

**EUROPEAN WINTER STORMS: DYNAMICAL  
ASPECTS AND WIND GUST ESTIMATION BASED ON  
RESULTS OF REGIONAL CLIMATE MODEL  
SIMULATIONS**

Inaugural-Dissertation

zur

Erlangung des Doktorgrades

der Mathematisch-Naturwissenschaftlichen Fakultät

der Universität zu Köln

vorgelegt von

**Patrick Ludwig**

aus Mönchengladbach

Köln, 2015



Berichtersteller:

Prof. Dr. Michael Kerschgens

Prof. Dr. Andreas Fink

Tag der mündlichen Prüfung:

02.06.2014



## **Abstract**

Extratropical cyclones in the North Atlantic – European sector are among the most perilous and damaging natural hazards affecting Europe. While most of the severe extratropical cyclones pass by Europe in northeastern direction, a small number of strong storms hit Europe each year. Their destructive power is mainly related to strong wind gusts, sustained high wind speeds or huge amounts of precipitation. Especially the relation between wind gusts and losses is a current topic of research. The focus of this thesis is to analyse severe extratropical cyclones affecting Europe during the winter half year (winter storms). The investigation of dynamical aspects and mesoscale processes associated with these hazardous extratropical cyclones is based on results from partly high-resolution mesoscale modelling approaches with the regional climate model COSMO-CLM. In the first part of this study, the ability of the COSMO-CLM to simulate severe winter storm events realistic is verified. With this aim, a total of 158 historical winter storms events between 1972 and 2008 are simulated. A new physically based wind gust estimation method, extended by a probabilistic approach, has been implemented to the COSMO-CLM to provide realistic area-wide wind gust distributions during the storm passage. In the second part, two recent severe winter storms (Kyrill in January 2007, Xynthia in February 2010) that caused widespread damage and even fatalities are investigated in more detail. Particularly, the dynamical aspects and mesoscale processes affecting their development are considered.

In general, the results approve the ability of realistic simulations of severe winter storm events by the COSMO-CLM. Further, the novel introduced wind gust estimation method provides comparable results to existing wind gust estimation methods. The probabilistic extension permits an estimation of the uncertainties of severe gusts at observational sites. This could be utilised as a valuable application when forecasting severe winter storm events to determine the possible range of maximum wind gusts and their related losses. This is of relevance for both society and for applications in insurance industry as well.

The results for winter storm Kyrill reveal the genesis of a secondary cyclone along the occluded front of the parent cyclone. This is an uncommon location for secondary frontal development and has not been documented in recent review articles covering this field of research. The formation of the secondary cyclone was associated with negative deformation

stretching and supported by diabatic processes in the lower and mid troposphere. The analysis of severe wind gusts associated with the strong cold front over Central Europe reveals the existence of a conditionally unstable boundary layer in addition with a turbulent flow. This indicates that high momentum at the top of the boundary layer could have been mixed downward to the ground leading to the strong surface wind gusts.

The analyses of winter storm Xynthia show that moist and warm air masses over the anomalously warm North Atlantic Ocean were incorporated into the cyclone. The realisation of sensitivity studies with modified (lowered) sea surface temperatures (SSTs) or reduced surface latent heat fluxes reveal their important influence on the intensity of the storm. A stronger reduction of SST or surfaces fluxes leads to a less intensive cyclone, which emphasizes the importance of warm and moist air near the ocean surface. This is also indicated by reduced diabatic heating rates at lower and mid levels and a weakening of the PV (potential vorticity) tower in case of altered surface conditions. These findings may be of relevance within the context of climate change and possible warming of SSTs.

To conclude, the ability of the COSMO-CLM to provide realistic simulations (including realistic area-wide wind gust estimates) of winter storms over the North Atlantic – European sector is ascertained. The realistic representation of near surface wind gusts by the model permits the possibility of estimation of losses and thus is of potential importance e.g. in the insurance business. Furthermore, the outcomes of this thesis extends the current knowledge and provides a substantial basis for the understanding of dynamical aspects and mesoscale mechanisms being relevant during the genesis, development and the passage of individual winter storms like Kyrill (January 2007) and Xynthia (February 2010) over Europe. Finally, the understanding of physical mechanisms and the effects of atmospheric conditions associated with individual winter storms are essential to improve the accuracy of the prediction of future storm events.

## **Kurzzusammenfassung**

Extratropische Zyklone über dem Nordatlantik zählen zu den gefährlichsten und schadensträchtigsten Naturgefahren in Europa. Obwohl der größte Teil der extremen extratropischen Zyklone in nordöstlicher Richtung an Europa vorbeizieht, sind jedes Jahr Teile Europas von einzelnen starken Stürmen betroffen. Ihre zerstörerische Kraft ist vorrangig andauerndem starken Wind bis hin zu schweren Orkanböen sowie enormen Niederschlagsmengen geschuldet. Insbesondere der Zusammenhang zwischen Sturmböen und resultierenden Schäden ist Gegenstand aktueller Forschung. Aus diesem Grund richtet sich der Fokus dieser Studie auf extreme extratropische Zyklone über Europa während des Winterhalbjahres (Winterstürme). Detaillierte Untersuchungen dieser Winterstürme hinsichtlich dynamischer Aspekte und mesoskaliger Prozesse während verschiedener Entwicklungsstadien werden mit Hilfe hochaufgelöster Simulationen eines regionalen Klimamodells (COSMO-CLM) durchgeführt. Im ersten Teil dieser Arbeit wird untersucht inwieweit das COSMO-CLM in der Lage ist extreme Winterstürme hinreichend genau wiederzugeben. Zu diesem Zweck wurden insgesamt 158 historische Winterstürme zwischen 1972 und 2008 simuliert. Um flächendeckende Informationen über die räumliche Verteilung der simulierten Böen zu erhalten wurde zusätzlich eine neuartige, um einen probabilistischen Ansatz erweiterte, Böenparametrisierung im COSMO-CLM implementiert. Der zweite Teil dieser Arbeit beschäftigt sich mit der ausführlichen Analyse zweier schadensintensiver Winterstürme der jüngeren Vergangenheit (Kyrill, Januar 2007; Xynthia Februar 2010). Der Fokus liegt hier auf der Betrachtung der dynamischen Aspekte und mesoskaligen Prozesse, die während der Sturmentwicklung eine bedeutende Rolle gespielt haben.

Es zeigt sich, dass das COSMO-CLM in der Lage ist die ausgewählten Winterstürme durchweg zufriedenstellend wiederzugeben. Des Weiteren liefert die neue Böenparametrisierung realistische und mit anderen Verfahren vergleichbare Resultate. Durch den probabilistischen Ansatz ist zusätzlich eine stationsbezogene Abschätzung der Unsicherheiten der simulierten Böen gegeben. In der Vorhersage ist somit die Möglichkeit gegeben, die Spannweite der zu erwartenden Böen, und somit auch der damit verbundenen Schäden durch Winterstürme, angeben zu können. Die möglichst genaue Vorhersage von Böen ist sowohl

von gesellschaftlichem Interesse als auch für Anwendungen in der Versicherungsbranche von eindeutiger Relevanz.

Die Untersuchungen zu Wintersturm Kyrill zeigen, dass eine sekundäre Zyklogenese entlang der Okklusionsfront des Sturmtiefs stattgefunden hat. Dies ist ein ungewöhnlicher und seltener Fall einer sekundären Entwicklung an Fronten und wird in vorhandenen Übersichtsartikeln zu diesem Thema nicht erwähnt. Die Entstehung der Sekundärzyklone steht in engem Zusammenhang mit negativer Streckungsdeformation entlang der Okklusionsfront sowie diabatischen Prozessen in der unteren und mittleren Troposphäre. Das Auftreten von starken Böen entlang der Kaltfront über Zentraleuropa steht im Zusammenhang mit einer bedingt labilen und turbulenten Grenzschicht. Diese Bedingungen ermöglichen das Heruntermischen hoher Windgeschwindigkeiten vom oberen Rand der Grenzschicht bis hinunter zum Boden.

Die Analyse von Wintersturm Xynthia zeigt, dass warme und feuchte Luftmassen über dem ungewöhnlich warmen südöstlichen Nordatlantik an dessen Entwicklung entscheidend beteiligt waren. Unter Berücksichtigung von Sensitivitätsstudien mit verringerter Meeresoberflächentemperatur bzw. reduziertem latenten Wärmefluss kann deren Einfluss auf die Existenz der feucht-warmen Luftmassen und somit auf die Sturmentwicklung quantifiziert werden. Je stärker die Abnahme der Meeresoberflächentemperatur bzw. des latenten Wärmeflusses angenommen wird, desto schwächer ist der resultierende Sturm. Zudem zeigt sich unter modifizierten Bedingungen eine deutliche Abnahme der diabatischen Erwärmungsrate in der unteren und mittleren Troposphäre, was mit einer Abnahme der Mächtigkeit der vertikalen Verteilung der potentiellen Vorticity einhergeht. Die Abhängigkeit der Sturmstärke vom Zustand der Meeresoberfläche ist im Rahmen eines zukünftigen Klimawandels durchaus von Bedeutung.

Zusammenfassend lässt sich sagen, dass das COSMO-CLM in der Lage ist Winterstürme (und die damit verbundenen Böenfelder) über dem Nordatlantik und Europa realistisch wiederzugeben. Die Simulation von bodennahen Böen eröffnet die Möglichkeit der Abschätzung von Schäden und bietet somit Anwendungsmöglichkeiten beispielsweise in der Versicherungswirtschaft. Zusätzlich erweitern die Erkenntnisse dieser Arbeit das Verständnis dynamischer Aspekte und mesoskaliger Prozesse, die entscheidend zur Entwicklung von Winterstürmen (Kyrill und Xynthia) beigetragen haben. Ein umfassendes Verständnis der physikalischen Mechanismen und atmosphärischen Randbedingungen, die mit der Entstehung einzelner Winterstürme in Verbindung stehen, ist für die Vorhersage zukünftiger Sturmereignisse von essentieller Bedeutung.

## Contents

Abstract .....	I
Kurzzusammenfassung .....	III
Contents .....	V
1. Introduction .....	1
2. Extratropical cyclones .....	3
2.1 Brief history of advances on Extratropical cyclones .....	3
2.2 Winter storms in the Atlantic - European sector .....	5
3. Winter storm modelling and wind gust estimation with COSMO-CLM .....	11
4. Case study of winter storm Kyrill (January 2007) .....	31
5. Case study of winter storm Xynthia (February 2010) .....	85
6. Summary of the results, discussion and outlook .....	101
6.1 Paper I .....	102
6.2 Paper II .....	103
6.3 Paper III .....	104
6.4 Discussion and outlook .....	105
References .....	109
Acknowledgments .....	115
Eigene Beteiligung an den Veröffentlichungen .....	117
Erklärung .....	119



### 1. Introduction

Extratropical cyclones (ETCs) are common everyday meteorological phenomena in the mid-latitudes. Their occurrence is accompanied by rapidly changes of local weather conditions, both in terms of temperature, precipitation and wind. Furthermore, the cyclones themselves are influenced by a variety of environmental conditions that affected their life cycle, path and intensity. The spatial extent and severity of single events puts them among the most costly and dangerous natural hazards in case they affect Europe (e.g. Held *et al.*, 2013). After Mailler *et al.* (2006) the most damaging European storms belong to one of the following three types: (1) serial storm, which are successive occurring events like Lothar<sup>1</sup> and Martin (1999) (Ulbrich *et al.*, 2001) or the storm series in the winter of 1989/1990 (Klawka and Ulbrich, 2003), (2) rapid developers, which exhibit deepening rates exceeding 24 hPa per day (also known as explosive cyclones or “bombs” e.g. Sanders and Gyakum, 1980) like Kyrill (2007) (Fink *et al.*, 2009) or Xynthia (2010) (Liberato *et al.*, 2013) and (3) slow movers, which are able to produce persistent large accumulations of precipitation concentrated over small regions (e.g. Elbe-Flood 2002; Ulbrich *et al.*, 2003, European summer flood 2013; Grams *et al.*, 2014). However, besides their perils, ETCs play a major role in compensation the latitudinal energy imbalance by transporting heat and moisture from the subtropics towards the cold Polar Regions (Oort, 1971).

The main intention of this study is to achieve a better understanding of mesoscale processes that play a role on the generation of strong wind gusts and thus on the formation and reorganising of winter storm events that affected Europe in the recent past. Besides from the analysis of a broad range of large-scale atmospheric fields, the realisation of realistic simulations with a non-hydrostatic regional climate model (COSMO-CLM, cf. Rockel *et al.*, 2008) is used to achieve this purpose. Additionally, the representation of a newly physical based wind gust estimation method, extended by a probabilistic approach within the COSMO-CLM is evaluated and compared to already existing wind gust estimation methods. Since wind gust measurements are limited to observation sites, the realistic simulation of area-wide wind gusts during winter storm events provides a strong benefit e.g. for applications in risk assessment. Furthermore, a detailed understanding of the physical mechanisms and the effects

---

<sup>1</sup> Storm names used in this thesis are given as by the Freie Universität Berlin and as used by German Weather Service. Source: <http://www.met.fu-berlin.de/adopt-a-vortex/historie>

of atmospheric conditions associated with individual winter storm events is essential to improve the accuracy of the prediction of future storm events. To accomplish this aim, the three included publications provide the basis for this thesis by addressing the following current issues:

- Evaluation of the COSMO-CLM performance and introduction of a novel physical based wind gust estimation method on basis of 158 historical European winter storm events (Paper I).
- Investigation of dynamic aspects of winter storm Kyrill (2007) producing severe wind gusts over Central Europe in association with secondary cyclogenesis over the eastern North Atlantic (Paper II).
- Considering the effects of anomalous high SSTs along the cyclone track on the development and intensity of winter storm Xynthia (2010) (Paper III).

Besides the selection criteria due to exceptional process-related characteristics of the individual winter storms Kyrill and Xynthia, the relevance in terms of corresponding losses is considered. Following loss estimates of leading reinsurers, Kyrill was ranked as the 2<sup>nd</sup> costliest (\$10 billion economic losses<sup>2</sup> in Europe) winter storm after Lothar (\$11.4 billion economic losses) since 1950. With a total economic loss of \$6.1 billion, winter storm Xynthia is ranked 4<sup>th</sup>. These high losses reveal the relevance of the selected winter storms also for society and economy.

This thesis is organised in the following way. Chapter 2 gives a short revision of the current state of scientific knowledge on extratropical cyclones. This includes a brief history of advances on the research of ETCs, an overview of ETCs in the Atlantic – European sector and a short introductory survey on wind gusts and their estimation techniques. Chapter 3 – 5 provide the relevant publications (Paper I - III) on which this thesis is based on. A summary and discussion of the main findings of the papers as well as an outlook of possible further work is given in chapter 6.

---

<sup>2</sup> Loss data taken from “Top 10 Losses – Europe; Costliest EU Windstorm/Winter Storm Events” available at: <http://catastropheinsight.aonbenfield.com/Pages/Home.aspx>

## 2. Extratropical cyclones

### 2.1 Brief history of advances on Extratropical cyclones

First efforts in describing the structure and life cycle of extratropical cyclones (ETCs) as a whole have been carried out by Bjerknes and Solberg (1922) and led to the polar front theory of cyclones, also known as Norwegian frontal cyclone model. This conceptual model of the life cycle of an ETC is still widely accepted, although it has been modified several times (e.g. Shapiro and Keyser, 1990, Browning *et al.*, 1994). As the polar front theory was established during the early years of the 20<sup>th</sup> century, upper air observations were not available (Reed, 1990). The whole cyclone life cycle was deduced from ground-based observations, starting with a wave disturbance along the polar front that separates tropical and polar air masses. Further amplification leads to the typical structure of a frontal cyclone, consisting of a warm sector bounded by a leading warm and a following cold front (Fig. 1a), which both exhibit typical cloud distributions (e.g. Browning and Roberts, 1994). The last stage of the cyclone is associated with the occlusion process (Schultz and Maas, 1993, Schultz and Vaughan, 2011) where the warm air is lifted up together with a shift of the cyclone towards the cold side of the polar front and finally leads to the decay of the cyclone.

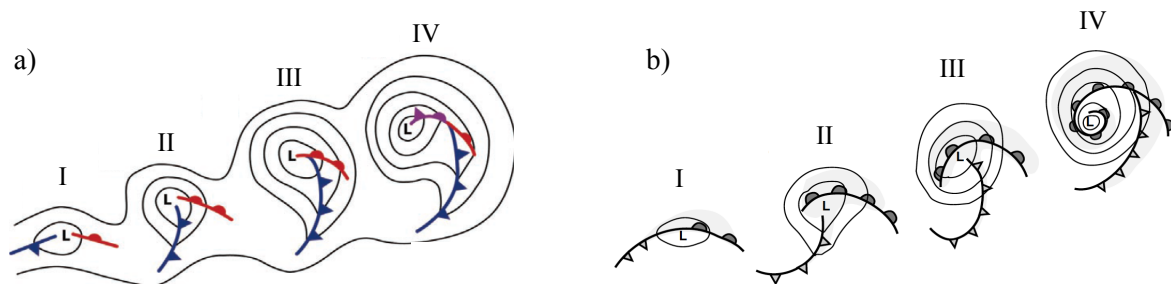


**Figure 1.** (a) Conceptual model of a Norwegian cyclone showing lower tropospheric (e.g. 850 hPa) geopotential height and fronts for different stages of the cyclone development (caption and figure adapted from Fig. 15a in Schultz and Vaughan, 2011) (b) Conceptual model of frontal-cyclone evolution proposed by Shapiro and Keyser (1990) (Caption and figure adapted from Fig. 2 in Semple, 2003).

During the time of the Second World War, regular upper air observations became more and more frequent, leading to new insights of atmospheric processes. Among them was the discovery of the existence of a westerly flow including embedded so-called Rossby-Waves (after Rossby, 1939), which are of planetary scale (usually 4-6 meanders can be observed

along the entire northern hemisphere). Investigations of the effects of velocity of the westerly background flow and propagation speed on the waves led to the relation of upper level divergence/convergence and surface pressure fall/rise by means of the pressure tendency equation (Bjerknes and Holmboe, 1944). Within their research the broadly familiar terms of 'Trough' and 'Ridge' were created, describing the direction (north- or southbound) of the wave's amplitude. The introduction of the theory of baroclinic instability (Charney, 1947, Eady, 1949) was an upcoming approach and milestone to describe the occurrence and growth of ETCs. In their independent research, they found out that waves in a baroclinic zone (lapse-rate on isobaric surfaces) are able to become unstable and thus may trigger ETC development. Together with the formulation of the general view on planetary flow patterns in the atmosphere (Rossby, 1940) and the detection of the jet stream (Palmen, 1948), the essentials for outstanding efforts in several branches of research on ETCs were provided. In recent years more and new knowledge has been obtained and many modifications and extensions of the Norwegian model lead to diverse conceptual models for different cyclone development mechanisms (e.g. review paper by Semple, 2003). A schematic overview of the fundamental Norwegian frontal cyclone model and the more recent conceptual model proposed by Shapiro & Keyser (1990) is given in Figure 1.

Another, more descriptive concept that describes the three dimensional airflow through an ETC is the principle of conveyor belts (e.g. Carlson, 1980; Browning, 1994; Semple, 2003). These system-relative airflows can be used to describe e.g. the developing cloud structure of an ETC. The two main airflows associated with frontal zones are the warm conveyor belt (WCB, Harrold, 1973) and the cold conveyor belt (CCB, Carlsson, 1980). The WCB forms ahead of the cold front and transports warm and humid air masses poleward from the lower troposphere at its southern end towards the upper troposphere at its northern end. Due to the ascending motion within the WCB, it is accountable for the elongated observed band of clouds along the cold front (Browning, 1986). The CCB originates at low levels ahead of the warm front and moves westward. It undercuts the poleward moving WCB with its associated precipitation and thus redistributes moisture within the system. Furthermore, there is a third type of airflow originating near the tropopause and descending behind the cold front towards the mid troposphere. The so-called dry intrusion (DI, Browning, 1997) is characterised by dry air masses and high values of potential vorticity. The DI can be identified as a cloud-free area (dry slot) in the water vapour, infrared and visible products of satellite imagery. Additionally, the DI is able to create potential instability as it overruns the cold front and thus the warm air associated with the WCB (Browning, 1997).

## 2.2 Winter storms in the Atlantic - European sector

Extratropical cyclones in the Atlantic - European sector, and particularly winter storms affecting Europe, are a main field of research for a considerable time. This sub-chapter gives a brief overview on the research that has been carried out with focus on the Atlantic - European sector. Most of the North Atlantic ETCs originate as small perturbations at the western parts of the North Atlantic basin, near the warm western oceanic surface currents. This region is also known as the North Atlantic storm track (Hoskins and Valdes, 1990). It is commonly characterised by a strong meridional temperature gradient along the hyperbaroclinic polar front that separates warm subtropical air masses in the south and polar air masses to the north (Pinto *et al.*, 2009). As a result of thermal wind balance, strong baroclinicity is associated with a strong upper-tropospheric jet stream located on the warm side of the polar front (Carlson, 1991). This baroclinicity is of essential importance for ETC development (e.g. Hoskins and Hodges, 2002; Gray and Dacre, 2006). Since the upper level jet stream is associated with divergence at the right entrance and left exit region of the jet maximum (Uccellini and Johnson, 1979), it plays a crucial role in enhancing the evolution of ETCs. Baehr *et al.* (1999) showed that ETCs crossing of the jet stream undergo a rapid deepening phase. Pinto *et al.* (2009) determined climatologies of the occurrence of extreme

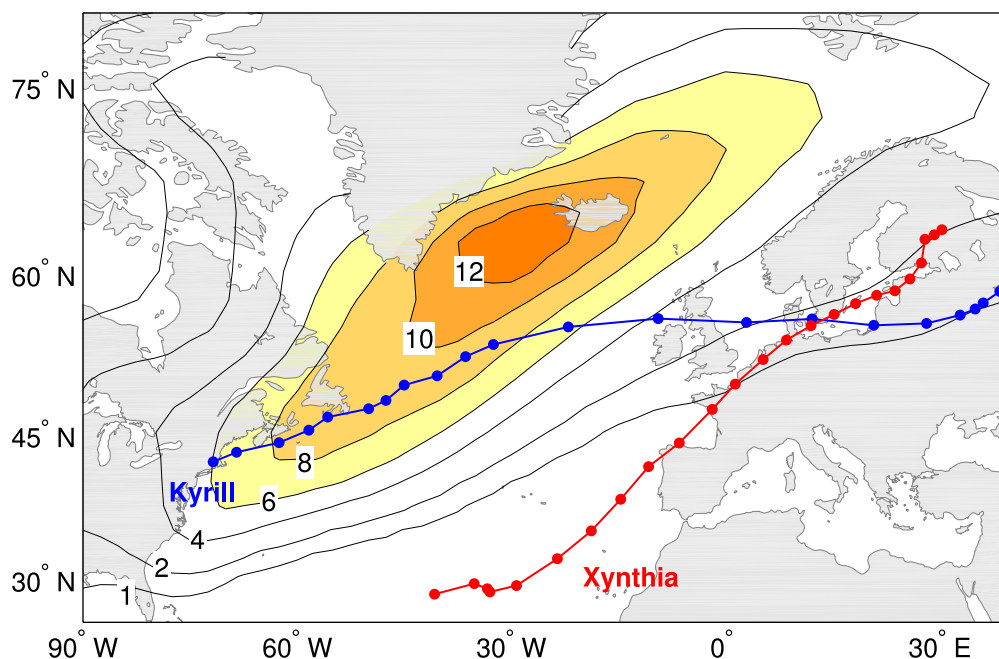


**Figure 2.** Cyclone track density (cyclone days/winter) of extreme cyclones over the North Atlantic and Europe for NCEP (1958-1998). The tracks (points at 6-hourly intervals, also from derived NCEP) of winter storms Kyrill (blue, starting at 1800 UTC 17 January 2007) and Xynthia (red, 1200 UTC 25 February 2010) are included. (Caption and figure adapted from Fig. 4 in Pinto *et al.*, 2009).

and non-extreme ETCs based on NCEP-reanalysis data (Kalnay *et al.*, 1996) for the period 1958-1998. Here, extreme cyclones are classified as the 10% strongest of all identified ETCs. A climatology of the cyclone track density for extreme cyclones during winter together with the tracks of the recent winter storms Kyrill and Xynthia (that are the focuses of Paper II and Paper III) is presented in Figure 2. In general, extreme cyclones (as well as non-extreme cyclones, not shown) tend to move towards the northeast, with only a few systems affecting Europe each winter.

The current state of the North Atlantic storm track and thus the tracks of the ETCs are closely related to the phase of the North Atlantic Oscillation (NAO, e.g. Wanner *et al.*, 2001). The NAO (based on the pressure difference between the semi-permanent Icelandic Low and the Azores High) is the leading pattern of variability in the North Atlantic and refers to the redistribution of atmospheric mass between the subtropical Atlantic and the Polar Regions (Hurrell and Deser, 2009). Changes from one NAO phase to another are associated with changes of the direction and strength of the surface westerlies across the North Atlantic towards Europe (Hurrell, 1995). Pinto *et al.* (2009) figured out that extreme cyclones occur more (less) often during positive (negative) phases of the NAO. Additionally, a shift of the NAO dipole towards Europe during positive phases results in an enhanced background pressure gradient that favours cyclone activity over Europe e.g. in the case of winter storm Kyrill (2007) (Fink *et al.*, 2009). Nevertheless, even during negative NAO phases extreme cyclones can occur and affect Europe as in the recent case of winter storm Xynthia (2010). A negative NAO phase is usually associated with a southward shift of the upper level jet stream (Woolings *et al.*, 2010), which plays a crucial role on the far southern formation of Xynthia.

Besides the well-known region of ETC occurrence outlined above, Ayrault *et al.* (1995) detected a distinct area downstream and slightly south of the climatological storm track location where frontal waves are able to develop during zonal weather regimes. These secondary cyclones often originate along the intensive trailing cold front of a parent cyclone and can have large growth rates (Parker, 1998). For example, winter storm Kyrill was identified as an unusual case of secondary cyclogenesis as the secondary cyclone developed at the occluded front of the parent cyclone (see Paper II of this thesis). As summarised by Parker (1998), various processes are important for the growth of frontal waves. These processes include shear at the frontal zone (e.g. Joly and Thorpe, 1991), large-scale strain (e.g. Renfrew *et al.*, 1997), latent heat release (e.g. Hoskins and Berrisford, 1988; Ahmadi-Givi *et al.*, 2003), boundary layer processes (Adamson *et al.*, 2006) and the influence of a local stripe of

maximum boundary layer potential vorticity (PV) that is associated with barotropic instability (cf. Figure 1 in Dacre and Gray, 2006).

Besides the effects of high low-level PV on secondary cyclogenesis, the PV-concept first used by Rossby (1940) and Ertel (1942) and enhanced by Hoskins *et al.* (1985) can be used to explain and analyse the evolution of ETCs. The two basic properties of PV are (1) conservation (PV is conserved in case of adiabatic motion) and (2) invertibility (under suitable balance conditions, such as geostrophic balance, the wind and temperature field can be derived from PV if it is given everywhere) (Hoskins, 1997). PV is defined as:

$$PV = \frac{1}{\rho} \zeta \cdot \nabla \theta$$

where  $\rho$  is the density,  $\zeta$  the absolute vorticity and  $\nabla \theta$  the gradient of the potential temperature. PV is often expressed in PVU units ( $1 \text{ PVU} = 10^{-6} \text{ m}^2 \text{ s}^{-1} \text{ K kg}^{-1}$ ). A potential application of this PV concept is for instance the definition of the dynamic tropopause (Hoskins, 1990). While the climatological distribution of PV has values between 0 and 1 PVU within the troposphere, there is a sharp increase of the static stability between the upper troposphere and lower stratosphere that leads to enhanced PV values, where the 2 PVU surface corresponds to the dynamic tropopause. The PV concept also allows for explaining cyclogenesis in case that a positive upper-level PV anomaly arrives over a low-level baroclinic region (Hoskins, 1985). Figure 3 illustrated the interaction of such an upper level PV anomaly and the induced circulation. The positive upper-level PV anomaly is associated with cyclonic circulation and induces a cyclonic circulation that extends through the troposphere down to the surface (Fig. 3 a). The low-level circulation in turn creates a low-level positive temperature anomaly by advection of warm air towards the north and somewhat ahead of the upper-level PV anomaly (Fig. 3 b). This warm low-level temperature anomaly

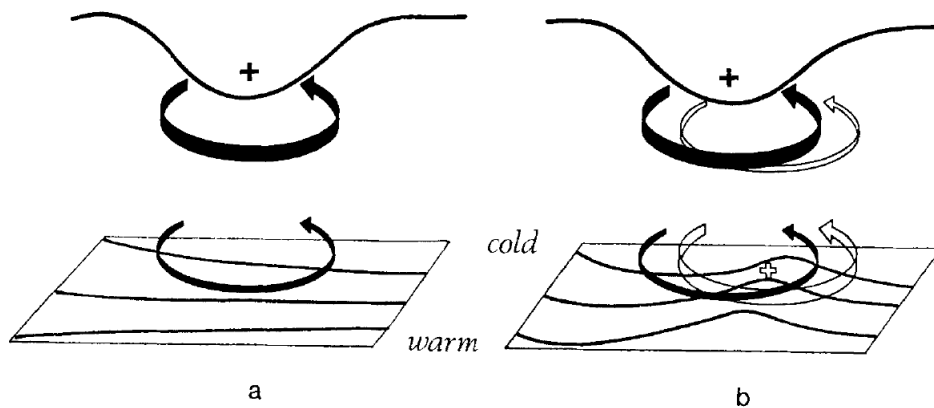


**Figure 3.** Schematic overview of cyclogenesis associated with the arrival of an upper-level PV anomaly over a low-level baroclinic region (Caption and figure adapted from Fig. 21 in Hoskins, 1985). See text for details.

again induces a cyclonic circulation and thus is able to reinforce the upper-level circulation pattern.

As mentioned before, PV is a conserved quantity in case of adiabatic motions. Since diabatic processes considerably determine the development of extratropical cyclones, the application of the PV perspective is a valuable tool to analyse processes that are important for the evolution of ETCs. Many studies have emphasised the importance of diabatic processes, in particular latent heat release due to condensation of water vapour, on the development of ETCs (e.g. Danard, 1964; Tracton, 1973; Uccellini, 1990). In a recent study by Fink *et al.* (2012) the role of diabatic processes on the development of five recent winter storms (Lothar and Martin (1999), Kyrill (2007), Klaus (2009, cf. Liberato *et al.*, 2011) and Xynthia (2010)) is quantified. The main finding of this study is that the pressure fall of three investigated storms (Lothar, Klaus and Xynthia) is mainly related to diabatic processes, while baroclinic processes are dominant for Martin and Kyrill. The key effect of latent heat release by condensation is the generation of anomalously high PV in the lower and mid troposphere (e.g. Reed *et al.*, 1992). If these high PV anomalies interact with a positive upper-level PV anomaly, they form a so-called PV tower (Rossa *et al.*, 2000) that extends vertically through the troposphere and often is associated with rapidly deepening cyclones like the “October Storm” (Hoskins and Berrisford, 1988), the “Presidents Day Cyclone” (Whitaker *et al.*, 1988), winter storm Lothar (Wernli *et al.*, 2002) or the more recent winter storm Xynthia (Campa and Wernli, 2012; also see Paper III of this thesis). Furthermore, diabatic processes, like they occur in WCBs, are able to modify the upper-tropospheric wave guide (Grams *et al.*, 2011). Along the airstream of a WCB, the PV increases due to condensational heating as long as the air parcels are below the level of maximum diabatic heating (see Figure 4 b in Wernli and Davies, 1997). During further ascent close to the tropopause region, a reduction of PV occurs, leading to negative upper-level PV anomalies. These negative PV anomalies in turn can have a significant impact on the downstream flow evolution like the formation of meridional elongated PV-streamers. Massacand *et al.* (2001) identified an upper level PV-streamer as a precursor for a high-impact weather of a Mediterranean cyclonic development. Likewise, the evolution of winter storm Xynthia is associated with an upper-level PV streamer (Piaget, 2011, also see Paper II of this thesis)

Another widespread field of research associated with ETCs covers the connection between intense winter storms and the extremes in surface winds. These extremes in surface winds are often associated with convective downdrafts along cold fronts (e.g. Houze and Hobbs, 1982) or convective systems like derechos (e.g. Gatzert *et al.*, 2011). Also for non-

convective high winds, like they occur in an environment of steep pressure gradients or within low-level jets (Browning and Pardoe, 1973), some detailed further physical explanations exist (Knox *et al.*, 2011). For example, tropopause folds (e.g. Uccellini, 1990) could be related to high surface winds (Browning and Reynolds, 1994). The authors figured out that during a severe wind event in the UK 1991, high-momentum stratospheric air descends to the boundary layer, and then was transferred to the surface via shear instabilities (Knox *et al.*, 2011). More recently, the sting jet hypothesis (first set up by Grønås, 1995) became more and more established since for different severe storm events high surface wind speeds could be linked to a sting jet (e.g. Great Storm over UK in October 1987 (Browning, 2004; Clark *et al.*, 2005), winter storm Jeanette in October 2002 (Parton *et al.* 2009) or winter storm Gudrun in January 2005 (Baker, 2009)). Sting jets evolve at the hooked tip of the cloud head that forms when the bent-back warm front and the CCB wrapped around the low centre (cf. Fig. 1 in Baker, 2009). So far, cyclones that have been associated with sting jets show a similar structure and development corresponding to the conceptual model by Shapiro and Keyser (1990) (Baker, 2009). In the presence of multiple mesoscale slantwise circulations (that may have been caused by conditional symmetric instability (CSI, Schultz and Schumacher, 1999)), air may leave the tip of the cloud head and enters the dry slot below where rapid evaporation and diabatic cooling causes further downward acceleration immediately upwind of the area of damaging surface winds (Browning, 2004).

Although the mechanisms leading to severe wind gusts are generally understood, their determination by means of atmospheric models is still a challenging issue. In particular, the proper estimation of losses requires a realistic representation of area-wide wind gusts. Klawns and Ulbrich (2003) derived a relationship between wind speed above a certain threshold and the estimation of losses that corresponds to the proportionality

$$\text{loss} \sim (\text{maximum wind speed})^3.$$

This implies that during high-wind situations, relatively small increases in wind speed can have a disproportionate impact on the amount of wind damage (Browning, 2004). Since the climatology of wind gusts does not coincide with the climatology of mean wind, a simple relation between mean wind and gust cannot be derived (Brasseur, 2001). For that purpose, a variety of wind gust estimation methods have been developed and applied to atmospheric models to obtain realistic area-wide distributions of wind gusts and/or associated losses during severe weather events for both present and future climate conditions (e.g. De Rooy and Kok, 2004; Della-Marta *et al.*, 2010; Pinto *et al.*, 2010; Schwierz, 2010; Etienne *et al.*, 2013).

In a first approach, Durst (1960) uses a gust factor derived as the fraction between wind gusts and mean wind speed to predict gusts. This technique has been refined later to take into account the state of the atmosphere in terms of stability or the roughness length in the environment (e.g. Wieringa, 1973; Verkaik, 2000). In an approach by Brasseur (2001), wind gusts are interpreted as downward transition of high-level boundary-layer momentum in case that turbulent kinetic energy (TKE) is able to overcome buoyancy force. Finally, the understanding of gusts as a combination of mean wind speed amplified by a part that can be connected with TKE (see Paper I of this thesis) should be mentioned as an alternative to predict wind gusts. In case that TKE is not directly available, Schulz and Heise (2003) make use of friction velocity as a predictor for turbulence.

### **3. Winter storm modelling and wind gust estimation with COSMO-CLM**

Journal article (published):

BORN, K., P. LUDWIG, AND J. G. PINTO, 2012: Wind Gust Estimation for Mid-European Winter Storms: Towards a Probabilistic View. *Tellus A* **64**:17471 doi: 10.3402/tellusa.v64i0.17471

Permission to reprint:

The article and any associated published material is distributed under the Creative Commons Attribution 3.0. Copyright on this article is retained by the authors.

Original page numbers of the manuscript are used.



# Wind gust estimation for Mid-European winter storms: towards a probabilistic view

By KAI BORN\*, PATRICK LUDWIG and JOAQUIM G. PINTO, *Institute for Geophysics and Meteorology, University of Cologne, Kerpener Str. 13, 50937, Cologne, Germany*

(Manuscript received 25 May 2011; in final form 9 January 2012)

## ABSTRACT

Three wind gust estimation (WGE) methods implemented in the numerical weather prediction (NWP) model COSMO-CLM are evaluated with respect to their forecast quality using skill scores. Two methods estimate gusts locally from mean wind speed and the turbulence state of the atmosphere, while the third one considers the mixing-down of high momentum within the planetary boundary layer (WGE Brasseur). One hundred and fifty-eight windstorms from the last four decades are simulated and results are compared with gust observations at 37 stations in Germany. Skill scores reveal that the local WGE methods show an overall better behaviour, whilst WGE Brasseur performs less well except for mountain regions. The here introduced WGE turbulent kinetic energy (TKE) permits a probabilistic interpretation using statistical characteristics of gusts at observational sites for an assessment of uncertainty. The WGE TKE formulation has the advantage of a 'native' interpretation of wind gusts as result of local appearance of TKE. The inclusion of a probabilistic WGE TKE approach in NWP models has, thus, several advantages over other methods, as it has the potential for an estimation of uncertainties of gusts at observational sites.

*Keywords:* windstorm, wind gust estimation, TKE, COSMO-CLM, probabilistic approach

## 1. Introduction

Wind gusts associated with windstorms are one of the main sources of economic and insured losses over Europe. For example, storm Kyrill (18 January 2007) caused insured losses of about €2.4 billion in Germany alone and caused a widespread disruption of normal social activities, public transportation and energy supply, as well as a large number of fatalities over large parts of Europe (cf. Fink et al., 2009). Therefore, the correct estimation and forecast of wind gusts associated with winter storms may enhance the capability of issuing accurate severe weather warnings and is of great value in scientific, societal and economical terms. Several studies on the estimation of gusts associated with the passage of windstorms were recently undertaken either using mesoscale modelling or statistical approaches (e.g. Brasseur, 2001; Goyette et al., 2003; De Rooy and Kok, 2004; Agustsson and Olafsson, 2004, 2009; Friederichs et al., 2009; Pinto et al., 2009). One of the recent applications is to estimate potential losses associated with wind gusts (e.g. Della-Marta et al., 2009, 2010; Pinto et al., 2010;

Schwierz et al., 2010). In these studies, very different approaches for wind gust estimation (WGE) are used. From this fact, the following questions arise: Which complexity of a WGE approach is necessary to obtain good WGEs? Which numerical weather prediction (NWP) model information may be provided that contributes to a WGE? Is a simple and self-suggesting approach based on the definition of subscale kinetic energy able to consider the obvious stochastic nature of gusts, and how does it compare to standard WGE methods?

Simulated near-surface winds from NWP models are usually smaller than observed wind gusts. This fact is related to (1) the formulation of model variables as averages over a space and time (grid box and time step) and (2) the high temporal variability of gustiness, especially during strong wind episodes. From the observational point of view, gust parameterisation reduces to the problem how a probability distribution of highly resolved wind speeds changes when the according time series is averaged. For NWP applications, model-resolved variables like wind speed and measures for the state of turbulence can be used to estimate gusts. In general, three techniques have been established: (1) the use of a gust factor as fraction between gust and mean wind speed (based on the original work of Durst, 1960;

\*Corresponding author.  
email: kai.born@uni-koeln.de

e.g. Wieringa, 1973; Verkaik, 2000), varying with atmospheric stability and/or roughness length in the environment; (2) the interpretation of gusts as downwards-transition of higher level boundary-layer momentum (e.g. Brasseur, 2001; Brasseur et al., 2002) and (3) the understanding of gusts as mean wind plus a part connected with turbulent kinetic energy (TKE). If TKE is not available, wind drag in terms of friction velocity (e.g. Schulz and Heise, 2003), atmospheric stability indices and wind direction, describing the advection of TKE from near-by regions with different roughness characteristics (Agustsson and Olafsson, 2004), can be used as a proxy for the turbulence state.

Wind gusts are affected by particular characteristics of the model topography, mainly land cover (in terms of roughness) and surface elevations, which induce turbulent eddies and, thus, influence the turbulence state of the atmosphere. The WGE formulation has to consider this subscale influence; its quality depends on the calibration of turbulence-related WGE parameters. One major setback is that spatially distributed observations usually do not provide sufficient information about the atmospheric turbulence; a statistical calibration of the turbulence-related part of a WGE is not possible. From the viewpoint of atmospheric modelling, wind gusts show a stochastic behaviour. Thus, rather than predicting absolute values, the estimation of a range of probability at which a gust value may occur appears to be an appropriate and skilful information. Further, such a probability range is also very helpful for various applications, for example, when deciding whether issuing severe weather warnings (e.g. Wichers Schreur and Geertsema, 2008).

In the following sections, a basic formulation of a turbulence-driven WGE method, hereafter called WGE TKE, considering a probabilistic extension, is described. Results of two standard WGE methods considering the turbulence state of the atmosphere locally and non-locally are compared with this new WGE method. The two standard WGE methods are the German Weather Service (DWD; Deutscher Wetterdienst) approach in COSMO-CLM, which uses friction velocity as predictor for turbulence (Schulz and Heise, 2003; Schulz, 2008), and the approach of Brasseur (2001), which estimates gusts considering a possible downward transition of air from higher atmospheric levels, carrying high momentum. The new WGE TKE approach defines the maximum available kinetic energy by interpreting TKE in a statistical sense as measure for wind speed variance. The probabilistic extension assesses the probability range of local gust factors statistically from observations. The forecast capability of the methods is tested by computation of proper skill scores. For the evaluation of WGE methods, a set of

historical European windstorms is considered. These were simulated by means of the regional climate model, COSMO-CLM, using reanalysis data as boundary conditions.

This study is organised as follows: Section 2 describes data and the NWP model, while Section 3 presents the different WGE formulations used. The evaluation of WGE methods (Section 4) is divided into four steps: (1) analysis of statistical characteristics of observational data, (2) an overall evaluation of COSMO-CLM simulations, (3) an exemplary comparison of WGE for typical winter storm events and (4) the calculation of skill scores for all events. The discussion of the results is presented in Section 5, and a short summary and conclusion finishes this study (Section 6).

## 2. NWP model and data

As a basis for this study, model simulations of 158 historical European windstorms between 1972 and 2008 (see Fig. 1a) have been undertaken using the mesoscale atmospheric model, COSMO (<http://www.cosmo-model.org>). It is mainly designed for application on the meso- $\beta/\gamma$  scale using grid resolutions from 20 km down to 1 km. The COSMO model has been widely used for regional climate simulations (e.g. Böhm et al., 2008; Jaeger et al., 2008; Rockel et al., 2008; Lautenschlager et al., 2009; see also COSMO-CLM community at <http://www.clm-community.eu>).

In the COSMO model, the non-hydrostatic, fully compressible Navier–Stokes equations are solved on an Arakawa-C grid using a hybrid terrain-following coordinate. In the vertical, the model contains the whole troposphere and parts of the lower stratosphere, the latter mainly as a damping layer. Standard vertical resolutions use 20–45 layers. Physical parameterisations consider an extended version of the level 2.5 scheme after Mellor and Yamada (1982) using prognostic TKE. Cloud microphysics are based on a Kessler-type scheme but contain cloud ice, graupel, and consider advection of cloud water/ice and rain/snow. Radiation effects are estimated using the  $\delta$ -two-stream approximation (Ritter and Geleyn, 1992). The model has been developed by the DWD and is in operational use for regional NWP in several European weather services. More detailed information may be found in Steppeler et al. (2003).

In this study, COSMO was used in its climate version COSMO-CLM4.0 (Böhm et al., 2008). The most important difference to the NWP version is that no assimilation of observational data and no nudging have been applied. In the vertical, 32 layers in the hybrid pressure-based terrain-following coordinate are used; the horizontal grid consists of  $257 \times 271$  grid boxes with grid sizes of  $0.165^\circ$  resolution

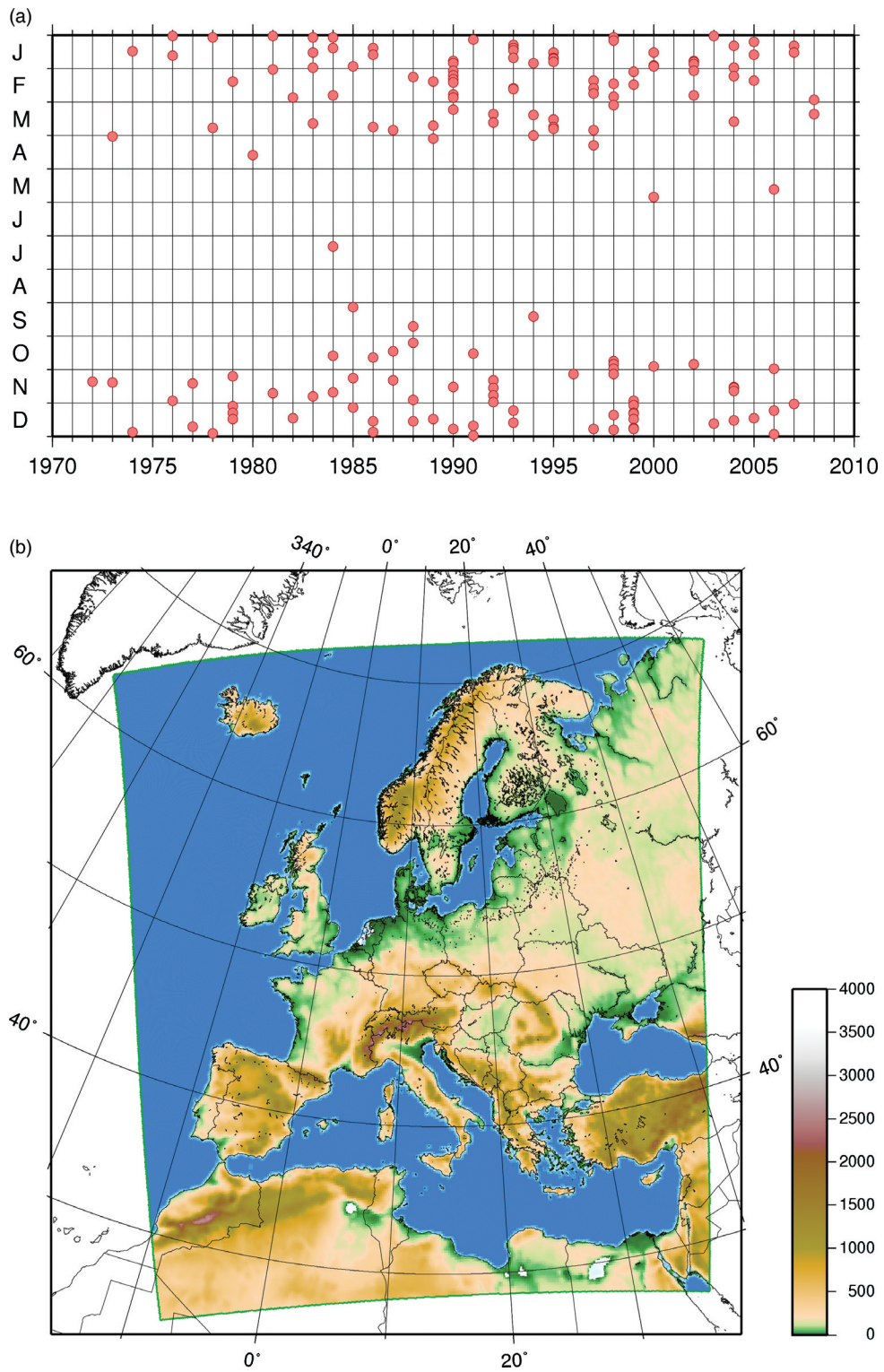


Fig. 1. (a) Year and month of simulated storms from 1972 to 2008, in a total of 158 storms and (b) COSMO-CLM model region, including orography, colour scale in m.

on a rotated latitude–longitude grid centred on  $8^\circ\text{W}$ ,  $50.75^\circ\text{N}$ . The thickness of the lowest model layer is approximately 67 m. The first full level, where horizontal momentum and temperature is calculated, is, thus, roughly at 33.5 m above ground. The Runge–Kutta integration scheme with a time step of 90 s and an output interval of 1 h was used. In general, the simulation periods are 96 h, starting 48 h before the peak of the event. For some cases (e.g. Lothar and Martin), the initialisation time had to be slightly changed to guarantee a good representation of that particular storm. The model domain comprises entire Europe and parts of Northern Africa (Fig. 1b). In this study, we focus on Germany for evaluation of the simulations.

In long-term transient COSMO-CLM simulations for Europe (e.g. Böhm et al., 2008; Jaeger et al., 2008), the representation of extreme events like windstorms may differ considerably from the real event. This fact is due to the boundary-only forcing, as atmospheric conditions are mainly inferred over the lateral boundaries. For a more accurate simulation of storms, a shorter model spin-up between initialisation and storm formation is advantageous, as it allows for an evolution of the event closer to the observed development. Therefore, the present set of COSMO-CLM simulations of historical storm events for Germany has been produced. As boundary forcing, ERA40 and ERA-Interim reanalyses (Uppala et al., 2005; Dee et al., 2011) are used. The storms in the overlapping period, 1989–2002, have been simulated using both ERA40 and ERA-Interim in order to assess the influence of the change of boundary forcing. It turned out that storm simulations using either ERA40 or ERA-Interim as atmospheric forcing do not exhibit systematic differences (not shown); hence, they can rather be understood as different realisation of the same storm.

The simulated episodes include all major storms, which affected central Europe between 1972 and 2008. These events were selected based on a storm intensity index, which considers exceedances of the 98th wind speed percentiles and is applied to the reanalysis dataset (Klawns and Ulbrich, 2003; Pinto et al., 2007a; Fink et al., 2009). In this way, the majority of the top-ranking events of the last decades for Germany are collected in the storm list. In addition, a few weaker events known from insurance companies’ reports were included. In order to allow for a comparison with observations, COSMO-CLM output had to be post-processed: In a horizontal plane, the  $0.165^\circ$  gridbox averages were interpolated to locations of the observational sites by means of a distance-weighted interpolation using a Gaussian filter (using  $9 \times 9$  neighbour grid points, and  $0.33^\circ$  lat/lon 1/e-width), including the vertical near-surface wind gradients calculated from model 10 m winds. The vertical gradients are needed for a height correction of winds and gusts: The effect of the vertical

displacement  $dz$  between surface heights at observational sites and the average model grid box height is considered by adding a correction factor  $(\partial v_{\max}/\partial z) \cdot dz$ . This kind of first-order correction is absolutely necessary for a comparison between grid box averages of model simulations and local observations.

Wind observations are provided for 37 DWD sites and cover the period from 1950 to 2005 (see Table 1). They consist of hourly wind records from 1979 to 2005, most observations start in 1976 with 3-hourly reports. The data is searched for inhomogeneities; obviously wrong observations are omitted (e.g.  $50 \text{ m s}^{-1}$  limited maximum winds). Except for mountain sites, the available number of gust observations typically decreases with distance to the coast: This is due to the fact that in Germany gusts are only reported when they exceed a threshold of  $12 \text{ m s}^{-1}$ . Such high gust values are less frequent inland.

For the evaluation of the RCM simulations, a dataset, including complete life cycles of cyclones obtained from ERA-Interim, is considered. Each track includes information (e.g. core pressure, vorticity) for one cyclone at each time step. The cyclone tracks are computed using an algorithm originally developed by Murray and Simmonds (1991), which is adapted and evaluated for Northern Hemisphere cyclone properties and high-resolution datasets (Pinto et al., 2005; Nissen et al., 2010). Further details on the method, its settings and cyclone climatologies can be found in Murray and Simmonds (1991), Simmonds et al. (1999) and Pinto et al. (2005, 2007b).

### 3. WGE estimation with different formulations

Wind gust estimation in NWP is a purely diagnostic calculation. The model variables are not influenced by the WGE. A WGE formulation considering model-predicted TKE and a probabilistic estimate of an uncertainty range is introduced here. The TKE approach is based on the relation between mean TKE  $\bar{q}$  and gusts  $v_{\max}$ , which can be summarised in the relationship:

$$v_{\max} = \sqrt{2E_{\max}} = \bar{v} + \sqrt{2\bar{q}} + \varepsilon_v \quad (1)$$

or, in a formulation of the gust factor  $g_v$ , which is simply the ratio gust/mean wind speed:

$$g_v = 1 + \frac{\sqrt{2\bar{q}}}{\bar{v}} + \varepsilon_g \quad (2)$$

Here,  $E_{\max}$  is the maximum kinetic energy, and  $\varepsilon_v$  is the ‘stochastic’ subgrid-scale part of  $v_{\max}$ . The random term  $\varepsilon_g = \varepsilon_v/\bar{v}$  is related to the difference between actual subscale kinetic energy of the gust and mean TKE and is of stochastic nature for the grid-scale model. It represents the variability of gusts due to the ‘unknown’ portion of small-scale

Table 1. Information on the 37 observational sites, including WMO number, station name, geographical location and height above seal level

WMO no.	Name	Lat (°N)	Lon (°E)	Elevation (m a.s.l.)	Daily hourly data available from		Until	Hourly values	Gusts (%)
10020	SYLT	55.01	8.25	26	1 January 1976	1 January 1979	31 December 2005	226933	20.51
10113	NORDERNEY	53.43	7.09	11	1 January 1976	1 January 1979	31 December 2005	202600	15.44
10129	BREMERHAVEN	53.32	8.35	7	1 January 1976	1 January 1979	31 December 2005	231334	8.77
10147	HAMBURG-FUHL.	53.38	9.59	11	1 January 1976	1 January 1981	31 December 2005	204360	6.33
10161	BOLTENHAGEN	54.00	11.12	15	1 January 1976	29 August 1977	31 December 2005	230103	11.10
10162	SCHWERIN	53.39	11.23	59	1 January 1976	29 August 1977	31 December 2005	226453	6.27
10170	ROSTOCK-WARNEM.	54.11	12.05	4	1 January 1976	29 August 1977	31 December 2005	229428	9.93
10224	BREMEN	53.03	8.48	5	1 January 1976	1 January 1981	31 December 2005	211507	6.55
10270	NEURUPPIN	52.54	12.49	38	1 July 1975	29 August 1977	31 December 2000	171210	3.73
10291	ANGERMUENDE	53.02	14.00	54	1 July 1975	29 August 1977	31 December 2000	170598	5.27
10317	OSNABRUECK	52.15	8.03	95	1 January 1976	1 January 1979	31 December 2005	177067	6.20
10338	HANNOVER-LANG.	52.28	9.41	59	1 January 1976	1 January 1976	31 December 2005	238068	4.97
10368	WIESENBURG	52.07	12.28	187	11 June 1990	11 June 1990	31 December 2000	88271	10.95
10382	BERLIN-TEGEL	52.34	13.19	36	2 January 1961	2 January 1961	31 December 2000	190182	2.66
10384	BERLIN-TEMP.	52.28	13.24	49	1 January 1950	1 January 1950	31 December 2000	368920	2.11
10385	BERLIN-SCHOEN.	52.23	13.32	45	1 July 1975	29 August 1977	31 December 2000	186349	3.61
10393	LINDENBERG	52.13	14.07	98	1 July 1975	29 August 1977	31 December 2000	182616	3.86
10396	MANSCHNOW	52.33	14.33	12	11 June 1990	11 June 1990	31 December 2000	85474	9.00
10438	KASSEL	51.18	9.27	231	1 January 1976	1 January 1979	31 December 2005	205664	3.03
10453	BROCKEN	51.48	10.37	1142	1 January 1976	29 August 1977	31 December 2005	235536	30.96
10469	LEIPZIG	51.26	12.14	131	1 January 1976	29 August 1977	31 December 2005	229602	5.02
10488	DRESDEN	51.08	13.45	227	1 January 1976	29 August 1977	31 December 2005	223602	5.27
10499	GOERLITZ	51.10	14.57	238	1 January 1976	29 August 1977	31 December 2005	218607	7.75
10513	KOELN-WAHN	50.52	7.10	92	1 January 1976	1 January 1981	31 December 2005	205973	3.16
10609	TRIER-PETRISBERG	49.45	6.40	265	1 January 1976	1 January 1979	31 December 2005	211573	5.71
10637	FRANKFURT/M.	50.03	8.36	112	1 January 1976	1 January 1981	31 December 2005	202463	4.47
10685	HOF-HOHENSAAS	50.19	11.53	567	1 January 1976	1 January 1979	31 December 2005	220504	7.23
10727	KARLSRUHE	49.02	8.22	112	1 January 1976	1 January 1979	31 December 2005	182201	5.87
10729	MANN HEIM	49.31	8.33	96	1 January 1976	1 January 1979	31 December 2005	197812	2.55
10738	STUTTGART-ECH.	48.41	9.14	371	1 January 1976	1 January 1981	31 December 2005	181479	3.23
10763	NUERNBERG-KRA.	49.30	11.03	314	1 January 1976	1 January 1981	31 December 2005	194281	2.74
10803	FREIBURGL.BR.	48.00	7.51	269	1 January 1976	1 January 1979	31 December 2005	211339	5.19
10838	ULM	48.23	9.57	571	1 January 1976	1 January 1979	31 December 2005	172506	2.60
10852	AUGSBURG-MUEHLH.	48.26	10.57	462	1 January 1976	1 January 1979	31 December 2005	198728	3.68
10908	FELDBERG/SCHW.	47.53	8.00	1486	1 January 1976	1 January 1979	31 December 2005	211775	24.58
10961	ZUGSPITZE	47.25	10.59	2960	1 January 1976	1 January 1979	31 December 2005	209701	26.26
10980	WENDELSTEIN	47.42	12.01	1832	1 January 1976	1 January 1979	31 December 2005	193686	23.55

In addition, the start/end dates, since/until daily and hourly observations are available. Last two columns mention the amount of available hourly values and the fraction of gusts therein, respectively.

kinetic energy.  $\varepsilon_g$  is not necessarily normally distributed but has obviously an expected value of 0. In this study, stochastic features of  $\varepsilon_g$  are derived from observational data by quantile regression. The model scale parameter used

is the ‘average turbulent wind speed’  $\bar{v}_{\text{turb}} = \bar{v} + \sqrt{2q}$ , which represents the median of the estimated gust distribution. The derivation of eqs. (1) and (2) and quantile regression details are shown in Appendixes A.1 and A.2.

In COSMO-CLM, the standard method for estimating non-convective gusts is to use wind speed interpolated from the lowest model level to 30 m height and the friction velocity  $u_*$ :

$$v_{\text{gust}} = |v_{z=30\text{m}}| + 3.0 \cdot 2.4 \cdot u_* \quad (3)$$

The maximum gust  $v_{\text{max}}$  is then defined as the maximum occurring in an output time interval, which here is 1 h. The factors 3.0 and 2.4 are motivated by Prandtl-layer theory (Panofsky and Dutton, 1984); the numerical values are determined empirically. A more detailed description and evaluation of this formulation can be found in Schulz and Heise (2003) and Schulz (2008). In general, the friction velocity method and TKE approach are relatively similar, because in both cases a predictor for local turbulence is estimated; in case of WGE DWD, an empirical factor allows for the optimum adaptation to observations. In case of WGE TKE, assumptions on the behaviour of the stochastic part  $\varepsilon_v$  have to be made. In this study, the characteristics of  $\varepsilon_v$  are based on gust observations.

Different from these approaches, as it does not consider the local turbulence directly, is the WGE approach named after Brasseur (2001), henceforth referred to as WGE Brasseur. It has been applied in many cases (e.g. Goyette et al., 2003; Pinto et al., 2009) and uses a relation between buoyancy and TKE in order to decide whether a parcel of air may be mixed down from a certain height to the surface, carrying momentum available for the peak gusts. The basic relation is  $v_{\text{max}} = \max(v(\hat{z}))$  for all levels  $\hat{z}$ , where

$$\frac{1}{\hat{z} - z_s} \int_{z_s}^{\hat{z}} \bar{q}(z') dz' \geq \int_{z_s}^{\hat{z}} g_N \frac{\theta_v(z') - \theta_v(z_l)}{\theta_v(z_l)} dz' \quad (4)$$

is satisfied. The inequation questions if the mean TKE, integrated from a near-surface layer  $z_s$  to a certain height  $\hat{z}$ , is able to overcome the buoyancy in the same air column. Buoyancy is calculated using the deviation of potential virtual temperature  $\theta_v$  in the considered height from the near-surface value and the gravity acceleration  $g_N$ . Here,  $z_l$  is the next lower model level. It has to be noted that in some studies,  $z_l$  is taken as near-surface level (e.g. Goyette et al., 2003; Pinto et al., 2009). An upper bounding value is formulated, allowing the wind velocity to be taken from the planetary boundary layer (PBL) only. The upper limit is represented by a dynamic PBL height assumption: PBL height is defined as the vertical level, where TKE is 1% of the surface TKE. Further, the method considers a lower bound, which takes into account only the TKE production due to vertical movements (see Brasseur, 2001, for more details). The mixing approach can be understood as a kind of non-local approach by interpreting the vertical turbulence structure.

The evaluation of the WGE methods is then undertaken using proper skill scores. Three scores compare different characteristics of the WGEs: The correlation (CORR) of time series evaluates accordance of temporal variability, the root mean square skill score (RSS) the deviation from WGEs to observations, and the quantile skill score (QSS) the similarity of probability distributions of WGEs in terms of the quantile functions. Formulae for the skill scores are listed in Appendix A.3.

## 4. Results

### 4.1. Statistical evaluation of observational data

In a first step, the relation between observed gusts and average wind speeds for the observational dataset is analysed. In particular, the possible use of multiple linear regression (MLR) models for spatial interpolation of statistical characteristics of gust factors is briefly discussed.

For this purpose, the Gauss-filtered density of observations in the  $(v_{10\text{m}} - v_{\text{max}})$ -space using 1/e-filter-widths of  $2 \text{ ms}^{-1}$  in each direction was calculated. Fig. 2 shows density plots of wind gusts against mean wind speeds and gust factors for three exemplary sites: one representative of an exposed mountain region, one for a coastal area and one for a low-range hilly region far from the coast. In addition, quantile regression lines based on a Weibull-like behaviour of the distribution of gust factors, dependent on wind speed above a certain level and assuming an exponential power-law relation between average wind speed and gusts (see Appendix A.2), have been added to the diagrams. The medians of the gust factors vary only little as a function of wind speed, showing very weak negative slopes in all cases. This behaviour may be attributed to the fact that strong wind conditions lead to near-neutral stratification with less variable TKE/wind speed relations. While the median of the gust factors is relatively similar for different locations, the spread of the gust factors' distribution at constant wind speed is obviously very variable: The width of the distributions of gust factors depends strongly on wind speed, and it increases with decreasing mean wind speed (see Fig. 2).

In Fig. 3, the spatial variation of the estimated mean gust factors is depicted for the observational sites. For this graphic, 10 sites with low counts of gust observations were excluded. The dependence of mean gust factors – given as quantiles – from latitude and height are shown as graphs, a map of Central Europe shows the location of the sites and corresponding average median values. The box and whiskers, showing 5, 25, 50, 75 and 95% quantiles (q05, q25, q50, q75 and q95), give an idea of the width of the gust factors distribution. The first conclusion apparent from the data is that there is no clear relation of the gust factor or its

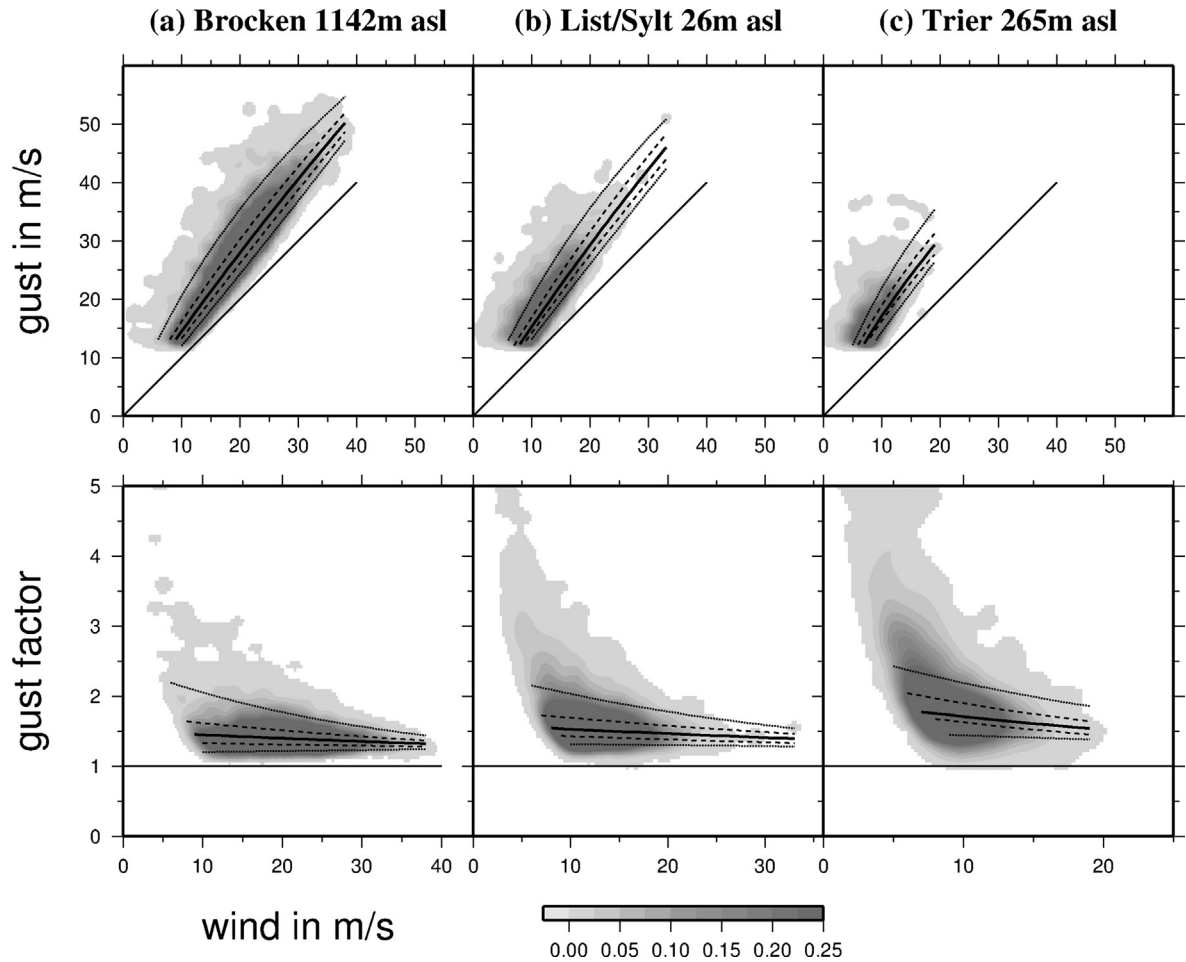


Fig. 2. Density plots of gust versus 10 m wind speed (upper row) and gust factors versus 10 m wind speed (lower row) for three exemplary climate observation sites, representative for an exposed mid-range mountain (Brocken, 10453), a maritime/coastal region (List/Sylt, 10020) and a low-range hilly region far from the coast (Trier, 10609). Colour shades represent normalised density of observations, lines represent a quantile regression of the gust factors for the 5, 25, 50, 75 and 95% quantiles. For more details on each station, see Table 1.

spread with latitude or elevation of observational sites. Extremely exposed mountain observations (10453 and 10908) are connected with rather small gust factors. This may be primarily attributed to the fact that in the free atmosphere, weaker turbulence is connected with higher average wind speeds. As it would be useful to relate the gust factors with external parameters of the land cover, linear models between the median gust factor and potential predictors were tested. Only those parameters that reveal at least a weak relationship are depicted in Fig. 3, namely, the location and the height of observational sites. A slight increase of gust factors with increasing distance to the coast from 1.45 to 1.65 may be observed in Fig. 3a. This increase is statistically significant at the 95% level (after student's  $t$ -test), but the explained variance is only 11%. A multilinear model using height of observational sites and their location

as predictors gains with a coefficient of determination of 13%, again not a promising result for a potential predictive skill of a statistical spatial interpolation. More interesting than a gust factor itself may be the spread, which is formed by the difference between  $q_{95}$  and  $q_{05}$ . This is a direct measure for the width of the gust factors distribution and for the uncertainty at which a gust factor can be estimated, which may be associated with local topographic characteristics. In order to test for the predictability of the ( $q_{95}$ – $q_{05}$ )–spread, a second multilinear model has been tested. It uses the difference of quantiles ( $q_{95}$ – $q_{05}$ ) as predictand and distance from the German Bight, height, roughness length ( $z_0$ ) and orographic variance within a circle of 10 km diameter as predictors (Fig. 4). The topographic characteristics were derived from USGS GTOPO30 and USGS Global Land Cover Characterisation 1 km land cover

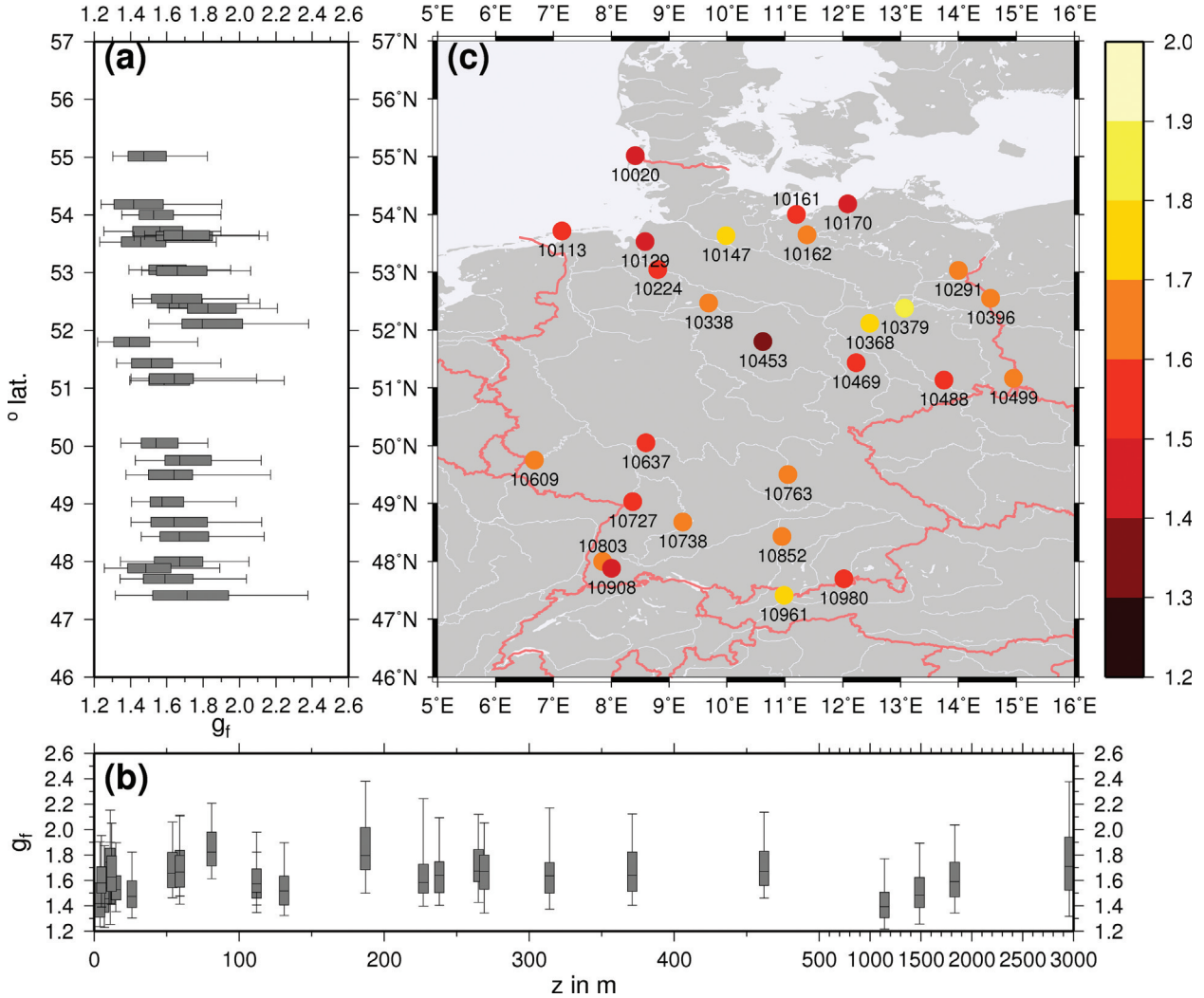


Fig. 3. (a) Mean gust factors at observational sites ( $x$ -axis) against latitude. (b) Mean gust factors against heights of observational sites. The box and whiskers show mean values for the 5, 25, 50, 75 and 95% quantile, respectively. (c) Mean 50% quantiles of the gust factors are depicted as colour dots on their geographical location. Ten stations with very low numbers of observations have been excluded from this plot. For more details on each station, see Table 1.

database. For this purely statistical model, a coefficient of determination (COFD, comparable to explained variance) of roughly 33% could be reached (Fig. 4a, topmost row). The predictability is higher than for the gust factor itself, but for a possible spatial interpolation the results are not convincing, indicating that such a statistical method needs improvement. Interestingly, roughness plays only a minor role for the predictive skill.

It has to be concluded that the gust factor seems to be strongly connected with dynamical features like wind speed or TKE, which have to be taken from model simulations. Still, an important result from Figs. 2 and 3 is that, in a first order approximation, the consideration of probabilities by using quantile regression parameters of the gust factors

with wind speed obtained for the specific sites, where a comparison of gusts is intended, provides more appropriate information than classical empirical gust estimation. This is further discussed in Section 4.4, Fig. 8.

#### 4.2. Overall evaluation of COSMO-CLM storm simulations

First, the performance of the COSMO-CLM storm simulations is discussed by comparing the paths of the storms in the RCM simulations with tracks derived directly from ERA-Interim data (see Section 2). Although ERA-Interim has a lower resolution, tracks of the storms obtained from these data are the best available estimate of storm positions

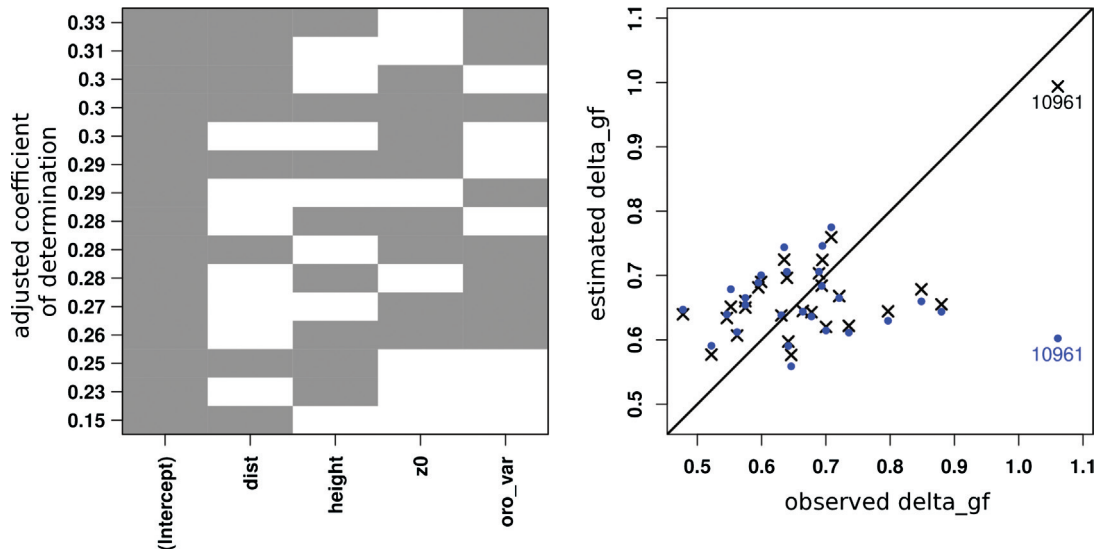


Fig. 4. Evaluation of the MLR model for the width of local gust factor distributions. Predictors are distance from the German Bight (dist), height of the site (height), roughness length at the site ( $z_0$ ) and orographic variance within a circle of 10 km diameter (oro\_var). (a) Adjusted coefficient of determination (COFD, left axis) for different combinations of predictors, ranked by their performance in terms of the COFD: the predictors used for each one model (rows) are marked with grey boxes. The best model with the highest COFD uses all predictors except roughness length (topmost row). (b) Scatter plot of the estimated and observed values by the optimum model. Crosses mark estimates of the full calibration; blue dots mark a cross-validation by leaving out data of the site. The station ‘Zugs Spitze’ is marked with the station number 10961.

and intensities. For the comparison with the COSMO-CLM results, core pressure is considered as a measure of intensity. The COSMO-CLM cyclone tracks are simply constructed from minimum pressure near the ERA-Interim cyclone track, which is sufficient, as the number of tracked cyclones within the RCM domain is limited, and the track can thus be identified unequivocally. Comparison is done only for the segment of the cyclone track within the COSMO-CLM domain.

The comparison of the tracks is shown in Table 2 and Fig. 5. In Table 2, characteristics of the 10 strongest cyclones for the ERA-Interim period from 1989 to 2007 – in terms of potential damage over Germany (cf. Pinto et al., 2007a; Fink et al., 2009) calculated from reanalysis data – are compared for reanalysis and COSMO-CLM simulations. Except for Daria (24 January 1990), the core pressure values are in good agreement. Fig. 5 exemplarily shows four cyclone tracks following very different paths with different

Table 2. Key features of the tracks of the strongest 10 storms (see text) simulated with CCLM

Storm	CCLM			ERA-Interim		
	Date	Lat (°N) Lon (°E)	$P_{\min}$ (hPa)	Date	Lat (°N) Lon (°E)	$P_{\min}$ (hPa)
Daria	25 January 1990 21UTC	56.43°N 4.63°E	958.02	25 January 1990 18UTC	56.82°N 0.42°E	949.13
Vivian	27 February 1990 12UTC	61.72°N 19.09°E	938.86	27 February 1990 12UTC	60.67°N 21.14°E	941.04
Wiebke	1 March 1990 03UTC	52.46°N 11.28°E	976.01	1 March 1990 06UTC	52.26°N 18.95°E	971.8
Verena	14 January 1993 10UTC	58.31°N 23.67°E	973.68	14 January 1993 06UTC	57.76°N 19.53°E	973.07
Barbara	24 January 1993 05UTC	59.97°N 3.00°E	965.43	24 January 1993 00UTC	59.17°N 3.74°W	966.8
Anatol	4 December 1999 00UTC	57.43°N 18.06°E	958.15	3 December 1999 18UTC	56.96°N 9.67°E	956.42
Lothar	27 December 1999 00UTC	51.39°N 22.82°E	974.75	26 December 1999 12UTC	50.46°N 9.37°E	976.09
Jeanett	27 October 2002 14UTC	56.32°N 7.06°E	977.86	27 October 2002 12UTC	56.44°N 4.05°E	975.32
Kyrill	19 January 2007 02UTC	56.47°N 24.01°E	962.97	19 January 2007 06UTC	56.00°N 28.54°E	961.51
Emma	29 February 2008 21UTC	62.72°N 1.14°W	956.45	29 February 2008 18UTC	62.34°N 4.66°W	959.97

Shown is the date and time, at which the minimum sea level pressure  $P_{\min}$  occurred, the geographical position and the minimum pressure value. The storms are in chronological order.

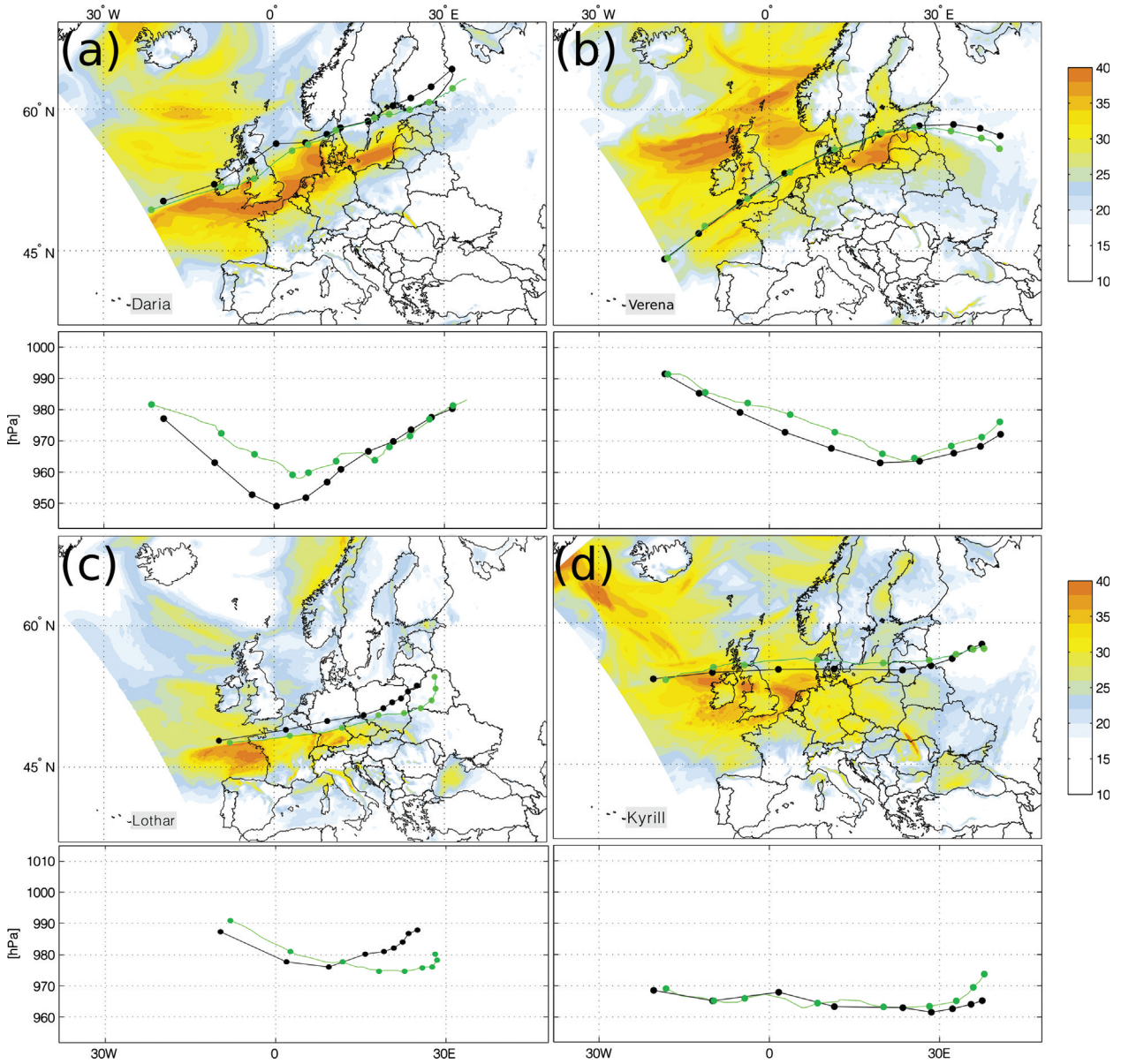


Fig. 5. Storm tracks, storm footprints (maximum wind gust speed during the event) and series of minimum pressure for four of the strongest storm events simulated with the COSMO-CLM (green tracks, colour-shaded gust speed in  $\text{m s}^{-1}$ ), in comparison to ERA-Interim Reanalysis (black tracks). The lower panels show time series of sea level pressure in hPa,  $x$ -axis is longitude. The dots mark six-hourly steps, which is the resolution of ERA-Interim, but COSMO-CLM tracks have been drawn hourly. All tracks were limited to the parts that lie entirely inside the COSMO-CLM domain. (a) Daria, 25 January 1990, (b) Verena, 14 January 1993, (c) Lothar, 26 December 1999 and (d) Kyrill, 18 January 2007.

intensities and characteristics (Daria, Barbara, Lothar, Kyrill). Results document that the tracks are generally in very good agreement. However, and particularly for cases when the track includes open systems during life-time, that means a vorticity minimum without closed isobars (like, for example, Lothar) on the reanalysis grid, the tracks may differ considerably, which does not come unexpectedly.

#### 4.3. Comparison of various WGE formulations for single storms

In this paragraph, results of WGE methods are compared. Fig. 6 shows footprints of storm ‘Anatol’ (3 December 1999; cf. Ulbrich et al., 2001). These footprints depict the maximum wind gust for each model grid point during the

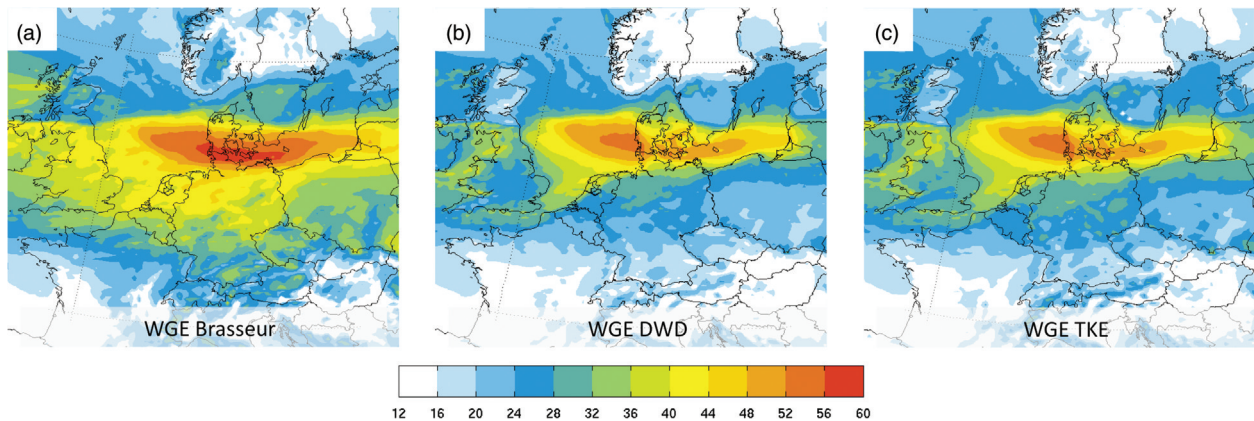


Fig. 6. Patterns of WGE for storm Anatol (a) WGE Brasseur, (b) WGE DWD and (c) WGE TKE. For further details, see text.

whole storm episode, thereby providing a wind gust ‘signature’ of the storm. Comparing the panels Fig. 6a–c, the WGE Brasseur (Fig. 6a) estimates highest wind speeds with little land–sea differences, while the two other methods provide very similar patterns (Fig. 6b, c). This is the case for the area primarily affected by the cyclone (North Sea, Denmark and Baltic Sea) and nearby areas (e.g. Germany). Over water, differences between WGE methods are smaller. Over land, WGE Brasseur shows less reduction in gust speed and, thus, estimates higher gusts compared with WGE DWD and WGE TKE. An over-estimation of gusts is also apparent in Brasseur (2001) and seems to be confined to storms, whereas less extreme situations are represented well.

In Fig. 7, WGE for three exemplary storms and all available gust observations are shown. Also, mean 10 m wind speeds simulated and from observations are depicted, in order to see if gust over- or under-estimation corresponds to a similar failure in the average wind speed. As expected from Fig. 6, the WGE Brasseur method overestimates gusts in high wind speed situations with gusts larger than  $30 \text{ m s}^{-1}$ , except at mountain sites, where it fits better to the observations. For gust speeds below  $30 \text{ m s}^{-1}$ , this systematic overestimation cannot be seen. On the other hand, for storm Lothar (26 December 1999), which had an impact far away from coastal regions in Germany (e.g. Ulbrich et al., 2001), results of WGE Brasseur were in better agreement with the other WGE methods than for storms moving over the North/Baltic Seas (e.g. Kyrill or Anatol). WGE DWD and the probabilistic estimate with the WGE TKE are relatively similar and generally, but not always, in better concordance with observations. Deficiencies are mostly related to failures in model prediction, as the comparison with mean 10 m wind speeds shows: Both WGE DWD and the probabilistic WGE TKE approach fail if the mean 10 m wind is not predicted correctly (e.g. station 10980 for storm Lothar). The width of the 90%

interval of the WGE, marked by the difference of the quantiles  $q_{05}$  and  $q_{95}$ , is typically  $10 \text{ m s}^{-1}$ , reaching also values of  $20 \text{ m s}^{-1}$  at mountain sites (10961 Zugspitze, 10980 Wendelstein), and sometimes at coastal stations (10129 Bremerhaven, 10147 Hamburg). The spread of the gusts uncertainty range depends on the average turbulent wind speed  $\bar{v}_{\text{turb}} = \bar{v} + \sqrt{2\bar{q}}$ , therefore, it is varying in both time and space. With respect to possible damage estimation from WGE, the large uncertainty indicates that the consideration of probabilistic aspects might be useful.

#### 4.4. Computation of skill scores for the whole storm sample

Next, an overall evaluation of WGE methods is performed taking as many historical storms into account as the observations allow (up to the end of 2005). For the calculation of the scores, only maximum wind gusts per event were considered, which reduces the effects of temporal phase shifts of a storm event. The three scores aim at three different aspects of quality: The QSS evaluates the form of the gust distribution without any emphasis on the temporal correlation of model data with observations; the RSS quantifies the effect of deviation between model and observations, the correlation CORR only evaluates temporal coincidence. Because QSS and RSS require a reference method for comparison, a WGE using a spatially varying, but temporary constant gust factor from Fig. 3 is defined as reference method. As Fig. 8 shows, the Brasseur-type WGE has a less good performance than the TKE-based WGEs, except at mountain sites. At some locations, WGE Brasseur is even worse than the constant gust factor. WGE DWD and the probabilistic TKE approach, where only the median value has been considered for scores, behave in a very similar way. Overall, the WGE DWD shows in this study slightly better skill scores than the other approaches (Table 3), although the difference to the probabilistic WGE TKE

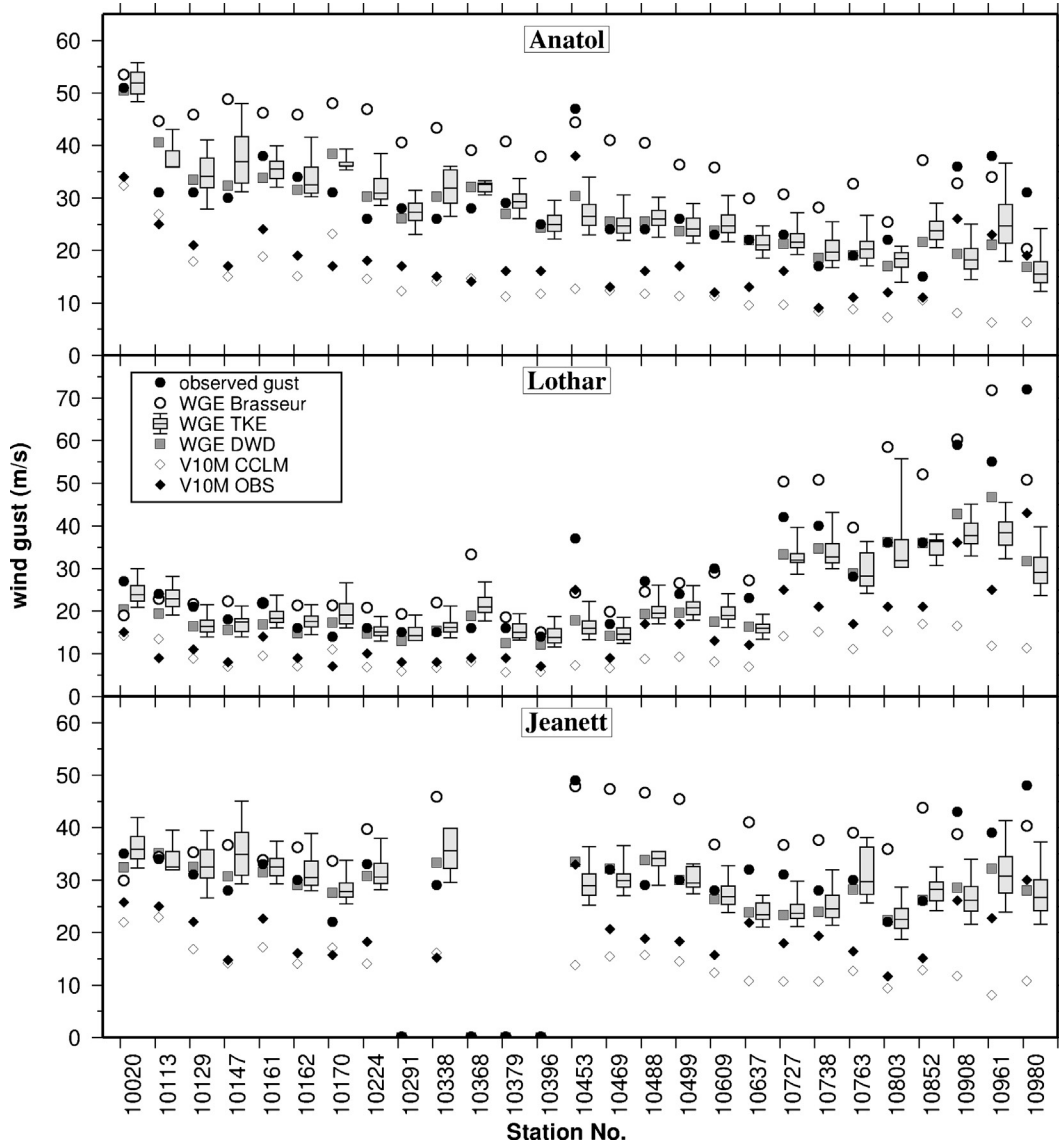


Fig. 7. Wind speed of gusts and 10 m winds at all available observational sites for three exemplary storms, Anatol (3 December 1999), Lothar (26 December 1999) and Jeanett (27 October 2002). The standard WGE methods after Brasseur (2001) (WGE Brasseur) and Schulz and Heise (2003) (WGE DWD) are compared with the TKE-based probabilistic estimation (box and whiskers for 5, 25, 50, 75 and 95% quantiles, respectively). The difference between 5 and 95% quantiles mark the range in which 90% of gusts are expected to occur. The latter are slightly shifted for easier comparison. For more details on each station, see Table 1.

is – due to the same physical base of both approaches – very small. The good performance of the WGE DWD could be expected, as this method was developed for Germany by the DWD. It has been slightly tuned by choosing 30 m instead of 10 m in the original formulation as reference height for available momentum and TKE in the Prandtl-layer of the model. Even though the WGE Brasseur method performs, in general, less well in this comparison, it has to be stated that the potential of fine-tuning has not been performed for this study. The consideration of a changed numerical implementation may counteract the overestimation of this

WGE (not shown) and provides more comparable results to the other methods.

## 5. Discussion

Our results indicate that the three different WGE approaches may provide quite diverse results. However, a main finding is that the WGE Brasseur approach produces results, which differ from the other two methods. Further, WGE DWD and WGE TKE deliver very similar gust patterns and time series. Such behaviour could be expected,

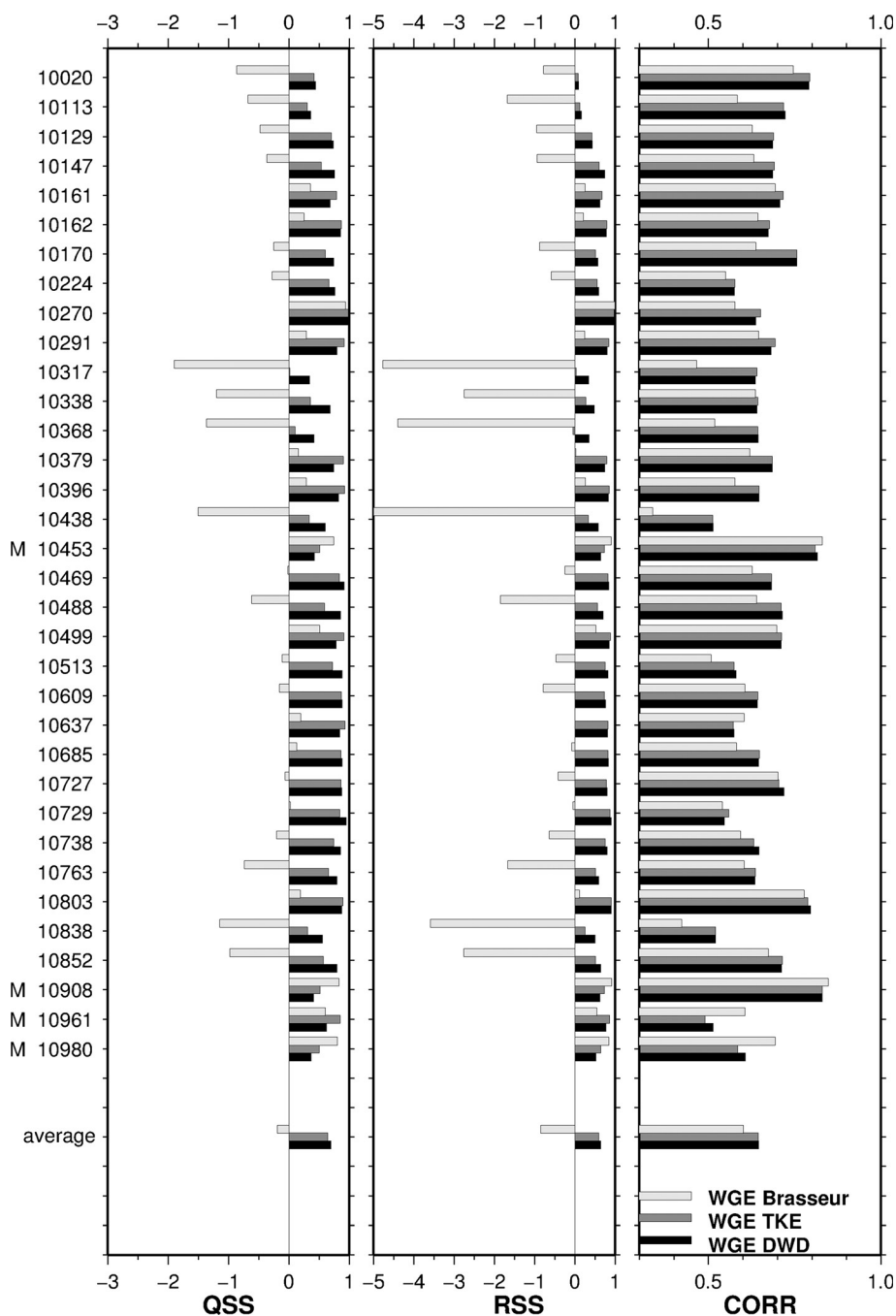


Fig. 8. Skill scores for the quality of the statistical distributions of gusts (QSS), the deviation of gust estimates from observations (RSS) and for temporal coincidence (CORR) at climate observation sites in Germany for WGE Brasseur (light grey), WGE TKE (dark grey) and WGE DWD (black). On the last row, an average over all stations per approach is given. For each station, the maximum number of considered storms is limited by availability of observations. M indicates a mountain station (height above 800 m a.s.l.). For more details on each station, see Table 1.

as the WGE Brasseur is in general methodically different from the others. WGE Brasseur overestimates wind gusts in flat terrain, whereas skill scores even suggest a better performance at mountain sites (cf. also Pinto et al., 2009).

However, although fine-tuning for WGE parameters and formulation of the discretisation has not been performed extensively in this study, results indicate that the quality of WGE may be improved by further calibration. From this

Table 3. Averaged skill scores for all stations and all events using investigated WGE methods

	DWD	TKE	Brasseur
QSS	0.69	0.63	-0.24
RSS	0.63	0.57	-0.96
CORR	0.65	0.65	0.60

See text for details on skill scores and different WGE formulations.

point of view, a general quality statement on the methods may be debatable; only the actual realisation (in our case an implementation in the COSMO-CLM model) can be rated.

Due to their intrinsic characteristics, WGE Brasseur and WGE DWD can be applied in every grid cell of an NWP model and are able to deliver high-resolution estimates of gust patterns. Nevertheless, the calibration evaluation is confined to observational sites; also for the WGE TKE, the probabilistic assessment of uncertainty ranges is based on local observations. The spatial interpolation of WGE TKE is in principle possible, but using less sophisticated approaches – simple MLRs using fixed topographic characters as predictors – it provides not satisfying results. Although statistical characteristics of the distribution are expected to depend very much on local topographic effects related to land cover (in terms of roughness length) or exposition, height and land-use in the nearest region of the observation sites (among other factors), dynamic factors like prevailing wind direction leading to advection of TKE and, of course, TKE itself seem to be more important for a predictive skill of a spatial interpolation model. All these factors are potential predictors in a multiple, not necessarily linear, regression model, which would have to be applied within the atmospheric model. An ‘offline’ version of a MLR model, which takes four topographic characteristics into account but which neglects dynamic forcing, is not a satisfying option to spatially interpolate uncertainties in terms of the width of local gust factor distributions (see Section 4.1). A satisfying interpolation technique (similar to Haas and Born, 2011), considering further dynamical parameters, requires far more attention than the present article can provide. Therefore, an interpolation of the statistical characteristics of gustiness between observational sites is not provided here and is left for future work.

As already stated, the WGE TKE method and the WGE DWD implementation behave very similar in terms of the skill scores. The time series of observed and simulated wind speeds indicate that gusts cannot be predicted correctly if the NWP model already underestimates mean wind speeds. Relatively small displacements of wind patterns, for example, connected with the cold front passage, result in large discrepancies between observations and simulated

gusts. Differences in temporal behaviour are reduced by considering footprints of storms, that is, the maximum gusts during the storm period, instead of hourly values for calculation of skill scores.

One of the main advantages of the WGE TKE is the consideration of a probabilistic formulation and, thus, of a measure of uncertainty for each value. For example, the 90% uncertainty intervals range from around  $10 \text{ m s}^{-1}$  in average to  $25 \text{ m s}^{-1}$  at mountain and some coastal stations, making clear that probabilistic interpretation of possible wind-related damages can be important. Thus, such an approach, including a probabilistic assessment of uncertainty ranges, may be of added value not only for issuing appropriate severe weather warnings, but also for application for wind-related damage estimation (e.g. Pinto et al., 2007a, 2010; Della-Marta et al., 2010; Schwierz et al., 2010) and wind energy estimates (e.g. Barthelmie et al., 2008; Pryor and Barthelmie, 2010).

## 6. Summary and conclusions

The present study compares three WGE methods with respect to their forecast quality using different skill scores representing the similarity of probability distributions, the standard error and the temporal correlation. Two of the WGE methods estimate gusts locally from mean wind speed and the turbulence state of the atmosphere (WGE DWD and WGE TKE), the third one named after Brasseur (2001) represents a mixing-down of high momentum within the PBL. The proposed WGE TKE permits a probabilistic interpretation using statistical characteristics of gusts at observational sites for an assessment of uncertainty. The WGE methods are implemented in the regional climate model, COSMO-CLM, which has been applied to 158 windstorms of the last four decades. The WGE methods are applied for each time step, calculating the maximum gust during every output interval. WGEs are compared with gust observations at 37 observational sites in Germany.

In terms of all skill scores, the two local WGE methods show an overall better behaviour. WGE Brasseur shows hardly a reduction of gust wind speeds over land compared with sea, leading to an overestimation between gusts over flatland and moderately hilly regions. The Brasseur method has only better skill scores for mountain stations and in situations with weaker winds. The potential of fine-tuning has not been applied in this study. In fact, extensive calibration and theoretical superiority may be competing effects: a theoretically more appropriate method may be worse in practice than any well fitted approach.

For historical reasons, a lot of WGE methods do not take TKE into account directly. The results of the present study document that using TKE as parameter for gust

estimation is especially valuable for NWP models, which supply TKE as prognostic or diagnostic variable. Without extensive tuning, WGE TKE is able to predict gusts at a comparable quality as the WGE DWD method. For cases when no TKE can be used directly or in a diagnostic way, estimates of atmospheric static stability may provide better results than constant gust factors. However, physically based methods should be preferred. The TKE formulation has the advantage that it allows for a ‘native’ interpretation of wind gusts as a result of local TKE. Thus, we propose that the consideration of a probabilistic WGE TKE approach in NWP models may have several advantages towards other methods, particularly as it allows for an estimation of uncertainties.

The WGE TKE method introduced in this work does not consider either fine-tuning or spatial interpolation. While the fine-tuning may not be of general interest, as its usefulness may be restricted to the fitted region and the particular NWP model characteristics, the spatial interpolation may be valuable for an improvement of gust estimations in regions with insufficient observations. Because of the unknown portion of the impact of local topographic characteristics, this interpolation has to be carried out very carefully and will be the objective of future work.

## 7. Acknowledgements

This research has been funded by the German Association of Insurers (‘Gesamtverband der Deutschen Versicherungswirtschaft’, GDV) in a project dealing with the impacts of climate change for the insurance industry for Germany (‘Auswirkungen des Klimawandels auf die Schadenssituation in der deutschen Versicherungswirtschaft’). Model simulations have been performed at the Computing Centre of the Cologne University (RRZK) and the German Climate Computing Centre (DKRZ). We thank the European Centre for Medium Range Weather Forecast (ECMWF, UK) for reanalysis data and the German Weather Service (DWD) for providing synoptic station data. We thank Rabea Haas for helping to prepare Fig. 4 and Sven Ulbrich (both Univ. Cologne) for Fig. 5 and Table 2.

## 8. Appendix A:

### A.1. Basic derivation of turbulence-driven wind gust estimation methods

We propose the use of the near-surface TKE for analysing the relation between average wind speed and wind maxima. This approach is similar to the theory proposed by Wichers Schreur and Geertsema (2008), but it handles the TKE in a different way. Following Reynolds’ concept of separation

in average and subscale portions of a variable, e. g.  $u_i = \bar{u}_i + u'_i$ , the mean kinetic energy  $\bar{E}$  consists of one term caused by average winds and another term caused by wind deviations. Using Einstein’s summation convention and the definition of average TKE:

$$q := \frac{1}{2} \bar{u}_i \bar{u}_i, \quad (\text{A.1})$$

$\bar{E}$  can be expressed in terms of the kinetic energy of the mean wind speed ( $\bar{u}_i = \frac{1}{2} \bar{u}_i \bar{u}_i$ ) and  $\bar{q}$ :

$$\bar{E} = E(\bar{u}_i) + \bar{q} \quad (\text{A.2})$$

Let  $(v_{\max})_i$  be the components of the wind gust vector and  $v_{\max} = \sqrt{(v_{\max})_i (v_{\max})_i}$  the wind gust speed, then the definitions  $(v_{\max})'_i := (v_{\max})_i - \bar{u}_i$  and  $q_{\max} := \frac{1}{2} (v_{\max})'_i (v_{\max})'_i$  lead to the following decomposition of the maximum kinetic energy available for gusts:

$$E_{\max} = \frac{1}{2} (v_{\max})_i (v_{\max})_i = \frac{1}{2} \left( \sqrt{2E(\bar{u}_i)} + \sqrt{2q_{\max}} \right)^2 \quad (\text{A.3})$$

The maximum gust speeds are expected to occur when mean wind and gust vectors have the same direction. Expressing  $v_{\max}$  in terms of  $E_{\max}$  yields:

$$v_{\max} = \sqrt{2E_{\max}} = \sqrt{2E(\bar{u}_i)} + \sqrt{2q_{\max}} \quad (\text{A.4})$$

In eq. (A.4),  $q_{\max}$  may be expressed in terms of the known grid-scale TKE and an unknown, subscale stochastic part. Thus, using  $\bar{v}$  as average wind speed, eq. (A.4) may be rewritten as:

$$v_{\max} = \bar{v} + \sqrt{2\bar{q}} + \varepsilon_v \quad (\text{A.5})$$

with  $\varepsilon_v$  being the square root of the difference between the energy of the wind speed deviation  $v'$  and the TKE:

$$\frac{1}{2} \varepsilon_v^2 = q_{\max} - \bar{q} \quad (\text{A.6})$$

Equation (A.5) is a key equation for turbulence-driven gust parameterisations, as they all can be expressed using this formula. It is an advantageous formulation for most state-of-the-art mesoscale models, as TKE is usually a prognostic variable of the turbulence parameterisation. Equation (A.4) is exact, if  $\varepsilon_v$  is known, which is variable in time and space. The gust factor ( $g_v$ ) can then be written as:

$$g_v = 1 + \frac{\sqrt{2\bar{q}}}{\bar{v}} + \varepsilon_g \quad (\text{A.7})$$

The random parts  $\varepsilon_v$  and  $\varepsilon_g = \varepsilon_v / \bar{v}$  are also variable both in space and time. In the WGE DWD, eq. (A.5) is approximated using:

$$\sqrt{2\bar{q}} + \varepsilon_v \approx au_*$$

with a semi-empirical factor  $\alpha$ , based partly on PBL theory considerations (Panofsky and Dutton, 1984) and partly being empirical (see Schulz, 2008; Schulz and Heise, 2003). In WGE TKE, the random part is estimated using the gust observations. Both WGE DWD and WGE TKE interpolate  $\bar{v}$ ,  $u^*$  and  $\bar{q}$  to a level of 30 m above surface.

### A.2. Probabilistic approach of WGE

The simplest way to achieve information about wind gust distributions is to estimate the width of the WGE distribution using mean wind speed  $\bar{q}$  dependent quantile functions, which may be assessed by quantile regression. For that purpose, we assume the gust distribution and, thus, the relation between gust factors and mean wind speed to be of exponential power-law type:

$$g_v = 1 + \exp(a \cdot \bar{v}^b) \quad (\text{A.8})$$

The assumed type of the fit function does not affect the results considerably, as long as curvature, slope and intercept are used in the fit. Here, very small or large values are discarded due to data availability, as (1) wind gusts are only reported above  $12 \text{ m s}^{-1}$ ; and (2) for some stations, the largest values are limited to  $50 \text{ m s}^{-1}$ . The fit of eq. (A.8) can be undertaken via linear regression using:

$$\ln(\ln(g_v - 1)) = \ln(a) + b \cdot \ln(\bar{v}) \quad (\text{A.9})$$

Equation (A.9) allows for an estimation of parameters  $b$  and  $a$  by linear quantile regression, which gives an assessment of the form of gust distributions at constant mean wind speed by showing 5, 25, 50, 75 and 95% quantiles (q05, q25, q50, q75 and q95).

### A.3. Skill scores

The evaluation of the WGE is undertaken using skill scores. The first and most simple score is the temporal correlation CORR of WGE and observations at weather stations for storm episodes. It reflects the temporal accordance of the two time series without regard to the absolute values. The other two scores are formulated in analogue to the Brier skill score and are designed to compare a method in focus with a reference method. The reference method is the WGE with a spatially varying but temporarily constant gust factor obtained from observations (see Fig. 3); the compared methods are either WGE Brasseur, the WGE DWD or WGE TKE. The basic form of all Brier-type skill scores is:

$$SS(\varepsilon) = 1 - \frac{\varepsilon}{\varepsilon_{\text{ref}}} \quad (\text{A.10})$$

with different types of error estimates ( $\varepsilon$ ,  $\varepsilon_{\text{ref}}$ ) for WGE methods and the reference method, respectively. A Brier-

type SS is zero for equal quality of both methods; for values below 0, the evaluated method is worse than the reference, and for values larger than 0, the tested method is better than reference with optimum performance at 1. For the RMSE skill score RSS, ( $\varepsilon$ ,  $\varepsilon_{\text{ref}}$ ) are root mean squared deviations of WGE and gust observations:

$$\varepsilon_{\text{RSS}} = \sqrt{\frac{1}{N} \sum_{i=1}^N (\text{WGE}_i - v_{\text{max},i})^2} \quad (\text{A.11})$$

WGE is the wind gust estimation after one of the three methods and  $v_{\text{max}}$  represents gust observations. The idea is simply that a better WGE should produce less deviation between observed and predicted wind gusts. For the quantile skill score (QSS), ( $\varepsilon$ ,  $\varepsilon_{\text{ref}}$ ) is the sum of distances of points of ranked time series ( $\text{WGE}_{\text{rank}}$ ,  $v_{\text{max,rank}}$ ) from the line of identity in a scatter plot:

$$\varepsilon_{\text{QSS}} = \frac{1}{N\sqrt{2}} \sum_{i=1}^N \text{abs}((\text{WGE}_i)_{\text{rank}} - (v_{\text{max},i})_{\text{rank}}) \quad (\text{A.12})$$

The scaling factor just indicates that in a scatter diagram of ranked values the length of the shortest path from the point ( $\text{WGE}_{\text{rank}}$ ,  $v_{\text{max,rank}}$ ) to the line of identity is measured. The QSS evaluates the form of distributions: although temporal correlation may be poor, the ranked events can be similar in a scatter plot.

## References

- Agustsson, H. and Olafsson, H. 2004. Mean gust factors over complex terrain. *Meteorol. Z.* **13**, 149–155.
- Agustsson, H. and Olafsson, H. 2009. Forecasting wind gusts in complex terrain. *Meteor. Atmos. Phys.* **103**, 173–185.
- Barthelmie, R. J., Murray, F. and Pryor, S. C. 2008. The economic benefit of short-term forecasting for wind energy in the UK electricity market. *Energy Policy* **36**, 1687–1696.
- Böhm, U., Keuler, K., Österle, H., Kücken, M. and Hauffe, D. 2008. Quality of a climate reconstruction for the CADSES region. *MetZ. Spec. Iss. Regional Clim. Model. COSMO-CLM (CCLM)* **17**(8), 477–485.
- Brasseur, O. 2001. Development and application of a physical approach to estimating wind gusts. *Mon. Wea. Rev.* **129**, 5–25.
- Brasseur, O., Gallee, H., Boyen, H. and Tricot, C. 2002. Reply. *Mon. Wea. Rev.* **130**, 1936–1943.
- Dee, D. P., Uppala, S. M., Simmons, A. J., Berrisford, P., Poli, P. and co-authors. 2011. The ERA-Interim reanalysis: configuration and performance of the data assimilation system. *Quart. J. R. Meteor. Soc.* **137**, 553–597. DOI: 10.1002/qj.828.
- Della-Marta, P. M., Liniger, M. A., Appenzeller C., Bresch D. N., Köllner-Heck P. and Muccione V. 2010. Improved estimates of the European winter wind storm climate and the risk of reinsurance loss using climate model data. *J. Appl. Meteor. Clim.* **49**, 2092–2120.

- Della-Marta, P. M., Mathis, H., Frei, C., Liniger, M. A., Kleinn, J. and Appenzeller, C. 2009. The return period of windstorms over Europe. *Int. J. Climatol.* **29**, 437–459.
- De Rooy, W. C. and Kok, K. 2004. A combined physical statistical approach for the downscaling of model wind speed. *Wea. Forec.* **19**, 485–495.
- Durst, C. D. 1960. Wind speeds over short periods of time. *Meteorol. Mag.* **89**, 181–186.
- Fink, A. H., Brücher, T., Ermert, E., Krüger, A. and Pinto, J. G. 2009. The European Storm Kyrill in January 2007: synoptic evolution and considerations with respect to climate change. *Nat. Hazards Earth Syst. Sci.* **9**, 405–423.
- Friederichs, P., Goeber, M., Bentzien, S., Lenz, A. and Krampitz, R. 2009. A probabilistic analysis of wind gusts using extreme value statistics. *Meteorol. Z.* **18**, 615–629.
- Goyette, S., Brasseur, O. and Beniston, M. 2003. Application of a new wind gust parameterisation: multiple scale studies performed with the Canadian regional climate model. *J. Geophys. Res.* **108**(D13), 4374. DOI: 10.1029/2002JD002646.
- Haas, R. and Born, K. 2011. Probabilistic downscaling of precipitation data in a subtropical mountain area: a two-step approach. *Nonlin. Process. Geophys.* **18**, 223–234.
- Jaeger, E. B., Anders, I., Lüthi, D., Rockel, B., Schär, C. and co-authors. 2008. Analysis of ERA40-driven CLM simulations for Europe. *Meteorol. Z.* **17**, 349–367.
- Klawa, M. and Ulbrich, U. 2003. A model for the estimation of storm losses and the identification of severe winter storms in Germany. *Nat. Hazards Earth Syst. Sci.* **3**, 725–732.
- Lautenschlager, M., Keuler, K., Wunram, C., Keup-Thiel, E., Schubert, M., Will, A., Rockel, B. and Boehm, U. (2009). Climate simulation with CLM, scenario A1B run no.1, data stream 3: European region MPI-M/MaD. *World Data Center Clim.* DOI: 10.1594/WDCC/CLM\_A1B\_1\_D3.
- Mellor, G. and Yamada, T. 1982. Development of a turbulence closure model for geophysical fluid problems. *Rev. Geophys. Space Phys.* **20**, 851–875.
- Murray, R. J. and Simmonds, I. 1991. A numerical scheme for tracking cyclone centres from digital data. Part I: development and operation of the scheme. *Aust. Meteorol. Mag.* **39**, 155–166.
- Nissen, K. M., Leckebusch, G. C., Pinto, J. G., Renggli, D., Ulbrich, S. and Ulbrich, U. 2010. Cyclones causing wind storms in the Mediterranean: characteristics, trends and links to large-scale patterns. *Nat. Hazards Earth Syst. Sci.* **10**, 1379–1391.
- Panofsky, H. A. and Dutton, J. A. 1984. *Atmospheric Turbulence: Models and Methods for Engineering Applications*. John Wiley & Sons, New York, 397 pp.
- Pinto, J. G., Fröhlich, E. L., Leckebusch, G. C. and Ulbrich, U. 2007a. Changes in storm loss potentials over Europe under modified climate conditions in an ensemble of simulations of ECHAM5/MPI-OM1. *Nat. Hazards Earth Syst. Sci.* **7**, 165–175.
- Pinto, J. G., Neuhaus, C. P., Krüger, A. and Kerschgens, M. 2009. Assessment of the wind gust estimates method in mesoscale modelling of storm events over West Germany. *Meteorol. Z.* **18**, 495–506.
- Pinto, J. G., Neuhaus, C. P., Leckebusch, G. C., Reyers, M. and Kerschgens, M. 2010. Estimation of wind storm impacts over West Germany under future climate conditions using a statistical-dynamical downscaling approach. *Tellus A* **62**, 188–201.
- Pinto, J. G., Spanghel, T., Ulbrich, U. and Speth, P. 2005. Sensitivities of a cyclone detection and tracking algorithm: individual tracks and climatology. *Meteorol. Z.* **14**, 823–838.
- Pinto, J. G., Ulbrich, U., Leckebusch, G. C., Spanghel, T., Reyers, M. and Zacharias, S. 2007b. Changes in storm track and cyclone activity in three SRES ensemble experiments with the ECHAM5/MPI-OM1 GCM. *Clim. Dyn.* **29**, 195–210.
- Pryor, S. C. and Barthelmie, R. J. 2010. Climate change impacts on wind energy: a review. *Renewable and Sustainable Energy Reviews* **14**, 430–437.
- Ritter, B. and Geleyn, J.-F. 1992. A comprehensive radiation scheme of numerical weather prediction with potential application to climate simulations. *Mon. Wea. Rev.* **120**, 303–325.
- Rockel, B., Will, A. and Hense, A. (eds.) (2008). Special issue: regional climate modelling with COSMO-CLM (CCLM). *Meteorol. Z.* **17**, 347–348.
- Schulz, J.-P. 2008. Revision of the turbulent gust diagnostics in the COSMO model. *COSMO Newslett.* **8**, 17–22. Online at: www.cosmo-model.org
- Schulz, J.-P. and Heise, E. 2003. A new scheme for diagnosing near-surface convective gusts. *COSMO Newslett.* **3**, 221–225. Online at: www.cosmo-model.org
- Schwierz, C., Köllner-Heck, P., Zenklusen Mutter, E., Bresch, D.N., Vidale, P.-L., Wild, M. and Schär, C. 2010. Modelling European winter wind storm losses in current and future climate. *Clim. Change* **101**, 485–514. DOI: 10.1007/s10584-009-9712-1.
- Simmonds, I., Murray, R. J. and Leighton, R. M. 1999. A refinement of cyclone tracking methods with data from FROST. *Aust. Met. Mag. Special Edition*, 35–49.
- Stappeler, J., Dom, G., Schättler, U., Bitzer, H. W., Gassmann, A. and co-authors. 2003. Meso-gamma scale forecasts using the nonhydrostatic model LM. *Meteorol. Atmos. Phys.* **82**, 75–96.
- Ulbrich, U., Fink, A. H., Klawa, M. and Pinto, J. G. 2001. Three extreme storms over Europe in December 1999. *Weather* **56**, 70–80.
- Uppala, S. M., Kallberg, P., Hernandez, A., Saarinen, S., Fiorino, M. and co-authors. 2005. The ERA-40 reanalysis. *Quart. J. R. Meteor. Soc.* **131**, 2961–3012.
- Verkaik, J. W. 2000. Evaluation of two gustiness models for exposure correction values. *J. Appl. Meteor.* **39**, 1613–1626.
- Wichers Schreur, B. and Geertsema, G. 2008. Theory for a TKE based parameterization of wind gusts. *HIRLAM Newslett.* **54**, 177–188. Online at: [http://hirlam.org/index.php?option=com\\_docman&Itemid=70](http://hirlam.org/index.php?option=com_docman&Itemid=70)
- Wieringa, J. 1973. Gust factors over open water and built up country. *Bound. Layer Meteorol.* **3**, 424–441.



#### **4. Case study of winter storm Kyrill (January 2007)**

Journal article (published online):

LUDWIG, P., J. G. PINTO, S. A. HOEPP, A. H. FINK, AND S. L. GRAY, 2014; Secondary cyclogenesis along an occluded front leading to damaging wind gusts: windstorm Kyrill, January 2007. *Mon. Wea. Rev.* doi: <http://dx.doi.org/10.1175/MWR-D-14-00304.1>

Permission to reprint:

©American Meteorological Society. Used with permission granted by Jinny Nathans, Permissions Officer at AMS.

Original page numbers of the manuscript are used.





# AMERICAN METEOROLOGICAL SOCIETY

*Monthly Weather Review*

## **EARLY ONLINE RELEASE**

This is a preliminary PDF of the author-produced manuscript that has been peer-reviewed and accepted for publication. Since it is being posted so soon after acceptance, it has not yet been copyedited, formatted, or processed by AMS Publications. This preliminary version of the manuscript may be downloaded, distributed, and cited, but please be aware that there will be visual differences and possibly some content differences between this version and the final published version.

The DOI for this manuscript is doi: 10.1175/MWR-D-14-00304.1

The final published version of this manuscript will replace the preliminary version at the above DOI once it is available.

If you would like to cite this EOR in a separate work, please use the following full citation:

Ludwig, P., J. Pinto, S. Hoeppe, A. Fink, and S. Gray, 2015: Secondary cyclogenesis along an occluded front leading to damaging wind gusts: windstorm Kyrill, January 2007. *Mon. Wea. Rev.* doi:10.1175/MWR-D-14-00304.1, in press.





19 **Abstract**

20 Windstorm Kyrill affected large parts of Europe in January 2007 and caused widespread  
21 havoc and loss of life. In this study the formation of a secondary cyclone, Kyrill II, along the  
22 occluded front of the mature cyclone Kyrill and the occurrence of severe wind gusts as Kyrill  
23 II passed over Germany are investigated with the help of high-resolution regional climate  
24 model simulations. Kyrill underwent an explosive cyclogenesis south of Greenland as the  
25 storm crossed polewards of an intense upper-level jet stream. Later in its life cycle secondary  
26 cyclogenesis occurred just west of the British Isles. The formation of Kyrill II along the  
27 occluded front was associated (a) with frontolytic strain and (b) with strong diabatic heating  
28 in combination with a developing upper-level shortwave trough. Sensitivity studies with  
29 reduced latent heat release feature a similar development but a weaker secondary cyclone,  
30 revealing the importance of diabatic processes during the formation of Kyrill II. Kyrill II  
31 moved further towards Europe and its development was favored by a split jet structure aloft,  
32 which maintained the cyclone's exceptionally deep core pressure (below 965 hPa) for at least  
33 36 hours. The occurrence of hurricane force winds related to the strong cold front over North  
34 and Central Germany is analyzed using convection-permitting simulations. The lower  
35 troposphere exhibits conditional instability, a turbulent flow and evaporative cooling.  
36 Simulation at high spatio-temporal resolution suggests that the downward mixing of high  
37 momentum (the wind speed at 875 hPa widely exceeded  $45 \text{ m s}^{-1}$ ) accounts for widespread  
38 severe surface wind gusts, which is in agreement with observed widespread losses.

## 1. Introduction

39           In January 2007, windstorm Kyrill<sup>1</sup> (cf. Fink *et al.*, 2009) swept across large parts of  
40 Western, Central and Eastern Europe resulting in 54 fatalities and overall insured losses of 4.6  
41 billion Euro in Germany, the UK, Belgium and the Netherlands (economic losses even  
42 reached 7.6 billion Euro, Swiss Re, 2008). As described in Fink *et al.* (2009) Kyrill underwent  
43 explosive cyclogenesis (a pressure drop of more than 24 hPa in 24 hours at 60°N, cf. Sanders  
44 and Gyakum, 1980) over the Northeastern Atlantic between 1200 UTC 16 January (998 hPa)  
45 and 1200 UTC 17 January (968 hPa). Most of the extratropical systems affecting Europe  
46 originate and intensify in this region, known as the North Atlantic storm track (e.g. Hoskins  
47 and Valdes, 1990). Like Kyrill, most of those systems emerged in a baroclinic environment  
48 (Hoskins and Hodges, 2002; Wernli *et al.*, 2002; Gray and Dacre, 2006), which is associated  
49 with a strong upper-tropospheric jet stream (Carlson, 1991). During the period of explosive  
50 cyclogenesis, Kyrill crossed the jet stream from the warm to the cold side (Fink *et al.*, 2009;  
51 their Figure 1). The crossing of the jet stream is known to correspond with the rapid  
52 deepening phase of extratropical cyclones (e.g. Palmén and Newton, 1969). Thus, upper-level  
53 divergence at the right entrance and left exit region of the jet streak (region of wind maximum  
54 within the jet stream) played a crucial role in enhancing the cyclone evolution (Uccellini and  
55 Johnson, 1979).

56           Fink *et al.* (2009) speculated that Kyrill would have then slowed down and decayed  
57 over the North Atlantic under normal circumstances. However, at 0000 UTC 18 January a  
58 secondary cyclogenesis initiated along the occluded front of Kyrill (henceforth Kyrill I),  
59 forming a secondary cyclone (henceforth Kyrill II), which then moved further towards Europe  
60 (Fig. 1). In general, secondary cyclones are formed from frontal waves along synoptic fronts  
61 e.g. the trailing cold front of a parent low (Parker, 1998a). Relative to the climatological

---

<sup>1</sup> Storm names employed herein are as given by the Freie Universität Berlin and as used by the German Weather Service. Source: <http://www.met.fu-berlin.de/adopt-a-vortex/archiv/>

62 storm track location, the preferred area for these events is shifted downstream and slightly  
63 south (Ayrault *et al.*, 1995). Such systems often reach Europe, typically during zonal weather  
64 regimes.

65 Zonal weather regimes over the North Atlantic are characterized by westerly flows and  
66 are associated with slightly to moderately positive values of the North Atlantic Oscillation  
67 (NAO, e.g. Wanner *et al.*, 2001) index. In January 2007, the NAO index<sup>2</sup> was strongly  
68 positive (+1.77) resulting in a series of extratropical cyclones (Anton, 3 January; Franz, 11  
69 January; Gerhard, 13 January; Hanno, 14 January; Lancelot, 20 January) over the North  
70 Atlantic with Kyrill being the most intense in terms of maximum wind gusts and precipitation  
71 amounts over Central Europe. This successive occurrence of cyclones (building a cyclone  
72 family) is also known as serial clustering (Mailier *et al.*, 2006; Pinto *et al.*, 2013).  
73 Additionally, the NAO dipole was shifted towards Europe forming an enhanced background  
74 pressure gradient (associated with amplified wind speeds at the surface) between Western  
75 Europe and the Baltic states, in which the cyclones were embedded (Fink *et al.*, 2009, their  
76 Figure 2).

77 The dynamics of such secondary cyclones have been investigated in several studies  
78 using either reanalysis data (e.g. Rivals *et al.*, 1998; Chaboureau and Thorpe, 1998) or  
79 numerical models (Carrera *et al.*, 1998). A comprehensive review of the dynamics of frontal  
80 waves and secondary cyclones is given by Parker (1998a). Therein, the shear at the frontal  
81 zone, the weakening of large-scale strain (or stretching deformation) field in the environment  
82 of the front, diabatic heating effects due to latent heat release inside clouds, boundary layer  
83 processes and the influence of a local strip of maximum potential vorticity (PV) are  
84 mentioned as decisive mechanisms for secondary cyclogenesis. Several studies investigated  
85 the influence of environmental deformation field on frontal wave development. An idealized

---

<sup>2</sup> A continuous update of the NAO index on monthly and seasonal scales is available at  
<http://www.cru.uea.ac.uk/~timo/datapages/naoi.htm>

86 study by Dritschel *et al.* (1991) provided evidence that deformation primarily affects the  
87 growth of an edge-wave. Several following studies (e.g. Bishop and Thorpe, 1994a, b;  
88 Renfrew *et al.*, 1997; Parker, 1998b; Dacre and Gray, 2006) further documented the  
89 importance of deformation strain on frontal wave development. While frontal wave  
90 development is suppressed in case of sufficient positive (frontogenetic) stretching  
91 deformation, reduced or negative (frontolytic) strain favors the occurrence of barotropic  
92 instabilities and thus of frontal wave development.

93 Intensive convection with severe wind gusts and exceptional precipitation amounts  
94 (some of them exceeding the mean January accumulations) were observed as the cold front  
95 passed over Central Europe. Over Eastern Germany, the Czech Republic and Poland a total of  
96 eight (including three F3) tornado reports were verified (cf. ESWD database, see Dotzek *et al.*  
97 *et al.*, 2009). Following the criteria of Johns and Hirt (1987), Kyrill II has even been classified  
98 as a cold-season derecho in Europe (cf. Gatzen *et al.*, 2011). The strong intensity of Kyrill II,  
99 particularly over Eastern Germany, is also indicated by a dry intrusion penetrating close to the  
100 surface in the vicinity of the cold front of Kyrill II (Fink *et al.*, 2009). The potential impacts  
101 of dry intrusions on extratropical cyclones and cold frontal rain bands have been described  
102 e.g. by Browning and Reynolds (1994), Browning and Golding (1995) and Browning (1997).  
103 The main effect is the generation of potential instability when cool and dry descending air  
104 overruns the warm conveyor belt in front of the cold front. A dry intrusion can be identified  
105 by i) a ‘dry-slot’ or ‘dark zone’ in the water vapor channel (e.g. Young *et al.*, 1987), and ii)  
106 downward advection of dry air with enhanced PV from the tropopause region (Browning,  
107 1997).

108 Methods for the estimation of wind gusts associated with the passage of windstorms,  
109 important e.g. for impact studies or loss estimations, using mesoscale modeling or statistical  
110 approaches, are documented in e.g. Brasseur, 2001; Goyette *et al.*, 2003; De Rooy and Kok,  
111 2004; Friederichs *et al.*, 2009; Born *et al.*, 2012. Methods for the estimation of wind gusts

112 from mesoscale model outputs can be partitioned into (i) the relation of wind gusts to mean  
113 wind speed based on a gust factor (Durst, 1960; Wieringa, 1973), (ii) the downward transition  
114 of higher-level boundary-layer momentum (Brasseur, 2001) and (iii) the interpretation of  
115 gusts as the sum of the mean wind speed and a wind component related to the turbulent  
116 kinetic energy (TKE, Born *et al.*, 2012). Schulz and Heise (2003) utilized the wind drag in  
117 terms of friction velocity when TKE was not available.

118 The objectives of this study are to

- 119 • Document the kinematic environment and dynamical forcing leading to the  
120 uncommon formation of the secondary cyclone Kyrill II along the occluded front of  
121 parent low Kyrill I.
- 122 • Quantify the influence of diabatic processes on the intensity of Kyrill II using  
123 sensitivity experiments in which latent heat release from the convection  
124 parameterization scheme is withheld.
- 125 • Characterize the boundary layer conditions to determine the cause of the strong wind  
126 gusts along the cold front over Germany.

127 To answer these questions, modeling efforts with a regional climate model (COSMO-  
128 CLM) using reanalysis data as boundary conditions are undertaken. Section 2 describes the  
129 data and the regional model used in this study. In section 3, a short validation of the COSMO-  
130 CLM simulations is carried out and the mechanisms, particularly for secondary cyclogenesis  
131 of Kyrill II, are considered. Section 4 focuses on the move of Kyrill II towards Eastern  
132 Europe and the model resolution dependence of the generation of strong wind gusts along the  
133 distinctive cold front over Northern Germany. A summary and further discussion of the main  
134 results are presented in the final section, section 5.

## 135 2. Data and numerical model

136 The numerical model used for the investigation of Kyrill I and Kyrill II is the non-  
137 hydrostatic regional COSMO model (<http://www.cosmo-model.org>) in its Climate Limited-  
138 area Model version 4.8, subversion 17 (hereafter CCLM; Rockel *et al.*, 2008). The COSMO  
139 model, developed by the German Weather Service (DWD, Deutscher Wetterdienst) is in use  
140 for regional weather prediction by several European weather services. Using an identical  
141 formulation of the dynamical core and physical parameterizations, the only difference  
142 between the CCLM and the operational model version is that neither data assimilation nor  
143 latent heat nudging are performed in the former. The physical parameterizations include  
144 enhanced sub-grid-scale turbulence (Baldauf *et al.*, 2011) based on the level-2.5 scheme by  
145 Mellor and Yamada (1982), longwave and shortwave radiation (Ritter and Geleyn, 1989),  
146 convection (Tiedtke, 1989), and cloud microphysics (Doms *et al.*, 2007).

147 The successful reproduction by the CCLM of windstorms affecting Europe has been  
148 documented e.g. in Born *et al.* (2012) and Ludwig *et al.* (2013). To obtain high-resolution  
149 model output a one-way nesting approach is used with three model resolutions. The model  
150 integrations are all initialized using 6-hourly ERA-Interim reanalysis data (Dee *et al.*, 2011)  
151 as lateral boundary conditions. Therefore, the full T255 spectral resolution is transformed  
152 onto a  $0.75^\circ \times 0.75^\circ$  longitude/latitude grid with 60 layers in the vertical which can be  
153 processed by the numerical model. In a first step, the 6-hourly ERA-Interim data is utilized as  
154 boundary data to force a CCLM run with a horizontal grid spacing of  $0.22^\circ$  (approximately 25  
155 km). The domain covers the North-Atlantic sector and most parts of Europe on a rotated  
156 longitude-latitude grid (Fig. 1 (a)). In a second step the 25 km grid spacing CCLM run  
157 provides boundary conditions for higher resolution CCLM runs with  $0.0625^\circ$  horizontal grid  
158 spacing (approximately 7 km). A final nesting step is undertaken to simulate the cold front  
159 with a convection permitting (i.e. with switched off convection parameterization) horizontal

160 grid spacing of  $0.025^\circ$  (approximately 2.8 km). In addition to the horizontal refinement, the  
161 number of vertical layers is enhanced from 35 (25 km) to 40 (7 km) to 50 (2.8 km),  
162 respectively. Vertical levels are irregularly distributed with height, with highest vertical  
163 resolution in the boundary layer. The coarsest simulation starts at 1200 UTC 16 January and  
164 lasts for 72 hours until 1200 UTC 19 January 2007. Hourly output data is stored for further  
165 analysis. The subsequent high-resolution CCLM simulations are conducted for two different  
166 domains designed to capture the secondary cyclogenesis and passing of the cold front over  
167 Germany, respectively. The investigation of the secondary cyclogenesis proceeds over a  
168 domain centered over the Eastern North Atlantic Ocean (Fig. 1 (a), domain 2a; CCLM  
169 simulation starting at 1800 UTC 16 January). The investigation of the maintenance of Kyrill  
170 II well into Eastern Europe and the vigorous cold front with severe (convective) gusts over  
171 Germany proceeds over a domain centered over continental Europe (Fig. 1 (a), domain 2b;  
172 CCLM simulation starting at 0000 UTC 18 January). Also here hourly output data is stored  
173 for further analysis. Finally, a domain covering Germany (Fig. 1, domain 3) was chosen for  
174 the highest-resolution (convective-permitting) simulation between 1200 UTC 18 January and  
175 0600 UTC 19 January. Here, 15-minute output data is stored to enable a more detailed  
176 analysis, particularly about the structure of the cold front and simulated wind (gusts) fields.

177 To quantify the influence of diabatic heating on the formation of Kyrill II, sensitivity  
178 studies with reduced latent heat release (reduced by 25% (LH75), 50% (LH50), 75% (LH25)  
179 and 100% (LH00)) have been conducted using the coarsest resolution (25 km grid spacing)  
180 model configuration. The reduction of latent heat release (both evaporation/condensation and  
181 fusion/sublimation) is limited to the convection scheme, since separate analysis of convective  
182 and grid scale diabatic heating rates reveals that most of the diabatic heating is through  
183 convection (cf. Fig. 5) in the vicinity of emerging Kyrill II.

184 Potential vorticity (in potential vorticity units, PVU) is calculated as a diagnostic  
 185 quantity using the output of the CCLM simulations. The calculation of potential vorticity on  
 186 isobaric surfaces follows Dickinson *et al.* (1997):

$$PV = -g \frac{\partial \theta}{\partial p} \left( f + \frac{\partial v}{\partial x} - \frac{\partial u}{\partial y} \right) + g \left( \frac{\partial v}{\partial p} \frac{\partial \theta}{\partial x} - \frac{\partial u}{\partial p} \frac{\partial \theta}{\partial y} \right) \quad (1)$$

187 Here,  $g$  is gravity,  $\theta$  represents the potential temperature,  $f$  is the Coriolis parameter,  $p$  is the  
 188 pressure level and  $u$  and  $v$  represent the zonal and meridional components of the wind,  
 189 respectively. To investigate the influence of diabatic heating on the generation of low level  
 190 PV, the diabatic PV rate (DPVR) is computed following Equation (2) of Joos and Wernli  
 191 (2012), converted to pressure as the vertical coordinate (see also Martin, 2006):

$$DPVR = \frac{d}{dt} PV \approx -g \eta_p \frac{\partial}{\partial p} (DHR) \quad (2)$$

192 where  $\eta_p$  is the vertical component of the absolute vorticity and DHR the total (convective and  
 193 non-convective) diabatic heating rate obtained from the CCLM simulations.

194 The along-front stretching deformation (following Renfrew *et al.*, 1997) is used to  
 195 investigate the kinematic environment of the front where Kyrill II forms and is calculated as:

$$E_{str} = \frac{\partial v}{\partial y_f} \quad (3)$$

196 Since stretching deformation is a non-Galilean invariant quantity, the coordinates are rotated  
 197 into a frontal coordinate system with  $y_f$  representing the along-front direction. Here, the  
 198 simulated (or “observed”) wind field is used, which is a simplification compared to Bishop  
 199 (1996) who considered a separation into frontal and environmental wind fields. Although the  
 200 calculation of the stretching deformation by means of the observed wind field exhibits higher  
 201 variation with regard to the frontal orientation (Renfrew *et al.*, 1997), this approach permits to  
 202 evaluate qualitatively if the kinematic environment along the front is favorable for the  
 203 development of a frontal cyclone. In addition, the frontogenesis function (Petterssen, 1936),

204 including horizontal divergence and the total deformation, is used to investigate whether the  
 205 wind field is frontogenetic or frontolytic. Following Keyser *et al.* (1988), the frontogenesis  
 206 parameter is physically a good choice since frontogenesis is partitioned between fundamental  
 207 kinematic quantities that are invariant with respect to coordinate transformations.

208 As stated in Section 1, a detailed analysis of the mesoscale features associated with the  
 209 cold front of Kyrill II on 18 January is one of the objectives of this study. Wind and gust data  
 210 from 121 Stations from German Weather Service (DWD) for the period between 1200 UTC  
 211 17 January and 1200 UTC 19 January are considered. To analyze the gusts along the strong  
 212 cold front, the gradient Richardson number ( $Ri$ ) is used to characterize whether the boundary  
 213 layer flow is turbulent ( $Ri < 0.25$ ) or stable ( $Ri > 1.0$ ) (e.g. Schrage and Fink, 2012). A  
 214 gradient Richardson number in the range  $0.25 < Ri < 1.0$  marks the transition between stable  
 215 and turbulent flow:

$$Ri = \frac{\frac{g}{T_v} \frac{\partial \theta_v}{\partial z}}{\left(\frac{\partial u}{\partial z}\right)^2 + \left(\frac{\partial v}{\partial z}\right)^2} \quad (4)$$

216 Here,  $T_v$  the virtual temperature,  $\theta_v$  the virtual potential temperature, and  $z$  is height.

217 Furthermore, two different diagnostic gust parameterizations for wind gust estimation  
 218 (both already implemented in CCLM) are considered to obtain area-wide gust distributions at  
 219 high resolution. The standard method for estimating gusts in the CCLM (Schulz and Heise,  
 220 2003; Schulz, 2008) depends on the wind speed at 30 m height and the friction velocity  $u_*$ :

$$v_{DWD} = |v_{30m}| + 3.0 \cdot 2.4 \cdot u_* \quad (5)$$

221 with the empirical factors 3.0 and 2.4 motivated by Prandtl-layer theory (Panofsky and  
 222 Dutton, 1984). In the alternative TKE approach (see Born *et al.*, 2012 for a detailed  
 223 description), the relation between mean TKE, denoted  $\bar{q}$ , and gusts,  $v_{TKE}$ , is

$$v_{TKE} = \sqrt{2E_{max}} = \bar{v} + 2\sqrt{\bar{q}} + \varepsilon_v, \quad (6)$$

224 where  $E_{max}$  is the maximum kinetic energy,  $\bar{v}$  the mean wind speed (30m above surface) and  
225  $\varepsilon_v$  is the stochastic subgrid-scale part of  $v_{max}$ .

### 226 **3. General model performance and development of the secondary cyclone**

#### 227 *(a) Validation of the CCLM Simulations*

228 In this subsection, the CCLM simulated cyclone tracks and intensities and the synoptic-  
229 scale structure are validated for the Kyrill case. Figure 2 shows a comparison of the cyclone  
230 tracks (Fig. 2 (a)) and core pressure evolution (Fig. 2 (b)) of Kyrill I and Kyrill II obtained  
231 from the CCLM with 25 km and 7 km grid spacing and ERA-Interim data. The simulations  
232 reproduce the storm with reasonable skill. The location of Kyrill I and II at the point where  
233 they co-exist is shifted slightly to the west (more so in the 25 km grid spacing simulation), but  
234 both the coarse and fine resolution simulations reproduce the track of Kyrill II very well. The  
235 evolution of core pressure shows an earlier pressure minimum for both simulations than in the  
236 reanalysis. However, the simulation data is available each hour; when comparing six-hourly  
237 values only, the timing of the pressure minimum is the same as in the reanalysis. The core  
238 pressure of the 7 km grid spacing simulation reaches a slightly deeper minimum than that of  
239 the 25 km simulation for both Kyrill I and II.

240 In Figure 3, the synoptic-scale structure of the 25 km grid spacing simulation of the  
241 evolution of Kyrill is depicted. A latitudinal band of strong wind speed (locally exceeding 90  
242  $\text{m s}^{-1}$ ) marks the upper-tropospheric jet stream on 1200 UTC 17 January (Fig. 3 (a)), 0000  
243 UTC 18 January (Fig. 3 (b)) and 1200 UTC 18 January (Fig.3 (c)). The corresponding surface  
244 cyclone location (mean sea level pressure in Fig. 3 (g)-(i), marked by Arabic numbers ‘1’ and  
245 ‘2’ throughout Figure 3) indicates a favorable location relative to the upper-level jet stream;  
246 the surface cyclone is situated underneath the left exit region of the jet streak, known to be a  
247 favorable location for upper-level divergence (cf. Fig. 4 (a), (b)) (e.g. Uccellini and Johnson,  
248 1979). Together with the eastward moving jet stream, a dry intrusion develops (cf. Fig. 3 (c),

249 (f), (i) in Fink *et al.*, 2009) with its tip on this 500 hPa surface following the position of the  
250 surface cyclone beneath (Fig. 3 (d)-(f)) towards Central Europe. The dry intrusion is  
251 characterized by i) low values of the specific humidity and ii) by high PV values, indicating  
252 descending air from the tropopause region. The 850 hPa  $\theta_e$  field (Fig. 3 (g)-(i)) shows the  
253 incorporation of warm and humid air masses at the southern flank of the cyclone, potentially  
254 providing energy to the storm in terms of latent heat release if this boundary-layer air is lifted.  
255 The sensitivity of the development of strong extratropical cyclones to warm and humid air  
256 masses has already been demonstrated by Danard (1964) and Gall (1976), and more recently  
257 by Fink *et al.* (2012), Dacre and Gray (2013), Ludwig *et al.* (2013) and Doyle *et al.* (2014).  
258 To summarize, the CCLM simulations provide realistic features in terms of large-scale  
259 atmospheric patterns and temporal storm development and thus are suitable for further  
260 investigation of this secondary cyclogenesis event and storm relevant details.

#### 261 *(b) Development of the secondary cyclone Kyrill II*

262 In this subsection, the focus is on the mechanism and location of the secondary  
263 cyclogenesis and thus the formation of Kyrill II. Results shown here are derived from the 7  
264 km grid spacing CCLM simulation covering domain 2a. Figure 4 shows selected model fields  
265 at 0000 UTC and 0600 UTC 18 January. At upper levels (300 hPa), the eastern edge of the  
266 strong jet stream with wind speeds up to  $80 \text{ m s}^{-1}$  is located over the British Isles (Fig. 4 (a),  
267 (b)). Maximum values of upper-level divergence exceeding  $6 \times 10^{-5} \text{ s}^{-1}$  are found in the left exit  
268 region of the jet streak. This region is therefore favorable for surface pressure falls, rising  
269 motion, and latent heat release in the ascending air stream; all of these are favorable for the  
270 intensification and maintenance of a low-level cyclone. Over the Atlantic Ocean, simulated  
271 wind speeds are even faster (exceeding  $90 \text{ m s}^{-1}$ ). The western parts of the domain (up to the  
272 location where Kyrill II emerges at the occluded front of Kyrill I) are characterized by  
273 negative (frontolytic) stretching deformation of the horizontal wind field at 900 hPa (Fig. 4

274 (c)) (for clarification of frontal boundaries, surface analysis charts from DWD are included;  
275 Fig. 4 (i), (j)). Frontolytic stretching deformation along a low-level PV band favors the  
276 breaking up of the PV band (Dacre and Gray, 2006) and thus supports secondary cyclogenesis  
277 (Parker, 1998a, b). Before (not shown) and during the development of Kyrill II, the band of  
278 negative stretching deformation is coherent in the region of the emerging low-pressure center  
279 (Fig. 4 (c)) potentially leading to several separated PV maxima. Additionally, the  
280 frontogenesis parameter (Pettterssen, 1936) is negative in the vicinity of emerging Kyrill II,  
281 documenting that the environmental flow is frontolytic (not shown). Six hours later, the PV  
282 band broadens as Kyrill II intensifies (Fig. 4 (d)), mainly due to continuing diabatic heating  
283 along the occluded front (cf. Fig 5 (a), (b)) Additionally, negative stretching deformation  
284 remains in the vicinity of Kyrill I, leading to the dissipation of the associated PV band. Figure  
285 4 (e) and (f) shows the distribution of warm and humid air masses along the occluded front.  
286 The convergence of the ageostrophic wind component along the PV band implies lifting of  
287 these air masses and their relevance for the development of Kyrill II. The cold front extending  
288 southwestwards from the eastern edge of the low-pressure center towards 50°N, 20°W in Fig.  
289 4 (g), (h) is associated with a cyclonic wind shift but, unlike the warm front, it is only weakly  
290 active with minimal precipitation at the times shown. At the intersection of the warm and the  
291 cold front the triple point is marked by the strongest precipitation rates (Fig. 4 (g), (h)). Since  
292 the triple point is southeast of the region where Kyrill II develops, we state that Kyrill II  
293 develops along the occluded front of the parent low Kyrill I (a rare case not described in  
294 Parker (1998a) but mentioned e.g. in Neiman *et al.*, (1993)). Kyrill fits nicely into the type 2  
295 category of the secondary cyclone classification scheme defined by Ayrault *et al.* (1995); this  
296 type is characterized by a strong warm front and frontolytic flow.

297         The evaluation of east-west and north-south orientated vertical cross sections centered  
298 along the cyclone center provides further insights into the environmental characteristics  
299 during secondary cyclogenesis. Figure 5 (a) shows vertically orientated regions of strong

300 diabatic heating rates (DHRs) and enhanced PV extending along the occluded front. The  
301 strong DHRs along the occluded front, where warm air has been lifted, are associated with the  
302 region of intensive precipitation (cf. Figure 4 (g)). Slightly west of 20°W, a narrow band of  
303 strong DHRs is located in the vicinity of emerging Kyrill II, which is also visible in a north-  
304 south cross section at the same time (Fig 5 (c)). Aloft of emerging Kyrill II, a coherent region  
305 of enhanced PV, associated with strong DHRs, is obvious up to 700 hPa. The region with  
306 strong DHRs between 51°N and 52°N is associated with the trailing cold front of Kyrill I. Six  
307 hours later, Kyrill II is located at 54.8°N and 9.2°W, Aloft, enhanced PV and strong DHRs  
308 co-exist, consistent with a hypothesized continued role of diabatic forcing in the  
309 intensification of Kyrill II (Fig. 5 (b), (d)). During the intensification, the dynamic tropopause  
310 has locally descended down to 650 hPa.

311 Separation of the convective and grid scale DHRs reveals that latent heat release by  
312 convective processes played the major role during the formation of Kyrill II. The narrow  
313 vertical strip of strong DHRs above the surface cyclone disappears when only grid scale latent  
314 heat release is considered (Fig. 5 (e), (f)). The importance of diabatic heating on the  
315 generation of low-level PV is also obvious in Fig. 5. The co-location of high values of  $\eta_p$  and  
316 a downward decrease in DHR causes high diabatic PV generation (cf. Equation 2) below 800  
317 hPa on 0000 UTC 18 January 2007 in the area where Kyrill II developed (Fig. 5 (g)). A  
318 separate analysis of convective and non-convective DHRs reveals a clear dominance of  
319 convective over non-convective (grid-scale) generation of PV (not shown). At 0600 UTC the  
320 maximum of  $\eta_p$  tilts away from the DHR maximum in the vertical, thereby reducing DPVR.  
321 Even though the DPVR is reduced at 0600 UTC (Fig. 5 (h)), the same conclusions can be  
322 drawn as for 0000 UTC. This motivated a set of sensitivity experiments with the coarsest  
323 resolution model configuration (25 km grid spacing) in which latent heat release is reduced,  
324 but only in the convective parameterization scheme. Results of the sensitivity experiments are  
325 summarized in Figure 6. The locations of the first co-existence of Kyrill I and Kyrill II are

326 depicted in Fig. 6 (a); the formation of Kyrill II (defined as the first closed isobar with 1 hPa  
327 interval based on the hourly model output) is retarded by about three hours in the sensitivity  
328 experiments. Likewise, a shift to the east of Kyrill II is discernable with decreasing latent heat  
329 release (except for the LH50 experiment). The decrease of latent heat release also leads to a  
330 systematic weakening of the mean sea level pressure minima for Kyrill I (Fig. 6 (b)) being  
331 strongest for LH00 with 4.5 hPa. The reduction of the mean sea level pressure minima for  
332 Kyrill II is considerably stronger than for Kyrill I (Fig. 6 (c)). At the formation time of Kyrill  
333 II, the difference between CNTRL and LH00 amounts to 7.5 hPa. Also the subsequent  
334 development of Kyrill II is weaker throughout the sensitivity experiments, leading to a  
335 maximum difference in mean sea level pressure minimum between CNTRL and LH00 of 17.1  
336 hPa at 1700 UTC 18 January. The additional DPVR diagnostics, together with the sensitivity  
337 studies with reduced diabatic heating through convection, lends more credence to our  
338 hypothesis that diabatic processes played an important role on the formation of Kyrill II.  
339 Nevertheless, since Kyrill II evolves even under zero latent heating in the convection scheme,  
340 diabatic processes are not able to explain the formation of Kyrill II entirely. Additional  
341 analyzes of the 300-hPa isotachs and divergence fields verify that the upper-level kinematic  
342 environment for the control simulation and the sensitivity studies are indeed similar, such that  
343 observed differences in cyclogenesis are likely not related to differences in the upper-level  
344 forcing (not shown). Thus, we conclude that the differences between the experiments are very  
345 unlikely to be due to the small differences in the upper-level conditions, thus supporting our  
346 hypothesis that the diabatic heating plays an important role for the secondary cyclone  
347 development. The role of combined upper-level forcing by the split jet stream is left to further  
348 research.

349 In summary, we have shown evidence that the formation of Kyrill II proceeds (i) along  
350 the occluded front, (ii) in a frontolytic environment with negative stretching deformation of  
351 the horizontal wind field and (iii) is supported by diabatic processes in the mid and

352 particularly lower troposphere hypothetically in conjunction with a developing upper-level  
353 trough.

#### 354 **4. Passing of Kyrill II over Central Europe**

##### 355 *(a) High resolution simulations with COSMO-CLM*

356 In the following hours, the storm moved further towards Europe. An overview of the  
357 upper-tropospheric conditions that maintained the deep core pressure of Kyrill II (Fig. 1)  
358 while it passed over Central Europe is presented using the 7 km horizontal grid spacing  
359 simulation over domain 2b. At 1500 UTC 18 January the core of the upper-level jet stream  
360 (wind speeds  $>80 \text{ m s}^{-1}$ ) is located over the British Isles heading towards eastern parts of  
361 Germany (Fig. 7 (a)). At this time strong upper-level winds exceeding  $50 \text{ m s}^{-1}$  are already  
362 located over northern and central Germany. As already hypothesized in Fink et al. (2009), the  
363 coexistence of a second jet streak over the Baltic States leads to very strong upper-level  
364 divergence between the exit and entry regions of both jet streaks and is assumed to play a  
365 crucial role for the maintenance of the long lasting deep core pressure of Kyrill II. In the  
366 following three to six hours (Fig 7 (b) and (e), (c) and (f)), the shortwave disturbance and  
367 associated jet streaks are observed to move downstream towards central Europe, exceeding  
368 wind speeds of  $80 \text{ m s}^{-1}$  at 2100 UTC over Benelux and eastern parts of Germany. During this  
369 period, the upper-level divergence remains strong between the two jet streaks and Kyrill II  
370 moves along with the short-wave trough towards the east (Figure 7 (g)-(i)), reaching  
371 simulated minimum mean sea level pressures of 961.1 hPa, 961.3 hPa and 963.0 hPa at 1500  
372 UTC, 1800 UTC and 2100 UTC respectively. The frontal structures are analyzed by  
373 considering the precipitation and maximum wind gust (here  $v_{DWD}$ ) for each preceding hour.  
374 The warm front is characterized by uniform large-scale precipitation with hourly-averaged  
375 precipitation rates hardly exceeding  $3 \text{ mm h}^{-1}$ . In contrast, the cold front is characterized by a  
376 narrow band of both large resolved grid-scale and parameterized hourly-averaged convective

377 precipitation rates exceeding  $7 \text{ mm h}^{-1}$  (grid points with parameterized convective  
378 precipitation are marked by red dots). Convective precipitation is also simulated by CCLM  
379 behind the cold front, a region where it is typically observed. Simulated wind gusts are  
380 partitioned into convective and non-convective types (grid points with convective gusts  $> 25$   
381  $\text{m s}^{-1}$  are marked by black dots, Figure 7 (j)-(l)). At 1500 UTC, convective gusts are  
382 predominantly located south of the cyclone center, with only a few convective gusts simulated  
383 along the cold front. At 1800 UTC, an increased number of grid points exhibit convective  
384 gusts, mainly at the western tail of the cold front. Maximum gusts exceeding  $40 \text{ m s}^{-1}$  are  
385 simulated all along the northern shoreline of the North Sea. Along the cold front, isolated grid  
386 points have gusts exceeding  $40 \text{ m s}^{-1}$  with only few of them being convective in nature. At  
387 2100 UTC, strongest wind gusts appear in the region with enhanced pressure gradient close to  
388 the west and south west of the cyclone center. The cold front, located along the German-  
389 Czech border, is still associated with widespread severe wind gusts exceeding  $40 \text{ m s}^{-1}$ ,  
390 particularly over the high mountain ranges of the Ore Mountains at this time.

391 The simulation with highest resolution (grid spacing 2.8 km, domain 3) provides a more  
392 detailed view of the cold front passing Germany between 1700 UTC and 1900 UTC. Narrow  
393 bands of strong simulated radar reflectivity exceeding values of 50 DBZ are aligned with the  
394 cold front (Figure 8 (a)-(c)). This is in good agreement with measured radar reflectivity as  
395 shown in Fink *et al.* (2009, their Figure 5). The areas with highest reflectivity are associated  
396 with strong updrafts in excess of  $0.75 \text{ m s}^{-1}$  and hourly-averaged precipitation rates exceeding  
397  $10 \text{ mm h}^{-1}$  (Fig. 8 (g)-(i)). The dry intrusion is situated directly behind the cold front during  
398 the period shown; the cold front is marked by strong simulated reflectivity. At 1700 UTC, the  
399 area beneath the dry intrusion is nearly free of precipitation. Weak post-frontal reflectivity is  
400 simulated near the North Sea coast, associated with weak hourly-averaged precipitation rates  
401 ( $< 3 \text{ mm h}^{-1}$ ). Gustiness associated with the cold front is shown in Figure 8 (d)-(f).  
402 Additionally, the locations of the three verified tornado reports over Eastern Germany (cf.

403 ESWD database, Dotzek *et al.*, 2009) are plotted on the maps. The first tornado (F2) was  
404 reported at Meseberg (52.96°N, 13.12°E) at 1730 UTC, followed by the second (F3) near  
405 Lutherberg (51.87°N, 12.65°E) at 1740 UTC and the third (also F3) at Lauchhammer  
406 (51.51°N, 13.94°E) at 1830 UTC. The strongest wind gusts are located below the left exit  
407 region of the upper-level jet stream. As stated by Rose *et al.* (2004), rising motions below  
408 left-exit quadrants of a jet streak are associated with the development of convection and  
409 severe weather. Their 10-year climatology reveals tornadoes primarily occur within the two  
410 exit quadrants of the jet stream, with the left-exit quadrant favored over the right-exit  
411 quadrant. The investigated case of Kyrill II is consistent with this climatology, as the  
412 observed tornadoes are located below the left exit region of the simulated jet stream.  
413 Additionally, the upper-level jet stream exhibits weak cyclonic curvature. In the case of  
414 cyclonic curvature, divergence in the left-exit region becomes amplified (Moore and  
415 Vanknowe, 1992). The observed tornado events are also within the region with the strongest  
416 simulated wind gusts, radar reflectivity and upward motion at the corresponding times.

417 *(b) Physical mechanisms associated with peak wind gusts along the cold front*

418 A detailed analysis of the mesoscale features associated with the cold front of Kyrill II  
419 over Germany on 18 January is presented in this sub-section. To evaluate in detail the nature  
420 of gusts and infer the areas potentially affected by strong downdrafts, two times are  
421 considered to characterize the conditions at different locations along the cold front,  
422 particularly at lower tropospheric levels: 1645 UTC (Fig. 9) and 1800 UTC (Fig. 10). At 1645  
423 UTC, the cold front extends from the federal state of North-Rhine Westphalia (NRW) towards  
424 Berlin (B) in northeasterly direction (Fig. 9 (e), federal state names included). While the cold  
425 front, here identified as the region with strong horizontal  $\theta_e$  gradient, is rather fragmented  
426 over NRW, the front is sharpened further to the east (Fig. 9 (e)). The regions with the  
427 strongest wind gusts, exceeding  $32.7 \text{ m s}^{-1}$  (definition of hurricane force winds), are mainly

428 located behind (north of) the front (see also Fig. 8 (d)-(f)). The vertical profiles at 6.76°E and  
429 51.28°N (near station Düsseldorf, WMO No. 10400, where the highest (40 m s<sup>-1</sup>) lowland  
430 wind gust was reported) reveal favorable lower-tropospheric conditions for the generation of  
431 the severe surface wind gusts; simulated gusts reached 34.3 m s<sup>-1</sup> at that time. The low values  
432 of gradient Richardson number below 850 hPa and maximum values of TKE below 900 hPa  
433 (TKE profiles before and afterwards ( $\pm$  30 and 60 minutes) show less TKE near the ground,  
434 not shown) imply that the boundary layer flow is turbulent (Fig 9 (a)). This lower-  
435 tropospheric region is generally associated with subsiding of air (Fig. 9 (b)). Slightly negative  
436 values of the temperature difference due to latent heating reveal only a weak impact of  
437 evaporative cooling at this grid point (Fig 9 (b)). The vertical profile of horizontal wind speed  
438 shows boundary layer winds exceeding 45 m s<sup>-1</sup> above about 850 hPa (Fig. 9 (c)). Based on  
439 vertical profiles of  $\theta$  and  $\theta_e^*$  (equivalent potential temperature of saturated air), the lower  
440 troposphere exhibits weak dry static stability but conditional instability ( $d\theta_e^*/dz < 0$ ) between  
441 the surface and 875 hPa (Fig 9 (d)). Thus, favorable environmental conditions for mixing high  
442 momentum from higher layers down to the surface exist. A south to north orientated cross  
443 section normal to the cold front clearly shows the cross frontal circulation (Fig. 11 (a)). At  
444 low levels, strong convergence dominates leading to ascending motions above the surface  
445 cold front (surface cold front marked by sharp horizontal gradient of  $\theta_e$  sloping upward and  
446 northward above 875 hPa). The upward motion in the frontal region is limited to below the  
447 650 hPa level. The layer below 900 hPa is entirely turbulent ahead and behind the cold front  
448 ( $Ri < 0.25$ ). Thus, a combination of broadly subsiding motion and high values of horizontal  
449 momentum (wind speeds exceed 45 m s<sup>-1</sup> at 900 hPa) is suggested to account for the severe  
450 surface wind gusts also ahead (south) of the cold front (Fig. 9 (e)).

451 Conditions at 1800 UTC (Fig. 10) are somewhat similar to those at 1645 UTC although  
452 the cold front has intensified, as indicated by a sharpened  $\theta_e$  gradient (Fig. 10 (e)). Severe  
453 wind gusts are mainly concentrated to northern parts of Thuringia. Vertical profiles of TKE

454 and  $Ri$  at  $10.5^{\circ}\text{E}$  and  $51.28^{\circ}\text{N}$  (where simulated surface wind gusts reach  $36.0\text{ m s}^{-1}$ ) provide  
455 evidence that the flow is turbulent up to 825 hPa (Fig 10 (a)) and is associated with enhanced  
456 subsiding motion, being strongest at 875 hPa (Fig 10(b)). The main contrast to the  
457 environmental conditions at the earlier time (discussed previously) is a strong increase in  
458 evaporative cooling and associated increased subsidence at lower-tropospheric levels; this  
459 contributes to the downward mixing of high momentum towards the ground, producing strong  
460 surface wind gusts. At the same time, the vertical profile of the horizontal wind exhibits  
461 maximum wind speeds exceeding  $50\text{ m s}^{-1}$  at 875 hPa (Fig 10(c)). As previously, the lower  
462 troposphere indicates weak dry static stability but conditional instability (Fig 10(d)). A  
463 comparison of simulated profiles with radiosonde profiles at 1800 UTC at Lindenberg (WMO  
464 10393) reveals that the simulated stabilities are reliable (not shown). The vertical cross  
465 section (Fig. 11 (b)) confirms the intensification of the cold front. The  $\theta_e$  gradient has  
466 increased considerably and there is deep vertical ascent up to at least 600 hPa. Again, the  
467 ascent is favored by low-level convergence and upper-level divergence of the front normal  
468 wind component. The thickness of the turbulent flow layer has increased, reaching up to about  
469 850 hPa. The transition layer of stable to turbulent flow partly extends up to 750 hPa. To  
470 summarize, conditions are favorable to produce strong surface wind gusts by mixing down  
471 existing high momentum within a turbulent and conditionally unstable environment.  
472 Additional analyses of large-scale environmental parameters like convective available  
473 potential energy, storm relative helicity and vertical wind shear at 1800 UTC (not shown)  
474 revealed that the potential for convective severe weather was given (e.g., Romero *et al.*,  
475 2007).

476 Since the physical mechanisms leading to strong wind gusts were analyzed at only two  
477 specific grid points and times (see above), the representation of area-wide simulated wind  
478 gusts is now considered. The maximum simulated gust from two wind gust estimation  
479 methods ( $v_{\text{DWD}}$ ,  $v_{\text{TKE}}$ ) for the whole simulated period (1200 UTC 18 January to 0600 UTC 19

480 January) at each grid point of the convection-permitting simulation is compared to the  
481 maximum observed gust at stations for the same period (Fig. 12). While the patterns for both  
482 methods are quite similar, the maximum  $v_{TKE}$  gusts (Fig. 12 (b)) are consistently weaker than  
483 the maximum  $v_{DWD}$  gusts (Fig. 12(a)). Compared to the maximum observed gust,  $v_{DWD}$  is  
484 overestimating gusts in both coastal and interior regions. In contrast, results of  $v_{TKE}$  especially  
485 at coastal regions match observations with considerable skill. Additionally, both methods  
486 underestimate gusts at mountain peaks e.g. at Brocken (51.8°N, 10.62°E, 1141 m a. s. l). A  
487 comparison with insurance losses for winter storm Kyrill (cf. Fig. 6 in Donat *et al.*, 2011)  
488 indicates that regions with strong wind gusts and high losses are in good accordance.  
489 Although both wind gusts estimation methods have been developed and tested for coarse grid  
490 spacing, it is shown that both methods are suitable also for convection-permitting simulations.  
491 To conclude, the two different wind gust estimates are able to provide realistic area-wide and  
492 temporal wind gust distributions for windstorm Kyrill and provide evidence that strong wind  
493 gusts occurred over a large area in Germany and nearby countries during the afternoon of 18  
494 January 2007.

## 495 5. Summary and Discussion

496 The formation of a secondary cyclone along the occluded front and strong wind gusts  
497 associated with severe winter storm Kyrill (January 2007) are examined using (high  
498 resolution) regional model simulations with COSMO-CLM. The objectives addressed in this  
499 study are i) to document the kinematic environment and dynamical forcing leading to the  
500 uncommon formation of the secondary cyclone Kyrill II along the occluded front of parent  
501 low Kyrill I, ii) to quantify the influence of diabatic processes on the intensity of Kyrill II, and  
502 iii) to characterize the boundary layer conditions to determine the cause of the strong wind  
503 gusts along the cold front over Germany. Kyrill underwent explosive cyclogenesis over the  
504 North Atlantic Ocean as it crossed the strong upper-tropospheric jet stream. The formation of

505 the secondary low Kyrill II, which moved further towards continental Europe, led to serious  
506 socio-economic impacts over large parts of Central and Eastern Europe (Fink *et al.*, 2009). A  
507 split upper-level jet structure with accompanied upper-level divergence supported the  
508 maintenance of Kyrill II during its eastward movement. The importance of a split jet structure  
509 to cyclone development and maintenance has already been ascertained for recent windstorms  
510 such as Lothar (1999), Klaus (2009) and Xynthia (2010) (Wernli *et al.*, 2002; Fink *et al.*,  
511 2012; Ludwig *et al.*, 2013). While existing studies of secondary cyclogenesis along trailing  
512 fronts of a parent cyclone are limited mainly to cyclogenesis along warm and cold fronts (e.g.  
513 Rivals *et al.*, 1998; Thorncroft and Hoskins, 1990), Kyrill II evolves along the occluded front  
514 of mature cyclone Kyrill I. This type of secondary cyclogenesis is apparently a very rare event  
515 but has been mentioned by Neiman *et al.* (1993). Nevertheless, the mechanisms leading to the  
516 formation of Kyrill II are comparable with other cases of frontal cyclogenesis (Parker, 1998a;  
517 Dacre and Gray, 2006). A narrow band with high-PV values aligned along the occluded front  
518 exists at lower levels. If stretching deformation along the front is above a critical threshold,  
519 the deformation flow will sharpen the front. However, if the stretching deformation is reduced  
520 or negative, the PV strip is able to break up into multiple PV anomalies with corresponding  
521 cyclonic circulations. Consequently, the circulations extend towards the surface and are able  
522 to form waves along the front (cf. Dacre and Gray, 2006, their Figure 1). In the case of Kyrill  
523 II, the along-front stretching deformation (Renfrew *et al.*, 1997) along the occluded front  
524 exhibits negative values and thus, together with a frontolytic environment, promotes the break  
525 up of the PV band at 0000 UTC 18 January (cf. Fig. 4 (c)) when Kyrill II forms. Also, strong  
526 diabatic heating rates exist, leading to increased diabatic PV modification near the point  
527 where Kyrill II evolves. Merging with the upper-level dry intrusion, which exhibits high  
528 values of PV, a PV tower formed across the depth of the troposphere and was enhanced  
529 during the ongoing development (Fig. 5 (d)). The importance of diabatic heat release and the  
530 accompanying formation of a vertical extended PV tower during cyclone development have

531 been described in several studies (e.g. Rossa *et al.*, 2000, Wernli *et al.*, 2002, Čampa and  
532 Wernli, 2012, Ludwig *et al.*, 2013). Sensitivity studies with reduced latent heat release within  
533 the convection parameterization scheme reveal the importance of diabatic forcing during the  
534 formation of Kyrill II. With reduced latent heat release, the development of Kyrill II is  
535 retarded, leading to a less intense cyclone over Central Europe. However, the fact that a  
536 secondary cyclone still developed implies that other factors (e.g. forcing from the split upper-  
537 tropospheric jet stream) also contributed to the secondary development; the quantification of  
538 this upper-tropospheric forcing is left for further research. To summarize, the realistic  
539 simulation of the uncommon secondary cyclogenesis of windstorm Kyrill with COSMO-CLM  
540 provides new insights into crucial (thermo-) dynamical aspects of the formation of Kyrill II  
541 along the occluded front of the mature cyclone Kyrill I.

542         The convection-permitting simulation (2.8 km grid spacing) of Kyrill II's cold front  
543 provides insight into dynamical aspects of the severe wind gusts along the front. The  
544 simulation reproduces realistic features observed during the passage over Germany (e.g. the  
545 simulated lines of maximum radar echoes; cf. Figure 5 in Fink *et al.*, 2009). The simulated  
546 gusts along the cold front often exceed hurricane force wind speeds, as observed. The location  
547 of the observed tornadoes, below the left exit region of the upper-tropospheric jet stream, is  
548 known to be favorable for severe weather (Rose *et al.*, 2004). The vertical state of the lower  
549 atmosphere during the passage of the cold front was analyzed at two grid points to determine  
550 the physical mechanisms causing the wind gusts. While the boundary layer shows weak dry  
551 static stability ( $d\theta/dz \geq 0$ ), the vertical gradient of  $\theta_e^*$  implies that the troposphere below 875  
552 hPa is conditionally unstable ( $d\theta_e^*/dz < 0$ ). Also, the small values of gradient Richardson  
553 number and maximum values of TKE near the ground characterize the boundary layer flow to  
554 be turbulent. The consideration of the diabatic heating rates implies that evaporative cooling  
555 occurs together within the downward motions contributing to the amplification of surface  
556 wind gusts. Thus, the strong gusts are embedded in a weak statically stable, conditionally

557 unstable and turbulent environment where it is feasible that high momentum (wind speeds  
558 above 850 hPa exceed  $45 \text{ m s}^{-1}$ ) is mixed downward towards the surface. Although strong  
559 wind conditions are generally associated with weak static stability, the prevalence of  
560 conditional instability in cases similar to the current situation is not known and thus might be  
561 an avenue for further research.

562 The realistic representation of the physical mechanism causing strong wind gusts by the  
563 COSMO-CLM permits the area-wide assessment of wind gusts at high temporal coverage.  
564 The realistic representation of wind gusts during windstorm events at high resolution (here  
565 calculated using two different wind gust estimation approaches) is of particular interest for a  
566 range of impact studies (e.g., forest and private household losses) and to enhance the  
567 predictability of such events. For storm Kyrill there is evidence of widespread strong wind  
568 gusts during the passage of the cold front over Germany and nearby countries, both from wind  
569 gust measurements and resulting insurance losses (cf. Fig. 6 in Donat *et al.*, 2011).

570 The present study provides evidence of the anomalous characteristics of storm Kyrill,  
571 including the secondary development along the occluded front and the severe cold front over  
572 Central Europe, both quite uncommon occurrences according to the current literature. Future  
573 work could focus on the analysis of similar storms (e.g. winter storm Emma in March 2008  
574 for another cold-season derecho, cf. Gatzen *et al.*, 2011) to identify how rare such  
575 developments actually are and potentially to enhance their predictability.

## 576 **Acknowledgments:**

577 We thank the European Centre for Medium-Range Weather Forecasts (ECMWF, UK)  
578 for providing the ERA-Interim reanalysis data and the German Weather Service (DWD) for  
579 providing synoptic station data. We thank the German Climate Computer Centre (DKRZ,  
580 Hamburg) for computer and storage resources within the context of DKRZ project ANDIVA

581 (Nr. 105). We thank Helen Dacre and John Methven (both Univ. Reading) for discussions.

582 We thank the editor David Schultz and four anonymous reviewers for their constructive

583 comments on an earlier version of the manuscript.

584

585 **References**

- 586 Ayrault, F., F. Lalaurette, A. Joly, and C. Loo, 1995: North Atlantic ultra high frequency  
587 variability. An introductory survey. *Tellus A*, **47**, 671–696.
- 588 Baldauf, M., A. Seifert, J. Förstner, D. Majewski, M. Raschendorfer, and T. Reinhardt, 2011:  
589 Operational Convective-Scale Numerical Weather Prediction with the COSMO Model:  
590 Description and Sensitivities. *Mon. Wea. Rev.*, **139**, 3887–3905.
- 591 Bishop, C. H. and A. J. Thorpe, 1994a: Frontal wave stability during moist deformation  
592 frontogenesis. Part I: Linear wave dynamics. *J. Atmos. Sci.*, **51**, 852–873.
- 593 Bishop, C. H. and A. J. Thorpe, 1994b: Frontal wave stability during moist deformation  
594 frontogenesis. Part II: The suppression of nonlinear wave development.  
595 *J. Atmos. Sci.*, **51**, 874–888.
- 596 Bishop, C. H., 1996: Domain-Independent Attribution. Part I: Reconstructing the Wind from  
597 Estimates of Vorticity and Divergence Using Free Space Green's Functions. *J. Atmos. Sci.*,  
598 **53**, 241–252.
- 599 Born K., P. Ludwig, and J. G. Pinto, 2012: Wind gust estimation for Mid-European winter  
600 storms: towards a probabilistic View. *Tellus A* **64**:17471
- 601 Brasseur, O., 2001: Development and application of a physical approach to estimating wind  
602 gusts. *Mon. Wea. Rev.* **129**, 5–25.
- 603 Browning, K. A., and R. Reynolds, 1994: Diagnostic study of a narrow cold-frontal rainband  
604 and severe winds associated with a stratospheric intrusion. *Quart. J. Roy. Meteor. Soc.* **120**,  
605 235-257.
- 606 Browning, K. A., and B. W. Golding, 1995: Mesoscale aspects of a dry intrusion within a  
607 vigorous cyclone. *Quart. J. Roy. Meteor. Soc.*, **121**, 463–493.
- 608 Browning, K. A., 1997: The dry intrusion perspective of extra-tropical cyclone development.  
609 *Met. Apps.*, **4**, 317–324.
- 610 Čampa, J., and H. Wernli, 2012: A PV perspective on the vertical structure of mature  
611 midlatitude cyclones in the Northern Hemisphere. *J. Atmos. Sci.*, **69**, 725-740.
- 612 Carlson, T.N, 1991: Mid-latitude weather systems. Harper Collins, London, pp 507.

613 Carrera, M. L., J. R. Gyakum, and D. -L. Zhang, 1999: A numerical case study of secondary  
614 marine cyclogenesis sensitivity to initial error and varying physical processes. *Mon. Wea.*  
615 *Rev.*, **127**, 641–660.

616 Chaboureau, J. -P. and A. J. Thorpe, 1999: Frontogenesis and the development of secondary  
617 wave cyclones in FASTEX. *Quart. J. Roy. Meteor. Soc.*, **125**, 925–940.

618 Dacre, H. F., and S. L. Gray, 2006: Life-cycle simulations of shallow frontal waves and the  
619 impact of deformation strain. *Quart. J. Roy. Meteor. Soc.*, **132**, 2171–2190. doi: 10.1256/  
620 qj.05.238

621 Dacre, H. F., and S. L. Gray, 2013: Quantifying the climatological relationship between  
622 extratropical cyclone intensity and atmospheric precursors, *Geophys. Res. Lett.*, **40**, 2322-  
623 2327.

624 Danard, M. B., 1964: On the influence of released latent heat on cyclone development. *J.*  
625 *Appl. Meteor.*, **3**, 27-37.

626 De Rooy, W. C., and K. Kok, 2004: A combined physical statistical approach for the  
627 downscaling of model wind speed. *Wea. Forec.* **19**, 485-495.

628 Dee, D. P., and 35 co-authors, 2011: The ERA-Interim reanalysis: configuration and  
629 performance of the data assimilation system. *Quart. J. R. Meteor. Soc.*, **137**, 553-597.

630 Dickinson, M. J., L. F. Bosart, W. E. Bracken, G. J. Hakim, D. M. Schultz, M. A. Bedrick,  
631 and K. R. Tyle, 1997: The March 1993 superstorm cyclogenesis: incipient phase synoptic-  
632 and convective-scale flow interaction and model performance. *Mon. Weather Rev.*, **125**,  
633 3041–3072.

634 Doms G., J. Förstner, E. Heise, H. J. Herzog, M. Raschendorfer, T. Reinhardt, B. Ritter, R.  
635 Schrodin, J. P. Schulz, and G. Vogel, 2007: A description of the nonhydrostatic regional  
636 model LM. Part II: physical parameterization. *Technical report*, Consortium for Small-Scale  
637 Modelling. [Available online at <http://www.cosmo-model.org>].

638 Donat, M. G., T. Pardowitz, G. C. Leckebusch, U. Ulbrich, and O. Burghoff, 2011: High-  
639 resolution refinement of a storm loss model and estimation of return periods of loss-intensive  
640 storms over Germany, *Nat. Hazards Earth Syst. Sci.*, **11**, 2821-2833.

641 Dotzek, N., P. Groenemeijer, B. Feuerstein, and A. M. Holzer, 2009: Overview of ESSL's  
642 severe convective storms research using the European Severe Weather Database ESWD.  
643 *Atmos. Res.* **93**, 575-586.

644 Doyle, J. D., C. Amerault, C. A. Reynolds, and P. A. Reinecke, 2014: Initial condition  
645 sensitivity and predictability of a severe extratropical cyclone using a moist adjoint. *Mon.*  
646 *Wea. Rev.*, **142**, 320–342. doi:10.1175/MWR-D-13-00201.1

647 Dritschel, D. G., P. H. Haynes, M. N. Jukes, and T. G. Shepherd, 1991: The stability of a  
648 two-dimensional vorticity filament under uniform strain. *J. Fluid Mech.*, **230**, 647–665.

649 Durst, C. D., 1960: Wind speeds over short periods of time. *Meteor. Mag.* **89**, 181–186.

650 Fink, A. H., T. Brücher, V. Ermert, A. Krüger, and J. G. Pinto, 2009: The European storm  
651 Kyrill in January 2007: synoptic evolution, meteorological impacts and some considerations  
652 with respect to climate change. *Nat. Hazards Earth Syst. Sci.*, **9**, 405-423.

653 Fink, A. H., S. Pohle, J. G. Pinto, and P. Knippertz, 2012: Diagnosing the influence of  
654 diabatic processes on the explosive deepening of extratropical cyclones. *Geophys. Res. Lett.*,  
655 **39**, L07803, doi:10.1029/2012GL051025.

656 Friederichs, P., M. Goeber, S. Bentzien, A. Lenz, and R. Krampitz, 2009: A probabilistic  
657 analysis of wind gusts using extreme value statistics. *Meteor. Z.* **18**, 615–629.

658 Gall, R., 1976: The effects of released latent heat in growing baroclinic waves. *J. Atmos. Sci.*,  
659 **33**, 1686-1701.

660 Gatzen, C., P. Púčik, and D. Ryva, 2011: Two cold-season derechoes in Europe. *Atmospheric*  
661 *Research.* **100**, 740-748.

662 Goyette, S., O. Brasseur, and M. Beniston, 2003: Application of a new wind gust  
663 parameterisation: multiple scale studies performed with the Canadian regional climate model.  
664 *J. Geophys. Res.* **108** (D13), 4374.

665 Gray, S. L., and H. F. Dacre, 2006: Classifying dynamical forcing mechanisms using a  
666 climatology of extratropical cyclones. *Quart. J. Roy. Meteor. Soc.*, **132**, 1119–1137.

667 Hoskins, B. J., and P. J. Valdes, 1990: On the existence of storm-tracks. *J. Atmos. Sci.*, **47**,  
668 1854 - 1864.

669 Hoskins, B. J. and K. I. Hodges, 2002: New perspectives on the Northern Hemisphere winter  
670 storm tracks. *J. Atmos. Sci.*, **59**, 1041-1061.

671 Johns, R. H., and W. D. Hirt, 1987: Derechos: widespread convectively induced windstorms.  
672 *Wea. Forecasting*. **2**, 32-49.

673 Joos, H., and H. Wernli, 2012: Influence of microphysical processes on the potential vorticity  
674 development in a warm conveyor belt: a case-study with the limited-area model COSMO.  
675 *Quart. J. Roy. Meteor. Soc.*, **138**, 407–418.

676 Ludwig, P., J. G. Pinto, M. Reyers, and S. L. Gray, 2013: The role of anomalous SST over the  
677 southeastern North Atlantic in the explosive development of winter storm Xynthia. *Quart. J.*  
678 *Roy. Meteor. Soc.* doi:10.1002/qj.2253

679 Mailier, P. J., D. B. Stephenson, C. A. T. Ferro, and K. I. Hodges, 2006: Serial clustering of  
680 extratropical cyclones. *Mon. Wea. Rev.*, **134**, 2224–2240.

681 Martin, J. E., 2006: *Mid-Latitude Atmospheric Dynamics – A First Course*. Wiley, 324 pp.

682 Mellor G, and T. Yamada, 1982: Development of a turbulence closure model for geophysical  
683 fluid problems. *Rev. Geophys. Space Phys.* **20**, 851–875.

684 Moore, J. T., and G. E. Vanknowe, 1992: The Effect of Jet-Streak Curvature on Kinematic  
685 Fields. *Mon. Wea. Rev.*, **120**, 2429–2441.

686 Neiman, P. J., M. A. Shapiro, and L. S. Fedor, 1993: The life cycle of an extratropical marine  
687 cyclone. Part II: Mesoscale structure and diagnostics. *Mon. Wea. Rev.*, **121**, 2177–2199.

688 Palmen, E., and C. W. Newton, 1969: *Atmospheric Circulation Systems. Their Structure and*  
689 *Physical Interpretation*. Academic Press, New York, 603 pp.

690 Panofsky, H. A., and J. A. Dutton, 1984: *Atmospheric Turbulence: models and methods for*  
691 *engineering applications*. John Wiley & Sons, New York, 397 pp.

692 Parker, D. J., 1998a: Secondary frontal waves in the North Atlantic region: A dynamical  
693 perspective of current ideas. *Quart. J. Roy. Meteor. Soc.*, **124**, 829–856.

694 Parker, D. J., 1998b: Barotropic instability in frontolytic strain. *Quart. J. Roy. Meteor. Soc.*,  
695 **124**, 1617–1632.

696 Petterssen, S., 1936: Contribution to the theory of frontogenesis. *Geophys. Publ.*, **11**, 1–27.

697 Pinto, J. G., N. Bellenbaum, M. K. Karremann,, and P. M. Della-Marta, 2013: Serial  
698 clustering of extratropical cyclones over the North Atlantic and Europe under recent and  
699 future climate conditions. *J Geophys Res – Atmospheres*, doi:10.1002/jgrd.2013JD020564

700 Renfrew, I. A., A. J. Thorpe, and C. H. Bishop, 1997: The role of the environmental flow in  
701 the development of secondary frontal cyclones. *Quart. J. Roy. Meteor. Soc.*, **123**, 1653–1675.

702 Ritter B, and J. F. Geleyn, 1989: A comprehensive radiation scheme for numerical weather  
703 prediction models with potential applications in climate simulations. *Mon. Weather Rev.* **120**,  
704 303–325.

705 Rivals, H., J. -P. Cammas, and I. A. Renfrew, 1998: Secondary cyclogenesis: The initiation  
706 phase of a frontal wave observed over the eastern Atlantic. *Quart. J. Roy. Meteor. Soc.*,  
707 **124**, 243–267.

708 Rockel, B., A. Will, and A. Hense, (eds.), 2008: Special issue: regional climate modelling  
709 with COSMO-CLM (CCLM). *Meteor. Z.*, **17**, 347–348.

710 Romero, R., M. Gayà, and C. A. Doswell III, 2007: European climatology of severe  
711 convective storm environmental parameters: A test for significant tornado events. *Atmos.*  
712 *Res.*, **83**, 389-404.

713 Rose, S. F., P. V. Hobbs, J. D. Locatelli, and M. T. Stoelinga, 2004: A 10-Yr climatology  
714 relating the locations of reported tornadoes to the quadrants of upper-level jet streaks. *Wea.*  
715 *Forecasting*, **19**, 301–309.

716 Rossa, A. M., H. Wernli, and H. C. Davies, 2000: Growth and decay of an extra-tropical  
717 cyclone's PV-tower. *Meteor. Atmos. Phys.*, **73**, 139–156.

718 Sanders, F., and J. R. Gyakum, 1980: Synoptic-dynamic climatology of the “Bomb”. *Mon.*  
719 *Wea. Rev.*, **108**, 1589–1606.

720 Schrage, J. M., and A. H. Fink, 2012: Nocturnal continental low-level stratus over tropical  
721 West Africa: Observations and possible mechanisms controlling its onset. *Mon. Wea. Rev.*,  
722 **140**, 1794–1809.

723 Schulz, J. -P., 2008: Revision of the turbulent gust diagnostics in the COSMO model.  
724 *COSMO Newslett.* **8**, 17–22. Online at: [www.cosmo-model.org](http://www.cosmo-model.org)

725 Schulz, J. -P., and E. Heise, 2003: A new scheme for diagnosing near-surface convective  
726 gusts. *COSMO Newslett.* **3**, 221–225. Online at: [www.cosmo-model.org](http://www.cosmo-model.org)

727 SwissRe 2008: Natural catastrophes and man-made disasters in 2007: high losses in Europe.  
728 *Sigma*, Nr. 1/2008. *Swiss Re publishing*. Available at [www.swissre.com/sigma/](http://www.swissre.com/sigma/)

729 Thorncroft, C. D., and B. J. Hoskins, 1990: Frontal cyclogenesis. *J. Atmos. Sci.*, **47**, 2317–  
730 2336.

731 Tiedtke, M. 1989: A comprehensive mass flux scheme for cumulus parameterization in large-  
732 scale models. *Mon. Wea. Rev.*, **117**, 1779–1800.

733 Uccellini, L. W., and D. R. Johnson, 1979: The coupling of upper and lower tropospheric jet  
734 streaks and implications for the development of severe convective storms. *Mon. Wea. Rev.*,  
735 **107**, 682–703.

736 Wanner, H., S. Bronnimann, C. Casty, D. Gyalistras, J. Luterbacher, C. Schmutz, D. B.  
737 Stephenson, and E. Xoplaki, 2001: North Atlantic oscillation. Concepts and studies. *Surv.*  
738 *Geophys.*, **22**, 321–382.

739 Wernli, H., S. Dirren, M. A. Liniger, and M. Zillig, 2002: Dynamical aspects of the life cycle  
740 of the winter storm ‘Lothar’ (24–26 December 1999). *Quart. J. Roy. Meteor. Soc.*, **128**, 405–  
741 429.

742 Wieringa, J., 1973: Gust factors over open water and built up country. *Bound. Layer Meteor.*  
743 **3**, 424–441.

744 Young, M.V., G. A. Monk, and K. A. Browning, 1987: Interpretation of satellite imagery of a  
745 rapidly deepening cyclone. *Quart. J. Roy. Meteor. Soc.*, **113**, 1089–1115.

746

747 **Figure caption list**

748 **Figure 1.** Six-hourly cyclone location (a) and core pressure evolution (b) for Kyrill I  
749 (squares) and Kyrill II (diamonds) from ERA-Interim. Data ranges from 16 January 1200  
750 UTC until 19 January 1200 UTC. CCLM domains for simulations with 25 km (domain 1,  
751 black), 7 km (domain 2a and 2b, blue) and 2.8 km (domain 3, black) grid spacing outlined in  
752 (a). Black circles mark points where Kyrill I and II co-occur for the first time.

753 **Figure 2.** Comparison of (a) cyclone tracks and (b) core pressure evolution of CCLM  
754 simulations for Kyrill I and II. Black squares/diamonds: 6-hourly ERA-Interim data for Kyrill  
755 I/Kyrill II. Red: hourly CCLM 25 km grid spacing data for Kyrill I/ Kyrill II (red  
756 squares/diamonds each six hours). Blue: hourly CCLM 7 km grid spacing data for Kyrill I/  
757 Kyrill II (blue squares/diamonds each six hours). All Kyrill I/II tracks in (a) end/start at 18  
758 January 0000 UTC.

759 **Figure 3.** Synoptic-scale overview for 25 km grid spacing simulation of Kyrill I & II at 17  
760 January 1200 UTC ((a), (d), (g)), 18 January 0000 UTC ((b), (e), (h)) and 18 January 1200  
761 UTC ((c), (f), (i)). (a)-(c): jet stream [ $\text{m s}^{-1}$ ] (shaded) and geopotential height (black isolines  
762 each 16gpdm) at 300hPa. (d)-(f): specific humidity [ $\text{g kg}^{-1}$ ] (shaded) and potential vorticity  
763 (isolines at 1.5 and 3.5 PVU) at 500 hPa. (g)-(i): equivalent potential temperature  $\theta_e$  [K]  
764 (shaded) at 850hPa and mean sea-level pressure [hPa] (isolines each 5 hPa). Numbers 1 & 2  
765 mark the corresponding cyclone positions of Kyrill I and II respectively.

766 **Figure 4** Frontal structure and forcing during secondary cyclogenesis for 7 km grid spacing  
767 simulation at 18 January 0000 UTC (left column) and 18 January 0600 UTC (right column).  
768 (a) and (b): horizontal wind [ $\text{m s}^{-1}$ ] speed (contour lines starting at  $40 \text{ m s}^{-1}$ , then each  $10 \text{ m s}^{-1}$   
769 until  $90 \text{ m s}^{-1}$ ) and divergence [ $10^{-5} \text{ s}^{-1}$ ] (shaded) at 300 hPa. (c) and (d): along-front stretching  
770 deformation of the wind field [ $10^{-5} \text{ s}^{-1}$ ] (shaded) at 900 hPa, potential vorticity (stippled area

771 inside bold black line marks regions with  $PV > 2PVU$  between 850 – 950 hPa) and mean sea  
772 level pressure [hPa] (contour lines each 4 hPa). (e) and (f): potential vorticity (as (c), (d)) and  
773 equivalent potential temperature [K] (shaded) at 850 hPa, ageostrophic wind component  
774 (vectors) at 900 hPa and mean sea level pressure (as (c), (d)). (g) and (h): precipitation  
775 amount [ $\text{mm h}^{-1}$ ] for preceding hour, wind barbs for wind speed [ $\text{m s}^{-1}$ ] at 975 hPa (triangle  
776  $22.5 \text{ m s}^{-1}$ , long dash  $5 \text{ m s}^{-1}$ , short dash  $2.5 \text{ m s}^{-1}$ ) and mean sea level pressure (as (c), (d)).  
777 Dotted black lines in (g), (h) denote location of cross sections depicted in Figure 6. Numbers  
778 1 & 2 mark the corresponding cyclone positions of Kyrill I and II respectively. (i) and (j):  
779 surface analysis charts provided by DWD (red border marks section for (a)-(h)).

780 **Figure 5.** West-East and South-North orientated vertical cross sections at (a), (c), (e), (g) 18  
781 January 0000 UTC and (b), (d), (f), (h) 18 January 0600 UTC for 7 km grid spacing  
782 simulation. Positions of cross sections are marked in Figure 4. (a) and (b) West-East cross  
783 sections depicting equivalent potential temperature  $\theta_e$  [K] in thin black lines (each 5 K),  
784 dynamical tropopause marked by 2-PVU line (bold blue line) and regions with diabatic  
785 heating rate [ $\text{K h}^{-1}$ ] (shaded areas). (c) and (d) as for (a) and (b) but for South – North cross  
786 sections. (e) and (f): as (c) and (d) but diabatic heating rate from cumulus parameterization  
787 excluded. Number “2” along the abscissa marks the corresponding cyclone positions of Kyrill  
788 II. (g) and (h) shows total DPVR ( $\text{PVU h}^{-1}$ ) and the z-component of absolute vorticity  $\eta_p$  (blue  
789 line at  $0.5 \times 10^{-4} \text{ s}^{-1}$ ).

790 **Figure 6.** (a): Synopsis of locations when Kyrill I & II co-occur for the first time for CCLM  
791 25 km grid spacing CNTRL and sensitivity experiments with suppressed latent heat release in  
792 convection scheme. (b): pressure progression for Kyrill I. (c): pressure progression for Kyrill  
793 II. Color codes for lines are in (c).

794 **Figure 7.** Frontal forcing, structure and wind gusts for the 7 km grid spacing simulation of  
795 Kyrill II over central Europe at 18 January 1500 UTC, 1800 UTC and 2100 UTC. (a)-(c): jet

796 stream [ $\text{m s}^{-1}$ ] (contour lines each  $10 \text{ m s}^{-1}$  above  $30 \text{ m s}^{-1}$ ) and divergence [ $10^{-5} \text{ s}^{-1}$ ] (shaded)  
797 at 300 hPa. (d)-(f): geopotential height [gpdm] (GPH, isolines each 8gpdm), potential  
798 vorticity [PVU] (PV, shaded) and relative humidity [%] (region less than 10% stippled) at  
799 500 hPa. (g)-(i): mean sea level pressure [hPa] (contour lines each 4 hPa, cyclone center  
800 isobar bold) and precipitation amount of the preceding hour [ $\text{mm h}^{-1}$ ]. Grid points with  
801 convective precipitation are marked with red dots. (j)-(l): same as (g)-(i) but for maximum  
802 wind gust  $v_{\text{DWD}}$  [ $\text{m s}^{-1}$ ]. Grid points with convective gusts exceeding  $25 \text{ m s}^{-1}$  are marked with  
803 black dots.

804 **Figure 8.** Convection-permitting CCLM-simulation (2.8 km grid spacing) of the cold front  
805 over Germany between 18 January 1700 UTC and 1900 UTC. (a)-(c): Simulated radar  
806 reflectivity (shaded, [DBZ]), upward vertical velocity at 850 hPa (bold black line for velocity  
807  $> 0.75 \text{ m s}^{-1}$ ) and relative humidity at 500 hPa (region with relative humidity  $< 30\%$  stippled).  
808 (d)-(f): Maximum  $v_{\text{DWD}}$  wind gust (shaded) and upper-level jet stream (contour lines each 10  
809  $\text{m s}^{-1}$  above  $30 \text{ m s}^{-1}$ ). Inverted triangles in (e) and (f) mark the positions of 3 verified tornado  
810 reports (see text for more details). (g)-(i): hourly-averaged precipitation rate (preceding hour)  
811 [ $\text{mm h}^{-1}$ ] (shaded) and mean sea level pressure [hPa] (isobars each 2 hPa).

812 **Figure 9.** Vertical profiles at  $6.76^\circ\text{E}$  and  $51.28^\circ\text{N}$  at 18 January 1645 UTC. (a) Gradient  
813 Richardson number ( $Ri$ , dimensionless: shaded area (grey) marks the transition between stable  
814 ( $Ri > 1$ ) and turbulent flow ( $Ri < 0.25$ )) and turbulent kinetic energy (TKE, [ $\text{m}^2 \text{ s}^{-2}$ ]). (b)  
815 Vertical velocity ( $\omega$ , [ $\text{m s}^{-1}$ ]) and diabatic heating rate ( $\Delta\text{TLH}$ , [ $\text{K h}^{-1}$ ]). (c) Magnitude of  
816 horizontal wind speed [ $\text{m s}^{-1}$ ]. (d) Potential and equivalent potential temperature of saturated  
817 air ( $\theta$ ,  $\theta_e^*$ , [K]). (e) Areas over Central Germany (including federal state borders; NRW: North  
818 Rhine-Westphalia; B: Berlin) with instantaneous gust wind speed at 1645 UTC exceeding  
819  $32.7 \text{ m s}^{-1}$  marked in red. Equivalent potential temperature ( $\theta_e$ ) along the front region at 950  
820 hPa marked with blue contours (lines between 300 K and 306 K with interval of 2 K) with

821 higher values to the south. Black/white circles mark the locations of vertical profiles. Front  
822 normal cross section depicted in Fig. 11 (a) is marked by bold black line.

823 **Figure 10.** Same as Figure 9 but for 10.50°E and 51.28°N at 18 January 1800 UTC and front  
824 normal cross section depicted in Fig. 11 (b) marked by bold black line.

825 **Figure 11.** Front normal cross sections for (a) 18 January 1645 UTC and (b) 18 January 1800  
826 UTC. Locations of cross sections are marked by the bold black lines in Fig. 9 (e) and 10 (e),  
827 respectively. Depicted are equivalent potential temperature ( $\theta_e$  [K], solid lines), wind vectors  
828 of front normal and vertical wind component (scale shown at the lower right corner, vertical  
829 velocity scaled by factor 10 for better representation) and magnitude of horizontal wind speed  
830 (above dashed line wind speeds exceed 45 m s<sup>-1</sup>). Gradient Richardson numbers ( $Ri$ ) below  
831 0.25 (turbulent flow) are shaded in dark grey. Regions with  $0.25 < Ri < 1$  (transition between  
832 stable and turbulent flow) are shaded in light grey. Bold vertical lines up to 700 hPa at  
833 51.28°N mark the locations of corresponding vertical profiles in Fig. 9 and 10.

834 **Figure 12.** Comparison of simulated (2.8 km grid spacing simulation, shaded areas) and  
835 observed (colored points) 10m-wind gusts (both averaged between 18 January 1200 UTC and  
836 19 January 0600 UTC) for (a)  $v_{DWD}$  and (b) for  $v_{TKE}$ . Federal state borders of Germany  
837 included.

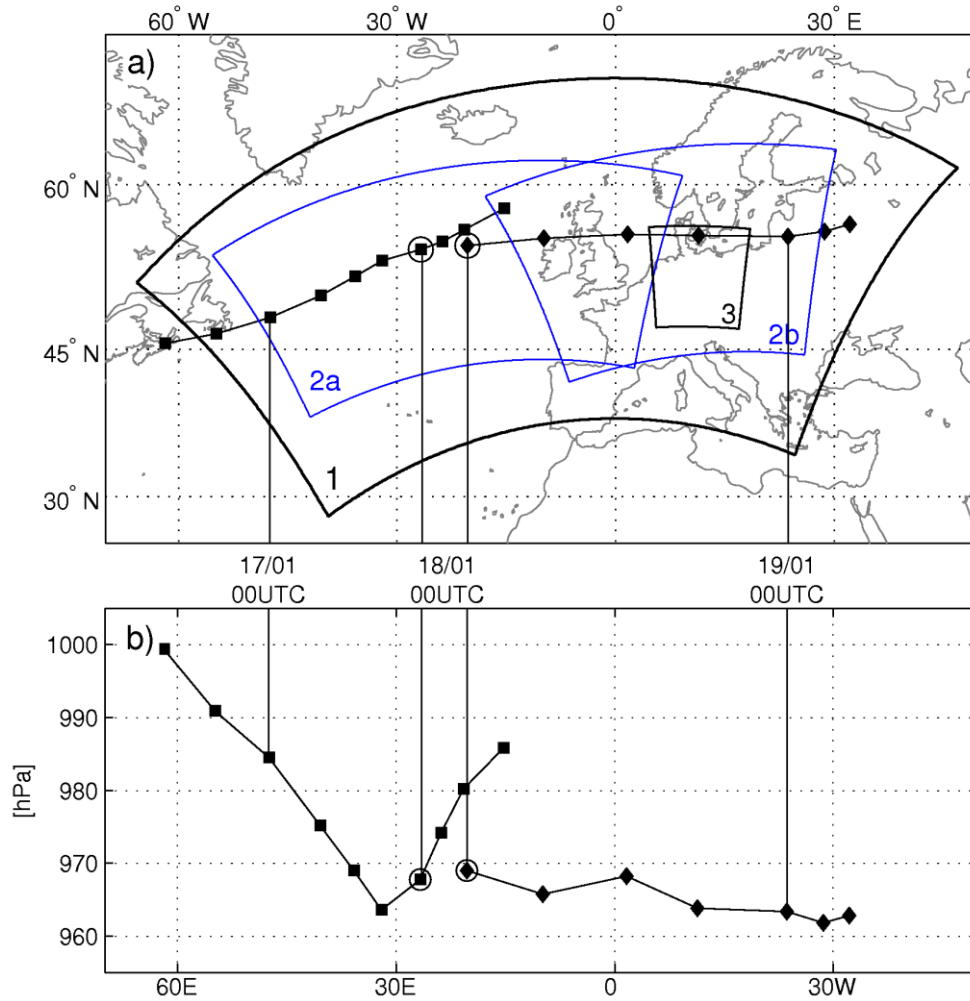


**Figure 1.** Six-hourly cyclone location (a) and core pressure evolution (b) for Kyrill I (squares) and Kyrill II (diamonds) from ERA-Interim. Data ranges from 16 January 1200 UTC until 19 January 1200 UTC. CCLM domains for simulations with 25 km (domain 1, black), 7 km (domain 2a and 2b, blue) and 2.8 km (domain 3, black) grid spacing outlined in (a). Black circles mark points where Kyrill I and II co-occur for the first time.

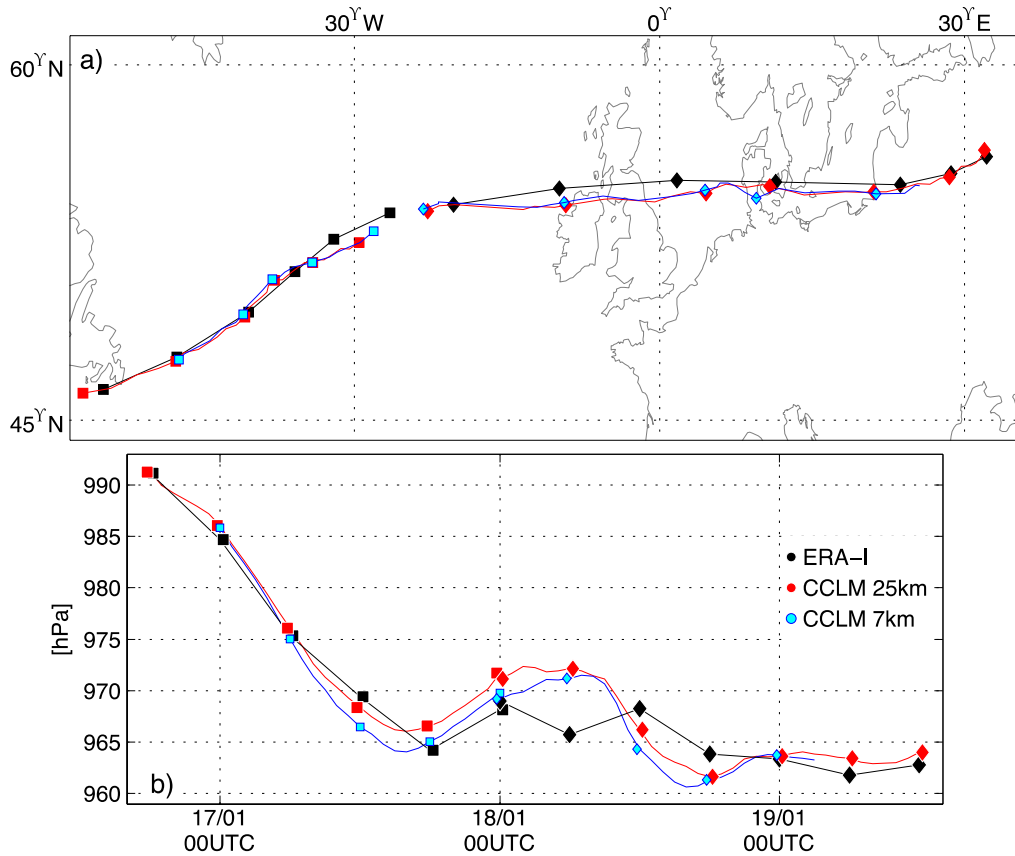
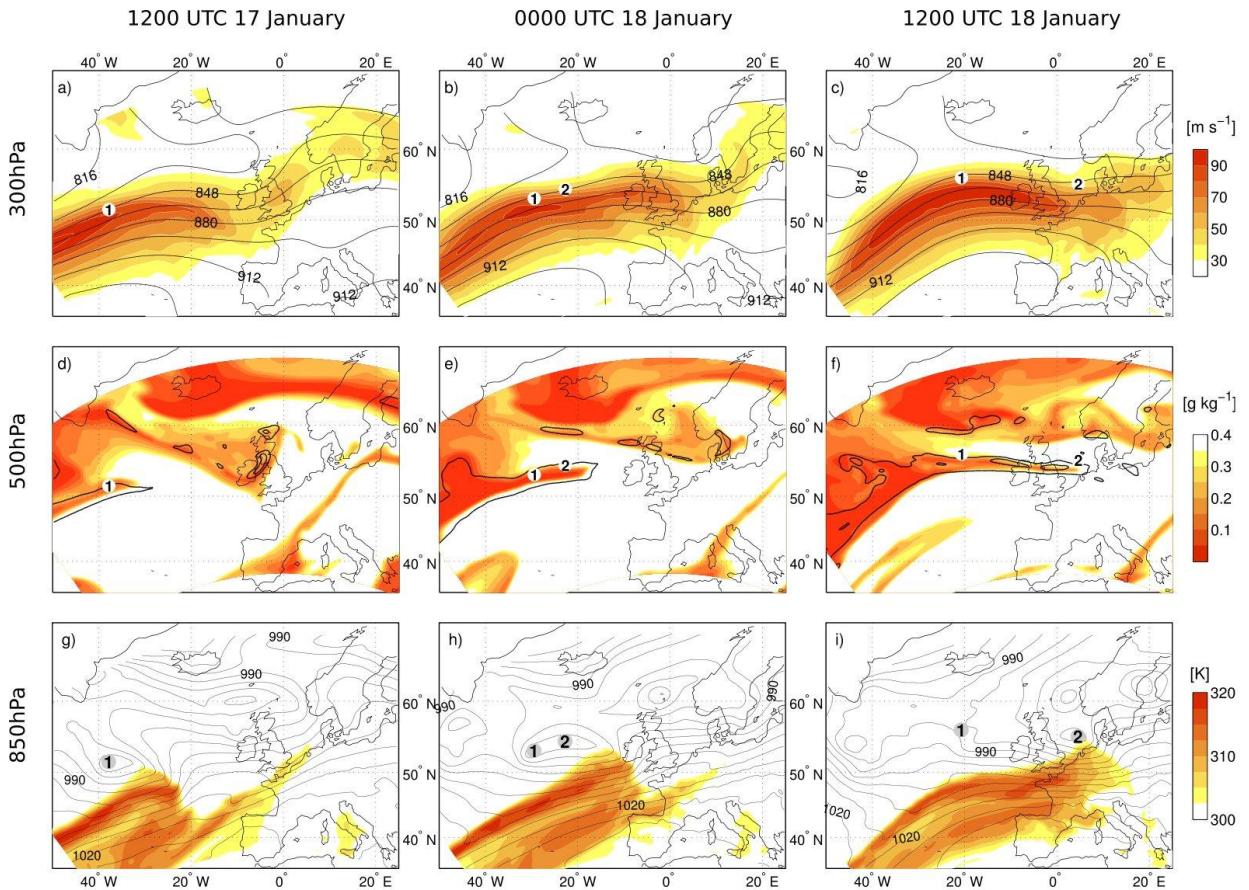
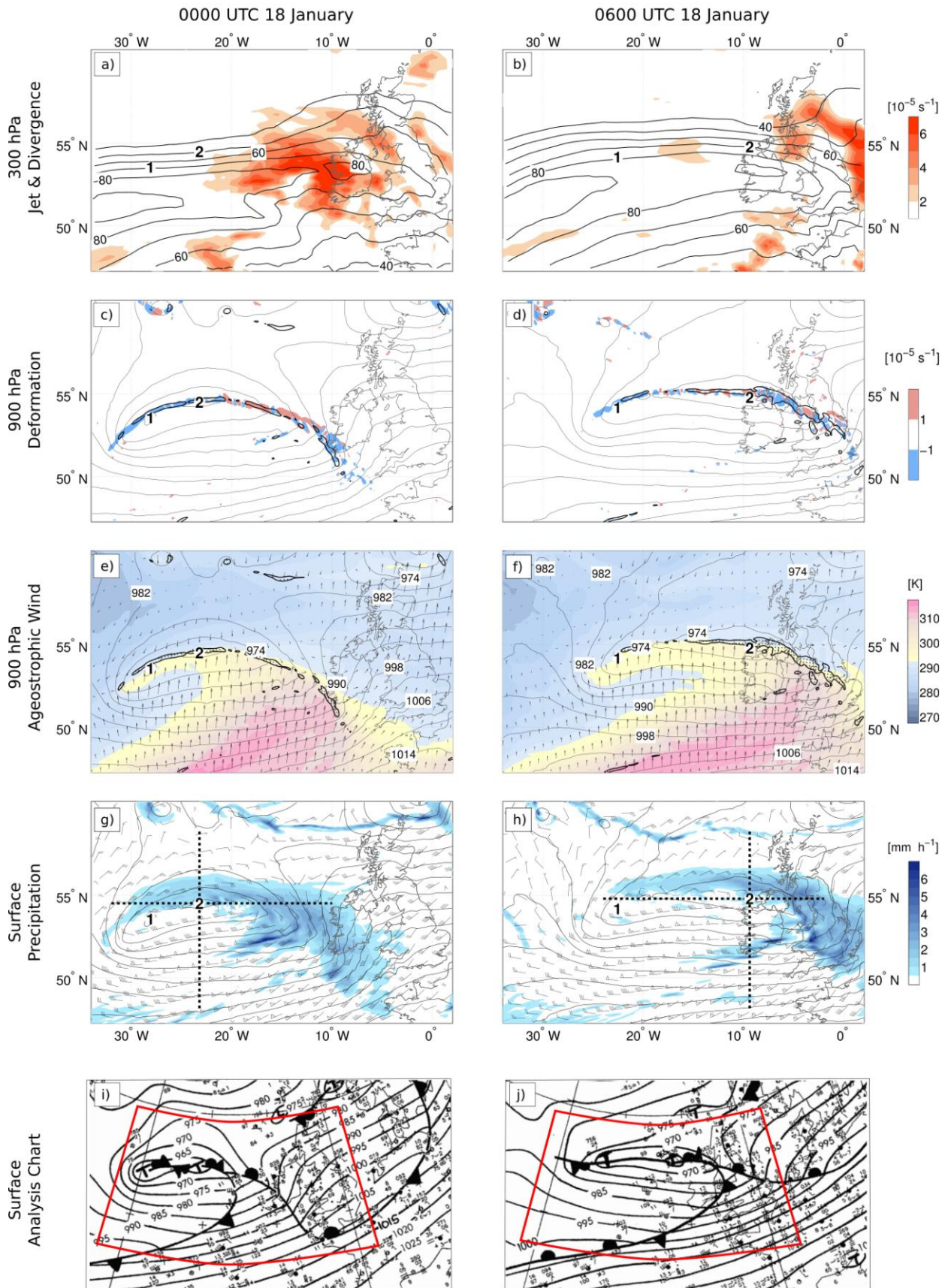


**Figure 2.** Comparison of (a) cyclone tracks and (b) core pressure evolution of CCLM simulations for Kyrill I and II. Black squares/diamonds: 6-hourly ERA-Interim data for Kyrill I/Kyrill II. Red: hourly CCLM 25 km grid spacing data for Kyrill I/ Kyrill II (red squares/diamonds each six hours). Blue: hourly CCLM 7 km grid spacing data for Kyrill I/ Kyrill II (blue squares/diamonds each six hours). All Kyrill I/II tracks in (a) end/start at 18 January 0000 UTC.

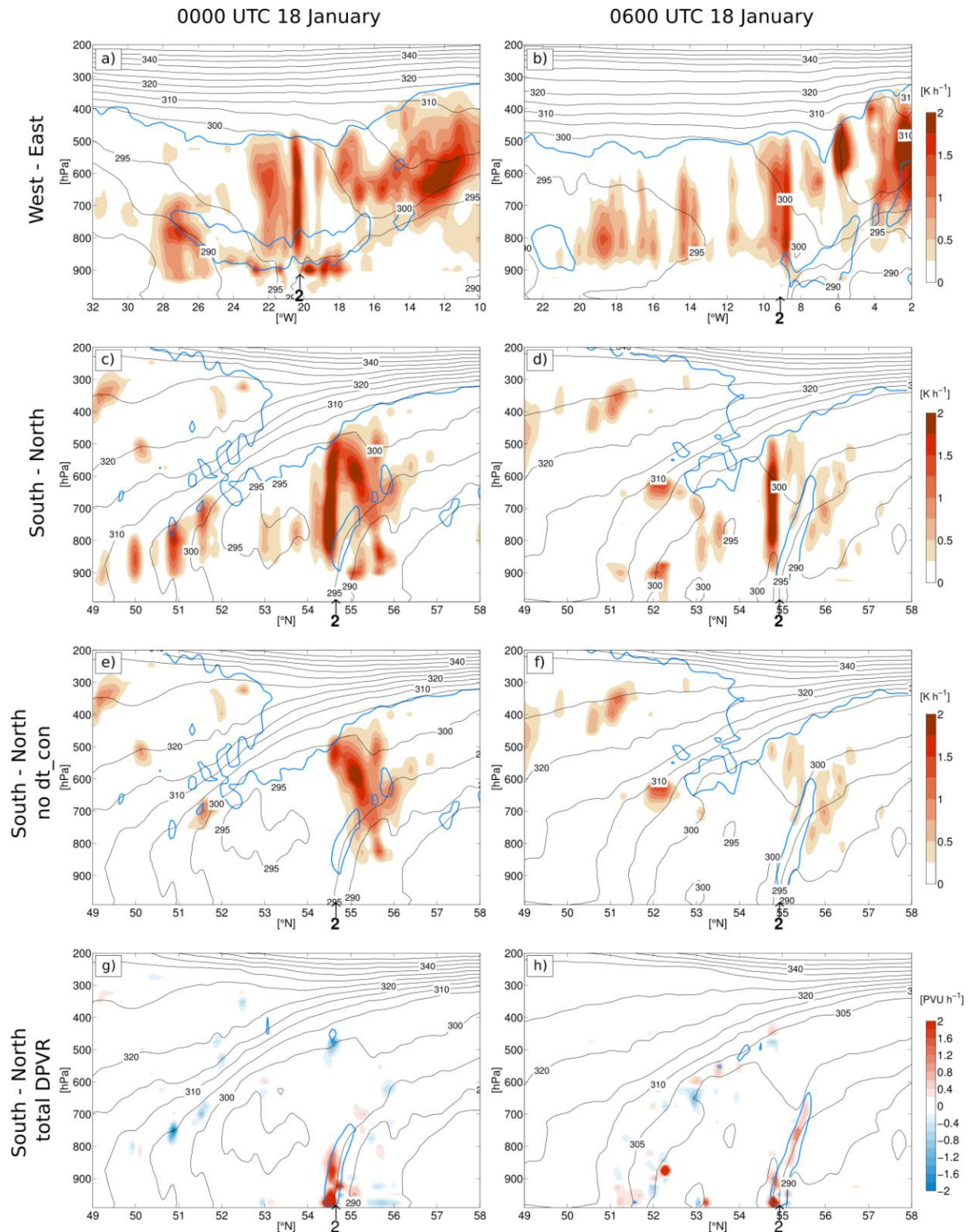


838 **Figure 3.** Synoptic-scale overview for 25 km grid spacing simulation of Kyrill I & II at 17  
839 January 1200 UTC ((a), (d), (g)), 18 January 0000 UTC ((b), (e), (h)) and 18 January 1200  
840 UTC ((c), (f), (i)). (a)-(c): jet stream [ $\text{m s}^{-1}$ ] (shaded) and geopotential height (black isolines  
841 each 16gpdm) at 300hPa. (d)-(f): specific humidity [ $\text{g kg}^{-1}$ ] (shaded) and potential vorticity  
842 (isolines at 1.5 and 3.5 PVU) at 500 hPa. (g)-(i): equivalent potential temperature  $\theta_e$  [K]  
843 (shaded) at 850hPa and mean sea-level pressure [hPa] (isolines each 5 hPa). Numbers 1 & 2  
844 mark the corresponding cyclone positions of Kyrill I and II respectively.  
845



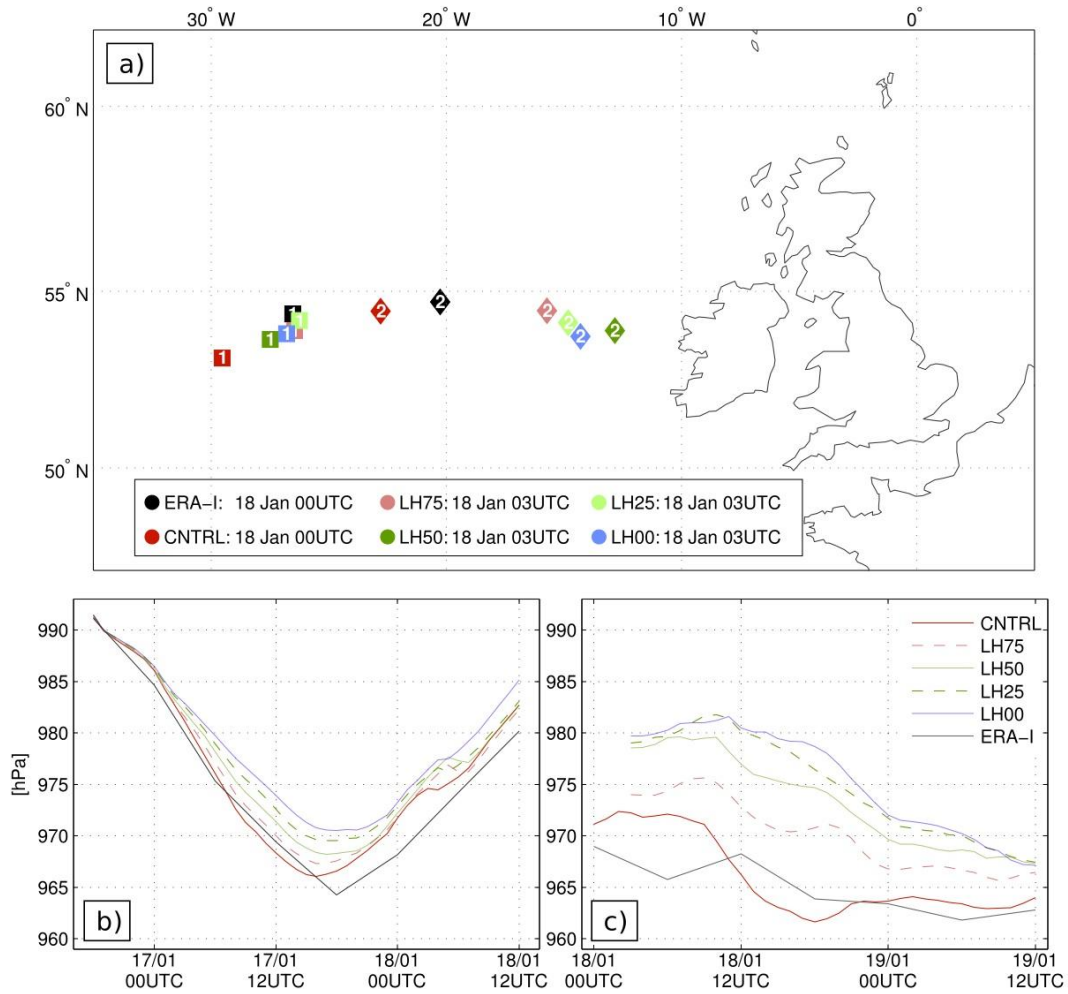
846 **Figure 4** Frontal structure and forcing during secondary cyclogenesis for 7 km grid spacing  
 847 simulation at 18 January 0000 UTC (left column) and 18 January 0600 UTC (right column).  
 848 (a) and (b): horizontal wind [ $\text{m s}^{-1}$ ] speed (contour lines starting at  $40 \text{ m s}^{-1}$ , then each  $10 \text{ m s}^{-1}$

849 until  $90 \text{ m s}^{-1}$ ) and divergence [ $10^{-5} \text{ s}^{-1}$ ] (shaded) at 300 hPa. (c) and (d): along-front stretching  
850 deformation of the wind field [ $10^{-5} \text{ s}^{-1}$ ] (shaded) at 900 hPa, potential vorticity (stippled area  
851 inside bold black line marks regions with  $\text{PV} > 2\text{PVU}$  between 850 – 950 hPa) and mean sea  
852 level pressure [hPa] (contour lines each 4 hPa). (e) and (f): potential vorticity (as (c), (d)) and  
853 equivalent potential temperature [K] (shaded) at 850 hPa, ageostrophic wind component  
854 (vectors) at 900 hPa and mean sea level pressure (as (c), (d)). (g) and (h): precipitation  
855 amount [ $\text{mm h}^{-1}$ ] for preceding hour, wind barbs for wind speed [ $\text{m s}^{-1}$ ] at 975 hPa (triangle  
856  $22.5 \text{ m s}^{-1}$ , long dash  $5 \text{ m s}^{-1}$ , short dash  $2.5 \text{ m s}^{-1}$ ) and mean sea level pressure (as (c), (d)).  
857 Dotted black lines in (g), (h) denote location of cross sections depicted in Figure 6. Numbers  
858 1 & 2 mark the corresponding cyclone positions of Kyrill I and II respectively. (i) and (j):  
859 surface analysis charts provided by DWD (red border marks section for (a)-(h)).

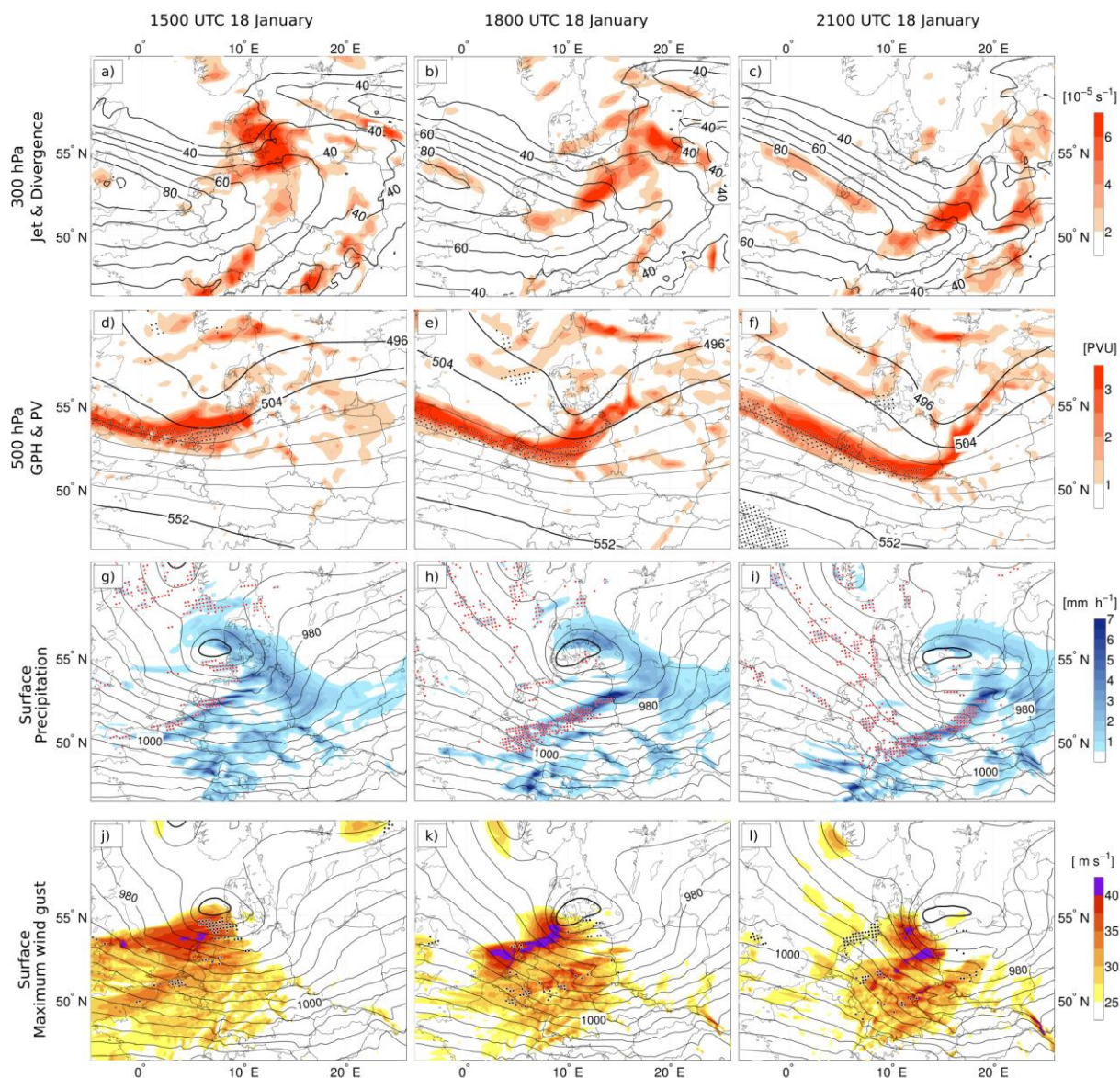


860 **Figure 5.** West-East and South-North orientated vertical cross sections at (a), (c), (e), (g) 18  
 861 January 0000 UTC and (b), (d), (f), (h) 18 January 0600 UTC for 7 km grid spacing  
 862 simulation. Positions of cross sections are marked in Figure 4. (a) and (b) West-East cross  
 863 sections depicting equivalent potential temperature  $\theta_e$  [K] in thin black lines (each 5 K),  
 864 dynamical tropopause marked by 2-PVU line (bold blue line) and regions with diabatic  
 865 heating rate [ $\text{K h}^{-1}$ ] (shaded areas). (c) and (d) as for (a) and (b) but for South – North  
 866 sections. (e) and (f): as (c) and (d) but diabatic heating rate from cumulus parameterization

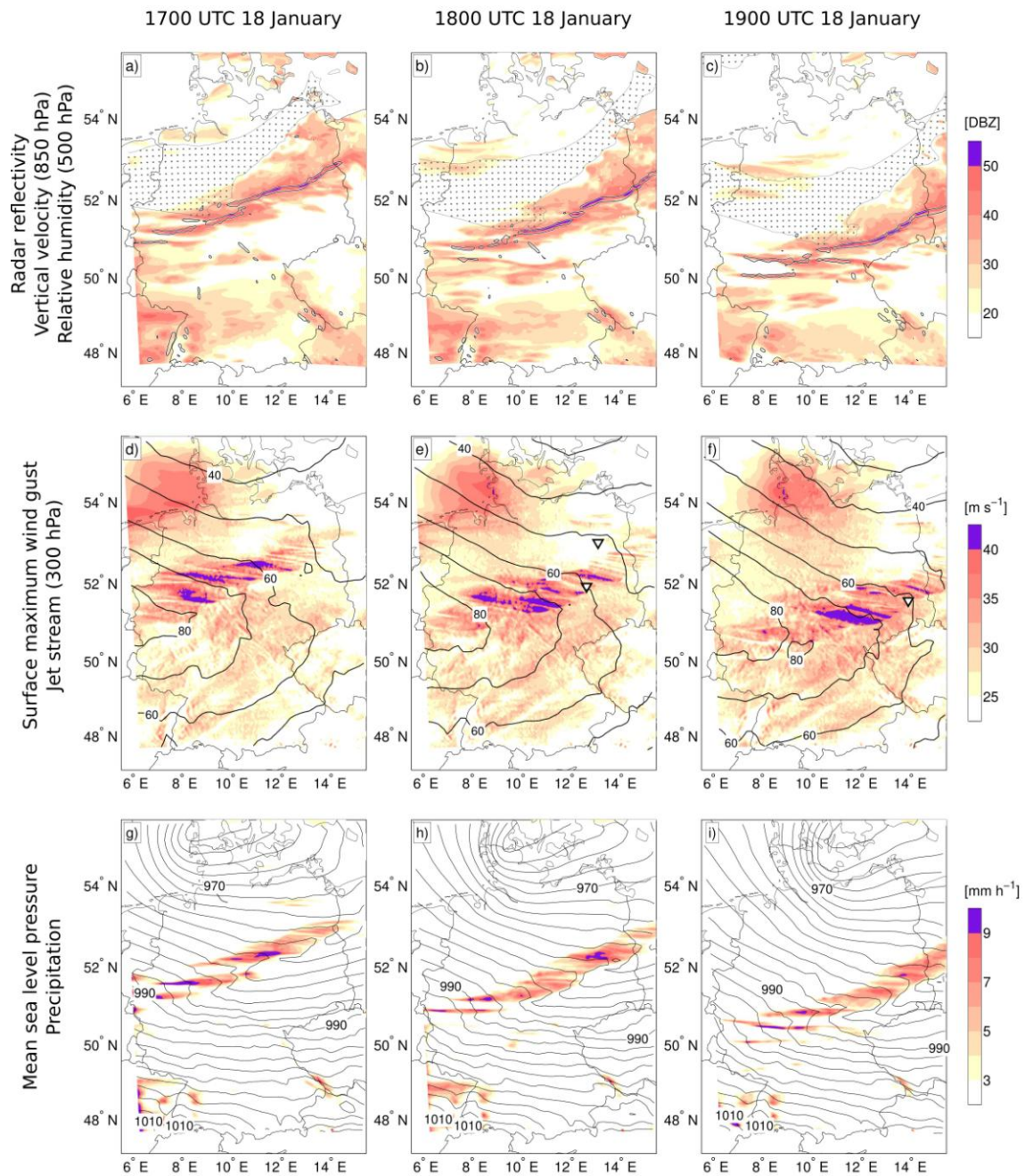
867 excluded. Number “2” along the abscissa marks the corresponding cyclone positions of Kyrill  
868 II. (g) and (h) shows total DPVR ( $\text{PVU h}^{-1}$ ) and the z-component of absolute vorticity  $\eta_p$  (blue  
869 line at  $0.5 \times 10^{-4} \text{ s}^{-1}$ ).  
870



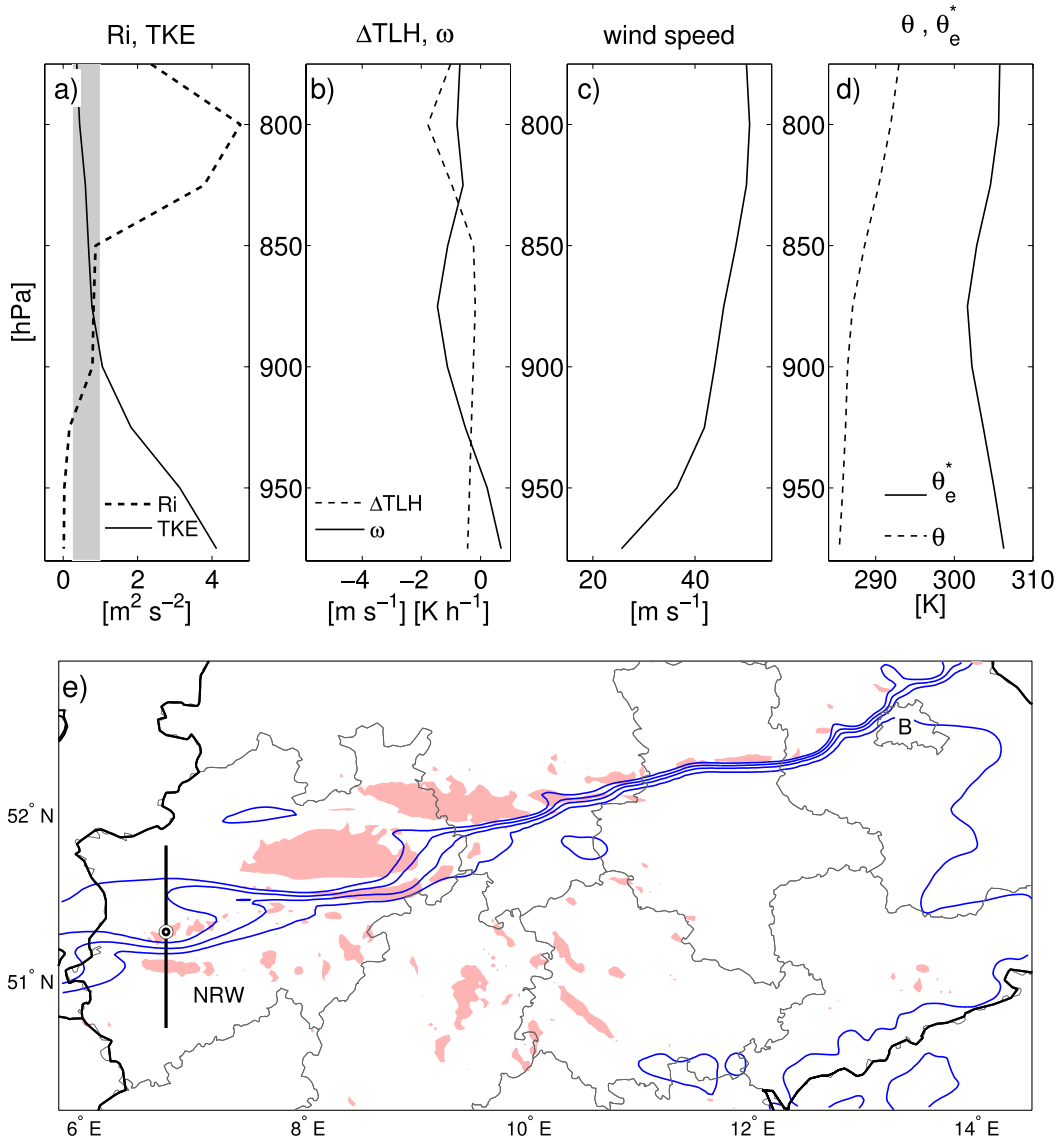
871 **Figure 6.** (a): Synopsis of locations when Kyrill I & II co-occur for the first time for CCLM  
 872 25 km grid spacing CNTRL and sensitivity experiments with suppressed latent heat release in  
 873 convection scheme. (b): pressure progression for Kyrill I. (c): pressure progression for Kyrill  
 874 II. Color codes for lines are in (c).



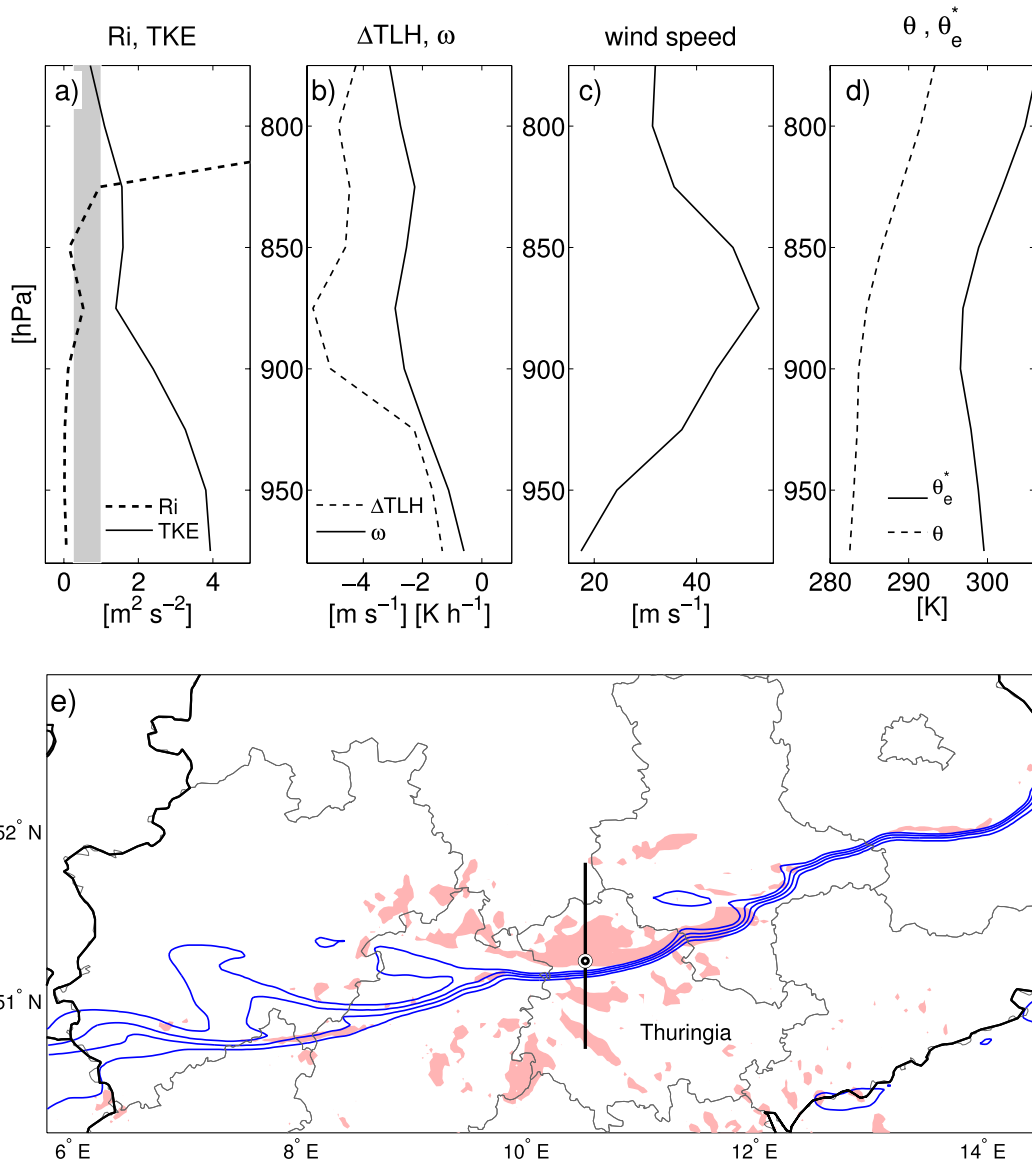
875 **Figure 7.** Frontal forcing, structure and wind gusts for the 7 km grid spacing simulation of  
876 Kyrill II over central Europe at 18 January 1500 UTC, 1800 UTC and 2100 UTC. (a)-(c): jet  
877 stream [ $\text{m s}^{-1}$ ] (contour lines each  $10 \text{ m s}^{-1}$  above  $30 \text{ m s}^{-1}$ ) and divergence [ $10^{-5} \text{ s}^{-1}$ ] (shaded)  
878 at 300 hPa. (d)-(f): geopotential height [gpm] (GPH, isolines each 8gpm), potential  
879 vorticity [PVU] (PV, shaded) and relative humidity [%] (region less than 10% stippled) at  
880 500 hPa. (g)-(i): mean sea level pressure [hPa] (contour lines each 4 hPa, cyclone center  
881 isobar bold) and precipitation amount of the preceding hour [ $\text{mm h}^{-1}$ ]. Grid points with  
882 convective precipitation are marked with red dots. (j)-(l): same as (g)-(i) but for maximum  
883 wind gust  $v_{\text{DWD}}$  [ $\text{m s}^{-1}$ ]. Grid points with convective gusts exceeding  $25 \text{ m s}^{-1}$  are marked with  
884 black dots.  
885



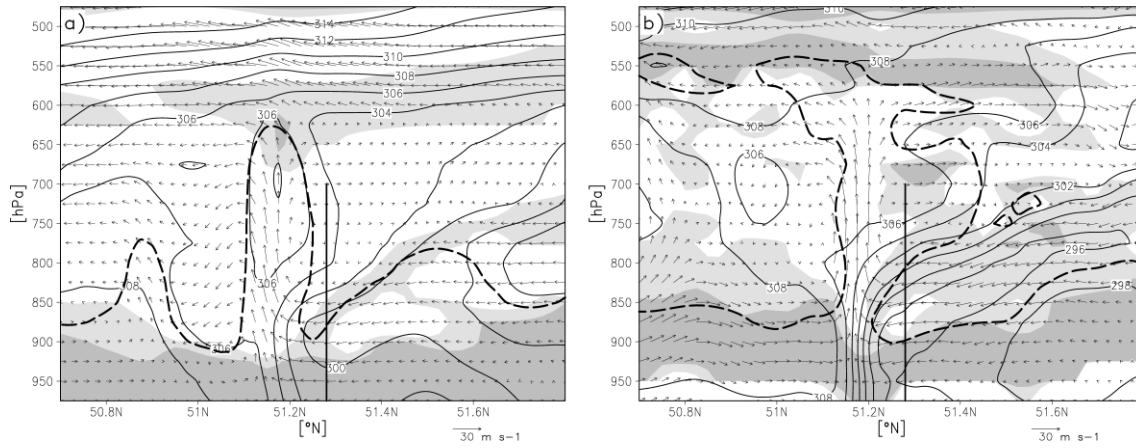
886 **Figure 8.** Convection-permitting CCLM-simulation (2.8 km grid spacing) of the cold front  
 887 over Germany between 18 January 1700 UTC and 1900 UTC. (a)-(c): Simulated radar  
 888 reflectivity (shaded, [DBZ]), upward vertical velocity at 850 hPa (bold black line for velocity  
 889  $> 0.75 \text{ m s}^{-1}$ ) and relative humidity at 500 hPa (region with relative humidity  $< 30\%$  stippled).  
 890 (d)-(f): Maximum  $v_{\text{DWD}}$  wind gust (shaded) and upper-level jet stream (contour lines each 10  
 891  $\text{m s}^{-1}$  above  $30 \text{ m s}^{-1}$ ). Inverted triangles in (e) and (f) mark the positions of 3 verified tornado  
 892 reports (see text for more details). (g)-(i): hourly-averaged precipitation rate (preceding hour)  
 893  $[\text{mm h}^{-1}]$  (shaded) and mean sea level pressure [hPa] (isobars each 2 hPa).



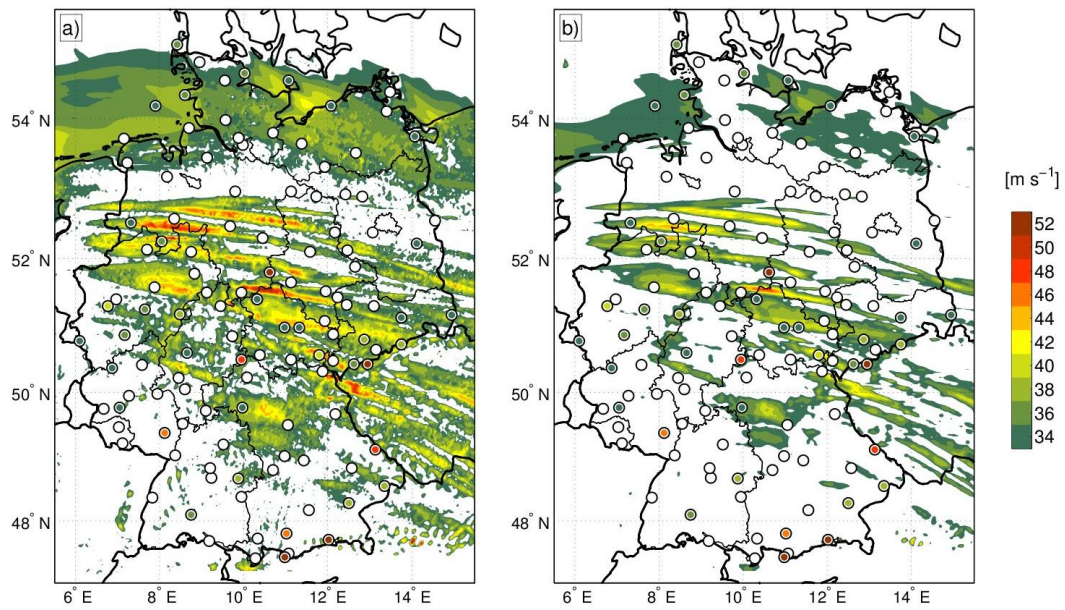
894 **Figure 9.** Vertical profiles at  $6.76^{\circ}\text{E}$  and  $51.28^{\circ}\text{N}$  at 18 January 1645 UTC. (a) Gradient  
 895 Richardson number ( $Ri$ , dimensionless: shaded area (grey) marks the transition between stable  
 896 ( $Ri > 1$ ) and turbulent flow ( $Ri < 0.25$ )) and turbulent kinetic energy (TKE,  $[\text{m}^2 \text{s}^{-2}]$ ). (b)  
 897 Vertical velocity ( $\omega$ ,  $[\text{m s}^{-1}]$ ) and diabatic heating rate ( $\Delta\text{TLH}$ ,  $[\text{K h}^{-1}]$ ). (c) Magnitude of  
 898 horizontal wind speed  $[\text{m s}^{-1}]$ . (d) Potential and equivalent potential temperature of saturated  
 899 air ( $\theta$ ,  $\theta_e^*$ ,  $[\text{K}]$ ). (e) Areas over Central Germany (including federal state borders; NRW: North  
 900 Rhine-Westphalia; B: Berlin) with instantaneous gust wind speed at 1645 UTC exceeding  
 901  $32.7 \text{ m s}^{-1}$  marked in red. Equivalent potential temperature ( $\theta_e$ ) along the front region at 950  
 902 hPa marked with blue contours (lines between 300 K and 306 K with interval of 2 K) with  
 903 higher values to the south. Black/white circles mark the locations of vertical profiles. Front  
 904 normal cross section depicted in Fig. 11 (a) is marked by bold black line.



905 **Figure 10.** Same as Figure 9 but for 10.50°E and 51.28°N at 18 January 1800 UTC and front  
 906 normal cross section depicted in Fig. 11 (b) marked by bold black line.



907 **Figure 11.** Front normal cross sections for (a) 18 January 1645 UTC and (b) 18 January 1800  
 908 UTC. Locations of cross sections are marked by the bold black lines in Fig. 9 (e) and 10 (e),  
 909 respectively. Depicted are equivalent potential temperature ( $\theta_e$  [K], solid lines), wind vectors  
 910 of front normal and vertical wind component (scale shown at the lower right corner, vertical  
 911 velocity scaled by factor 10 for better representation) and magnitude of horizontal wind speed  
 912 (above dashed line wind speeds exceed 45 m s<sup>-1</sup>). Gradient Richardson numbers ( $Ri$ ) below  
 913 0.25 (turbulent flow) are shaded in dark grey. Regions with  $0.25 < Ri < 1$  (transition between  
 914 stable and turbulent flow) are shaded in light grey. Bold vertical lines up to 700 hPa at  
 915 51.28°N mark the locations of corresponding vertical profiles in Fig. 9 and 10.  
 916



917 **Figure 12.** Comparison of simulated (2.8 km grid spacing simulation, shaded areas) and  
 918 observed (colored points) 10m-wind gusts (both averaged between 18 January 1200 UTC and  
 919 19 January 0600 UTC) for (a)  $v_{\text{DWD}}$  and (b) for  $v_{\text{TKE}}$ . Federal state borders of Germany  
 920 included.



## 5. Case study of winter storm Xynthia (February 2010)

Journal article (published):

LUDWIG, P., J. G. PINTO, M. REYERS, AND S. L. GRAY, 2014; The role of anomalous SST and surface fluxes over the southeastern North Atlantic in the explosive development of windstorm Xynthia. *Q. J. R. Meteorol. Soc.* **140**, 1729–1741. doi: 10.1002/qj.2253

Permission to reprint:

The permission to reuse the following material in this thesis has been given by a License Agreement between the corresponding author and John Wiley and Sons provided by Copyright Clearance Center.

*License Number:* 3335791303117

*License date:* Feb 25, 2014

*Licensed content publisher:* John Wiley and Sons

*Licensed content publication:* Quarterly Journal of Royal Meteorological Society

*Licensed content title:* The role of anomalous SST and surface fluxes over the southeastern North Atlantic in the explosive development of windstorm Xynthia

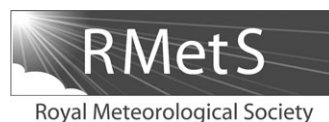
*Licensed copyright line:* ©2013 Royal Meteorological Society

*Licensed content author:* Patrick Ludwig, Joaquim G. Pinto, Mark Reyers, Suzanne L. Gray

*Licensed content date:* Nov 12, 2013

Original page numbers of the manuscript are used.





# The role of anomalous SST and surface fluxes over the southeastern North Atlantic in the explosive development of windstorm Xynthia

Patrick Ludwig,<sup>a\*</sup> Joaquim G. Pinto,<sup>a,b</sup> Mark Reyers<sup>a</sup> and Suzanne L. Gray<sup>b</sup>

<sup>a</sup>*Institute for Geophysics and Meteorology, University of Cologne, Germany*

<sup>b</sup>*Department of Meteorology, University of Reading, UK*

\*Correspondence to: Patrick Ludwig, Institute for Geophysics and Meteorology, University of Cologne, Kerpener Str. 13, 50937 Cologne, Germany. E-mail: pludwig@meteo.uni-koeln.de

In late February 2010 the extraordinary windstorm Xynthia crossed over southwestern and central Europe and caused severe damage, affecting particularly the Spanish and French Atlantic coasts. The storm was embedded in uncommon large-scale atmospheric and boundary conditions prior to and during its development, namely enhanced sea-surface temperatures (SST) within the low-level entrainment zone of air masses, an unusual southerly position of the polar jet stream, and a remarkable split jet structure in the upper troposphere. To analyse the processes that led to the rapid intensification of this exceptional storm originating close to the subtropics (30°N), the sensitivity of the cyclone intensification to latent heat release is determined using the regional climate model COSMO-CLM forced with European Centre for Medium-range Weather Forecasts Reanalysis (ERA)-Interim data. A control simulation with observed SST shows that moist and warm air masses originating from the subtropical North Atlantic were involved in the cyclogenesis process and led to the formation of a vertical tower with high values of potential vorticity (PV). Sensitivity studies with reduced SST or increased laminar boundary roughness for heat led to reduced surface latent heat fluxes. This induced both a weaker and partly retarded development of the cyclone and a weakening of the PV tower, together with reduced diabatic heating rates, particularly at lower and mid-levels. We infer that diabatic processes played a crucial role during the phase of rapid deepening of Xynthia and thus to its intensity over the southeastern North Atlantic. We suggest that windstorms such as Xynthia may occur more frequently under future climate conditions due to the warming SSTs and potentially enhanced latent-heat release, thus increasing the windstorm risk for southwestern Europe.

*Key Words:* extratropical cyclone; windstorm; potential vorticity; diabatic processes; COSMO-CLM

*Received 3 June 2013; Revised 6 September 2013; Accepted 12 September 2013; Published online in Wiley Online Library 12 November 2013*

## 1. Introduction

Mid-latitude winter storms are frequent phenomena that occasionally lead to severe damage and strong socio-economic impacts over Europe (e.g. Lamb, 1991; SwissRe, 2008). The majority of such extreme extratropical cyclones originate in a region between Newfoundland and Iceland and have a northeastward orientated track. This area is also known as the North Atlantic storm-track region (e.g. Hoskins and Valdes, 1990). Most of these extreme cyclones undergo explosive cyclogenesis over the North Atlantic basin before they hit Europe (e.g. windstorms Lothar and Martin in 1999, Jeanett in 2002, Kyrill in 2007, and Klaus in 2009; see Wernli *et al.*, 2002; Liberato *et al.*, 2011; Fink *et al.*, 2012)<sup>1</sup>.

In late February and the first days of March 2010 windstorm Xynthia affected southwestern and central Europe. This explosively deepening storm exhibited an uncommon track compared with typical extreme cyclones (see Trigo, 2006; Pinto *et al.*, 2009). Xynthia originated from the subtropical eastern North Atlantic around 30°N where there were anomalously high sea-surface temperatures (SSTs) even for this subtropical region, and followed an unusual southwest to northeast track passing close to the coast of the Iberian Peninsula (Figure 1(a)).

Severe winds were reported over large parts of southwestern Europe (Liberato *et al.*, 2013; their Figure 2). The windstorm reached a minimum measured core pressure of 969 hPa (according to European Centre for Medium-range Weather Forecasts Reanalysis (ERA)-Interim re-analysis data), and gales reached up to 200 km h<sup>-1</sup> in exposed mountainous areas (Bedacht and Hofherr, 2011). A total of 47 fatalities were reported because of the storm surge and associated dyke bursts that caused 50 000 ha of flooded land when the storm reached the French

<sup>1</sup>Storm names used herein are as given by the Freie Universität Berlin and as used by the German Weather Service. Source: <http://www.met.fu-berlin.de/adopt-a-vortex/historie/>

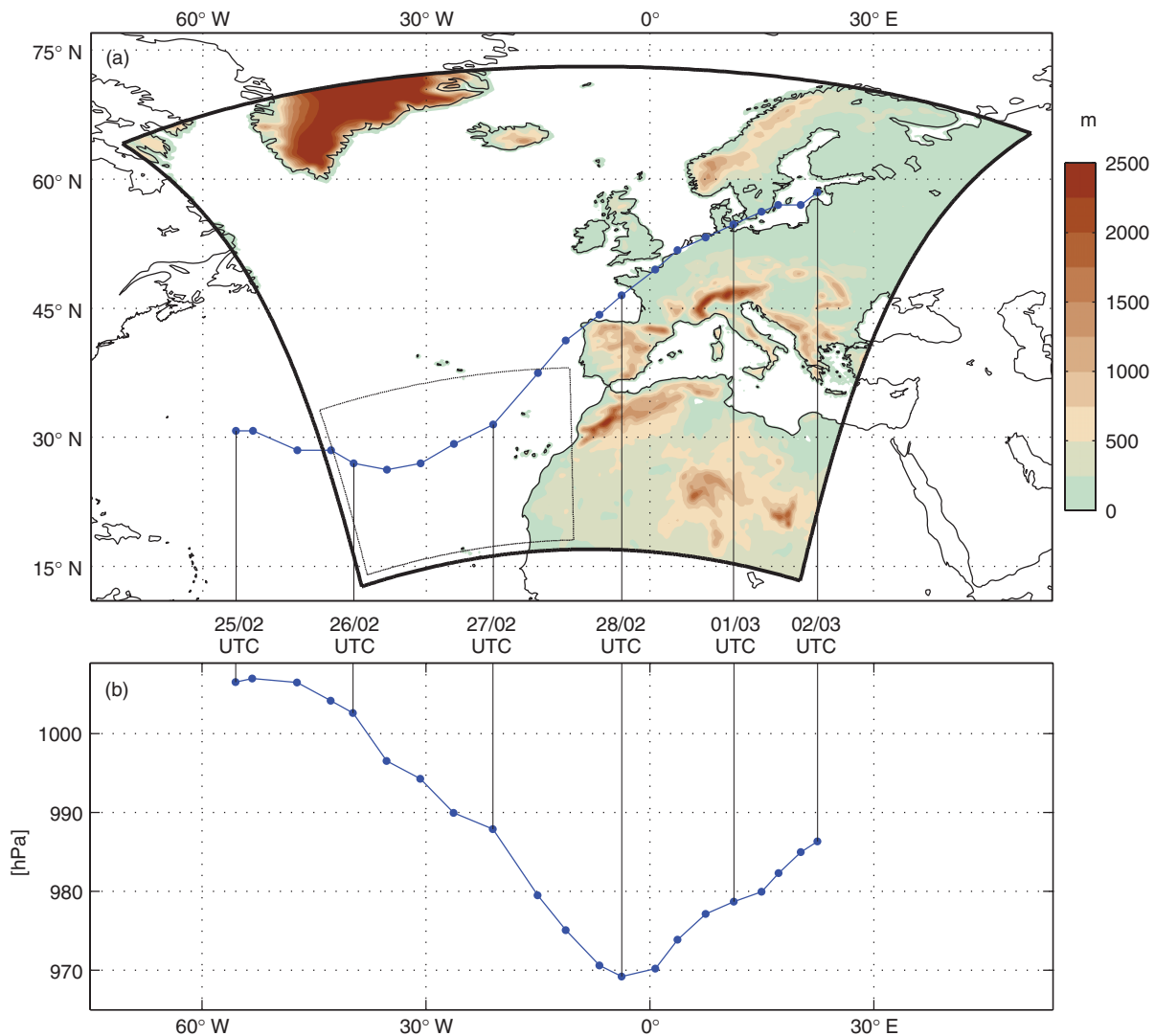


**Figure 1.** (a) Six-hourly cyclone location and (b) core-pressure evolution for Xynthia derived from ERA-Interim data. Data ranges from 25 February 0000 UTC until 2 March 0000 UTC. (a) The CCLM model domain is marked by the black border. The model orography is shaded (m). The small box at the southwestern corner of the model domain delimits the region where SST is perturbed for sensitivity studies. This figure is available in colour online at [wileyonlinelibrary.com/journal/qj](http://wileyonlinelibrary.com/journal/qj)

coast (Lumbroso and Vinet, 2011). Losses for France, Spain and Germany were estimated at €3.10 billion, €250 million and €750 million, respectively (Bedacht and Hofherr, 2011). A detailed description of the socio-economic impacts can be found in Liberato *et al.* (2013).

Many factors associated with the development of extratropical cyclones have been explored in the literature. Primarily, a broad baroclinic environment is required (e.g. Hoskins and Hodges, 2002; Wernli *et al.*, 2002; Gray and Dacre, 2006). As a result of thermal wind balance, strong baroclinicity is associated with a strong upper-tropospheric jet stream (Carlson, 1991). Uccellini and Johnson (1979) showed that upper-level divergence at the entrance and exit region of a jet streak is an important factor for rapid cyclogenesis. Baehr *et al.* (1999) demonstrated that the phase of rapid deepening corresponds to the crossing of the cyclone from the warm to the cold side of the jet stream and its prevailing divergence areas.

Diabatic processes such as the release of latent heat are also important for the evolution of extratropical storms (Uccellini, 1990). Previous studies have demonstrated that latent heat release by cloud condensation processes can be a crucial energy source for the storm evolution (Danard, 1964; Chang *et al.*, 1982; Robertson and Smith, 1983). By applying a novel version of the surface-pressure-tendency equation to re-analysis data, Fink *et al.* (2012) were able to quantify the role of diabatic processes for five recent windstorms. For Xynthia and two other storms diabatic processes were found to contribute more to the observed core pressure fall than horizontal temperature advection. Latent heating has

often been identified to increase the growth rate of cyclones by baroclinic instability (e.g. Davis and Emanuel, 1991), and in some cases it even dominates the cyclogenesis process. Plant *et al.* (2003) and Ahmadi-Givi *et al.* (2004) showed that mid-level latent heating was crucial for two so-called 'type C' cyclones as defined by Deveson *et al.* (2002). In these cases, the latent heating acts as a 'dynamical surrogate' (Snyder and Lindzen, 1991) for the basic-state baroclinicity, enabling cyclones to develop in regions of weak surface thermal anomalies. This is consistent with the higher proportion of type C cyclones found in the east compared with the west North Atlantic (Dacre and Gray, 2009). The location and orientation of the tracks of extreme extratropical cyclones over the North Atlantic basin are strongly linked to the mode of the North Atlantic oscillation (NAO; e.g. Wanner *et al.*, 2001). The probability of the development of extreme cyclones over the North Atlantic is highest during positive NAO phases (e.g. Raible, 2007; Pinto *et al.*, 2009). Nevertheless, extreme cyclones may also occur during negative NAO phases. In such a negative NAO phase, the polar jet stream is shifted southwards (e.g. Woollings *et al.*, 2010), thus enhancing the probability for severe windstorms affecting southwestern Europe.

Many studies have pointed out the benefit of using potential vorticity (PV; Hoskins *et al.*, 1985) to analyse the temporal evolution of synoptic systems. Broad areas of high PV values in the upper troposphere (meridionally orientated PV streamers) have been identified as precursors for cyclonic systems (Massacand *et al.*, 1998, 2001). Potential vorticity anomalies are also strongly

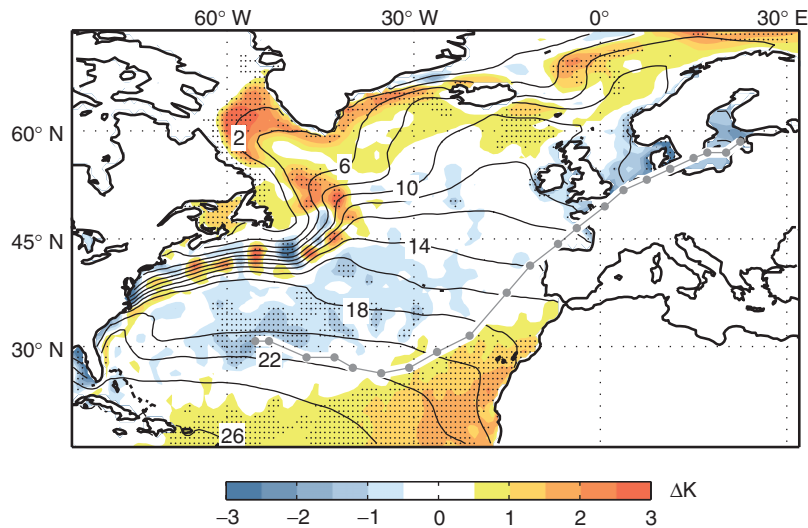


**Figure 2.** Long-term average of SST over the North Atlantic basin for February (1980–2009) from ERA-Interim data (isolines with an interval of 2 °C) and SST anomalies for February 2010 (shaded). Areas with an anomaly more/less than twice the standard deviation are indicated with black dots. Cyclone track is included in grey.

linked to diabatic processes, and anomalously high low-level and mid-level PV values often act as an indicator of latent heat release (cf. Hoskins, 1990; Wernli *et al.*, 2002). The interactions between upper-level PV anomalies and diabatically induced low-level PV anomalies can lead to an intensification of the cyclogenesis process (Hoskins *et al.*, 1985) and to the formation of a so-called PV tower with a distinct vertical extension throughout the troposphere (Wernli *et al.*, 2002). Hence, the generation of PV in the low and mid-troposphere also plays an important role in cyclone formation (e.g. Reed *et al.*, 1992; Wernli and Davies, 1997), and the vertical PV distribution can be used to analyse the associated diabatic processes. Areas of extensive diabatic heating can be found, e.g. in warm conveyor belts of extratropical cyclones, where the ascent of warm and moist air masses leads to huge amounts of latent heat release and the formation of upper-tropospheric negative PV anomalies in addition to the positive PV anomalies at lower levels (Pomroy and Thorpe, 2000). The influence of latent heat release on PV changes in warm conveyor belts and its potential influence on the large-scale dynamics is currently a subject of intense research (e.g. Chagnon *et al.*, 2013; Joos and Wernli, 2012). Further, Dacre and Gray (2013) analysed the relationship between atmospheric precursors and extratropical cyclone intensity. For cyclones over the eastern North Atlantic they detected a significant association between the existence of mid-tropospheric PV anomalies and increased cyclone intensity 48 h later.

As countries in southern Europe are rarely affected by severe windstorms, we analyse here the large-scale dynamical conditions supporting the unusual southerly origin and rapid intensification of Xynthia. Regional (rather than global) model studies are required to consider the associated diabatic processes, because the feedback between cyclone intensification and latent heat release is strongly sensitive to horizontal resolution (Willison *et al.*, 2013). The aim of this study is to determine the role of anomalously high SST over the southeastern North Atlantic in the cyclogenesis process of Xynthia by using a regional climate model. Section 2 describes the data and the regional climate model used in this study. A short description of different numerical sensitivity experiments is also given. In section 3 a brief synoptic overview of the large-scale atmospheric conditions prior to and during the occurrence of Xynthia, as well as results of a Lagrangian trajectory analysis, are shown. The analysis of the outcomes of the regional numerical simulations is presented in section 4. The general findings are discussed and summarized in section 5.

## 2. Data, analysis tools and numerical model

ERA-Interim re-analysis data (Dee *et al.*, 2011) from the European Centre for Medium-range Weather Forecasts (ECMWF) are used to analyse the large-scale atmospheric conditions prior to and during the occurrence of Xynthia. These data are available at six-hourly intervals with a horizontal resolution of  $0.75^\circ \times 0.75^\circ$ . To identify the sources of air masses involved in the cyclogenesis process a Lagrangian trajectory analysis tool (Noone and Simmonds, 1999; Barras and Simmonds, 2009) is applied to several variables in the ERA-Interim dataset.

The non-hydrostatic regional COSMO model (<http://www.cosmo-model.org>) is used for model studies, specifically the Climate Limited-area Model Version 4.8 (COSMO-4.8-CLM, hereafter CCLM; Rockel *et al.*, 2008). The formulation of the dynamical core and physical parametrizations is equal to those of the COSMO-model, which is operationally used by the German Weather Service (DWD). The only difference to the operational model version is that neither data assimilation of observational data nor latent-heat nudging of radar data are performed. The ability of CCLM to reproduce extreme windstorms and their characteristics is documented in Born *et al.* (2012). The model domain (Figure 1(a), bold black border) covers large parts of Europe and the North Atlantic Ocean, roughly ranging from  $70^\circ\text{N}$  to  $15^\circ\text{N}$ . This large domain enables us to capture all crucial stages of the evolution of Xynthia, from its deepening phase over the southeastern North Atlantic to its decay over the Baltic Sea. Due to the large model domain, the simulations are performed with a relatively coarse horizontal resolution (compared with operational limited area weather forecast models) of  $0.22^\circ \times 0.22^\circ$  (approximately  $25\text{ km} \times 25\text{ km}$ ) and with 35 layers in the vertical. ERA-Interim data are used as boundary conditions. For time-step integration, the Runge–Kutta integration scheme is used with a time step of 144 s. The CCLM simulations are performed for the 96 h period from 0000 UTC 26 February 2010 to 0000 UTC 2 March 2010.

First, a control simulation with standard physics and undisturbed initial boundary conditions (in particular observed SST) serves as a reference run (CNTRL). Further, five sensitivity experiments are performed to investigate the role of the anomalously high SST and associated latent heat release in the development of Xynthia. In the first two sensitivity experiments (SF5, SF10) the surface heat fluxes, and thus the evaporation, over a southwestern subregion of the model domain (Figure 1, thin black box) covering the North Atlantic Ocean are reduced by modifying the respective empirical model parameters. This subregion comprises the area over which the strongest

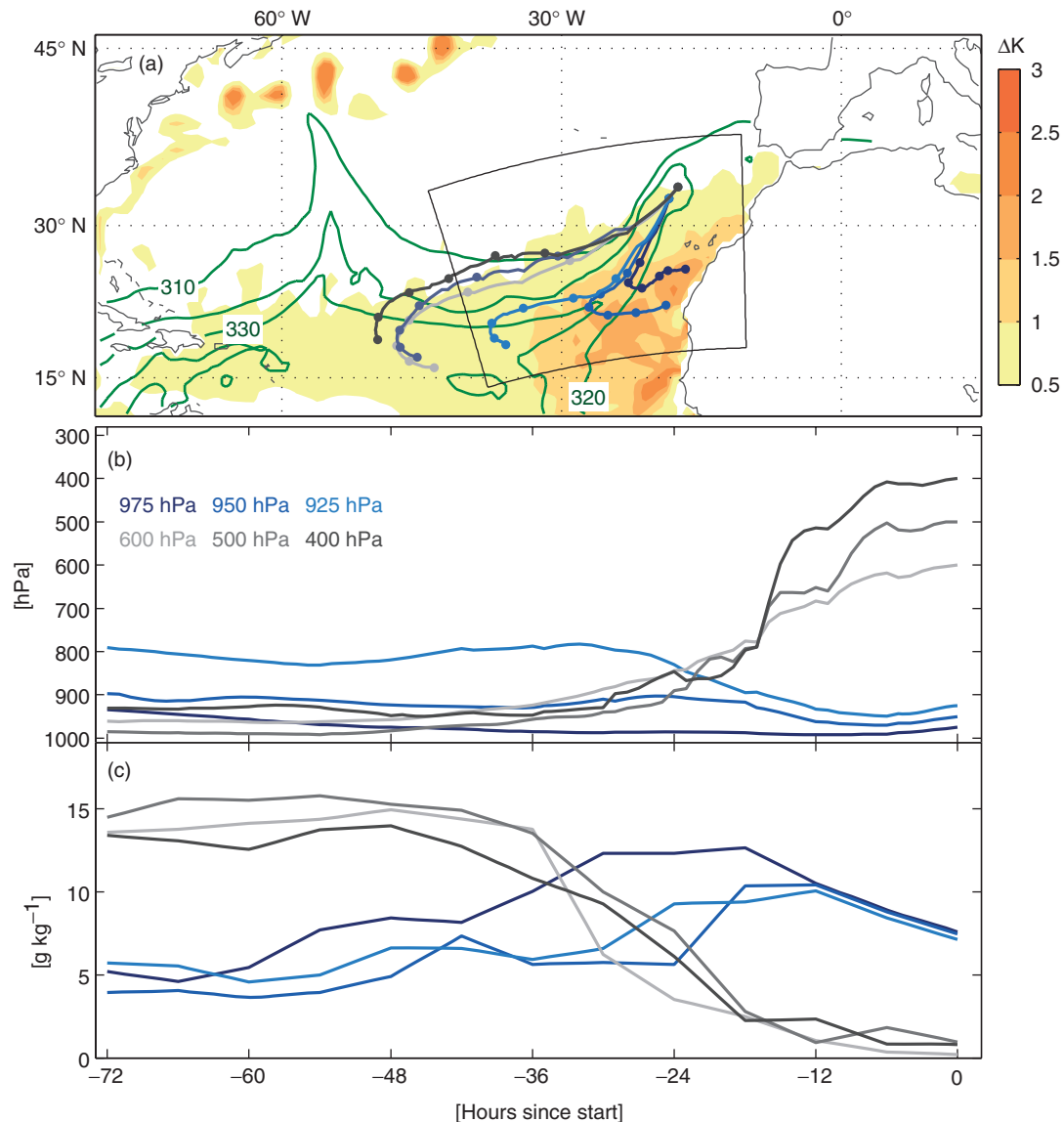


**Figure 3.** (a)  $\Theta_e$  distribution at 950 hPa (green isolines with an interval of 10 K), positive SST anomalies (shaded) and backward trajectories of airflows inside the warm sector of the cyclone. All trajectories start at 0000 UTC on 27 February and are calculated backwards for 72 h. The colours of the trajectories indicate the starting height (see 3(b) for colour key). The area where the SST is reduced in the CCLM sensitivity studies is also outlined by the black frame. (b) Pressure along the trajectories. (c) Specific humidity along the trajectories.

intensification of Xynthia was identified. Specifically, the laminar boundary roughness for heat at the surface is enhanced; the non-dimensional parameter `ram_heat` (identified to affect model results by Bellprat *et al.*, 2012) is increased from 1 to 5 (SF5) and 10 (SF10), respectively. The parameter `ram_heat` is proportional to the inverse of the transfer coefficient of heat (TCH). In turn, TCH is directly proportional to the surface latent heat flux. Thus, an increase of `ram_heat` will lead to lower TCH values and also to a reduction in surface latent-heat fluxes. A sensitivity study by Langland *et al.* (1996) showed that an increase of the transfer coefficient for the surface latent-heat flux leads to an intensified cyclone.

In the other three sensitivity experiments, the SST is stepwise reduced over the subregion defined in Figure 1. The initial SST is reduced in steps of 1 K at each model grid point in the subregion relative to that in the CNTRL to a maximum reduction of 3 K (experiments TS1 to TS3). The specific humidity in the boundary layer is assumed to decrease when surface fluxes or initial SST are reduced. To give the specific humidity sufficient time to adjust to modified surface conditions an initialization run is performed prior to each of the sensitivity runs. The initialization runs are started on 24 February 0000 UTC (2 days prior to the start time of the sensitivity runs), and provide adapted boundary layer humidity fields. Analysis of simulations with different lengths of initialization runs reveals that a lead-time of 48 h is sufficient

for humidity adjustment. Afterwards, the sensitivity runs are performed using these adjusted boundary-layer humidity fields as initial conditions at 26 February 0000 UTC. To restrict the adjustment of humidity to the boundary layer, a spectral nudging procedure (von Storch *et al.*, 2000) is applied to the initialization runs. By using this technique, the large-scale atmospheric flow fields are kept close to the driving re-analysis fields ensuring that the upper-level forcing differs only marginally from that in the control simulation. A similar approach of humidity adjustment for initializing regional climate models (RCMs) has, e.g. been applied by Etienne *et al.* (2013) for simulations over lakes in Switzerland. Surface and upper-air analysis charts provided by DWD (German weather service) as well as reports from two synoptic stations (Porto, WMO: 08545, 8.68°W, 41.23°N and Chassiron, WMO: 07314, 1.41°W, 46.05°N) are used to validate the CNTRL simulation. The locations of both synoptic stations are indicated later in Figure 5(a).

To reveal the influence of diabatic processes (see section 5) we calculated potential vorticity units (PVU) and the diabatic heating rate (DHR). The calculation of potential vorticity on isobaric surfaces follows Dickinson *et al.* (1997):

$$PV = -g \frac{\partial \theta}{\partial p} \left( f + \frac{\partial v}{\partial x} - \frac{\partial u}{\partial y} \right) + g \left( \frac{\partial v}{\partial p} \frac{\partial \theta}{\partial x} - \frac{\partial u}{\partial p} \frac{\partial \theta}{\partial y} \right) \quad (1)$$

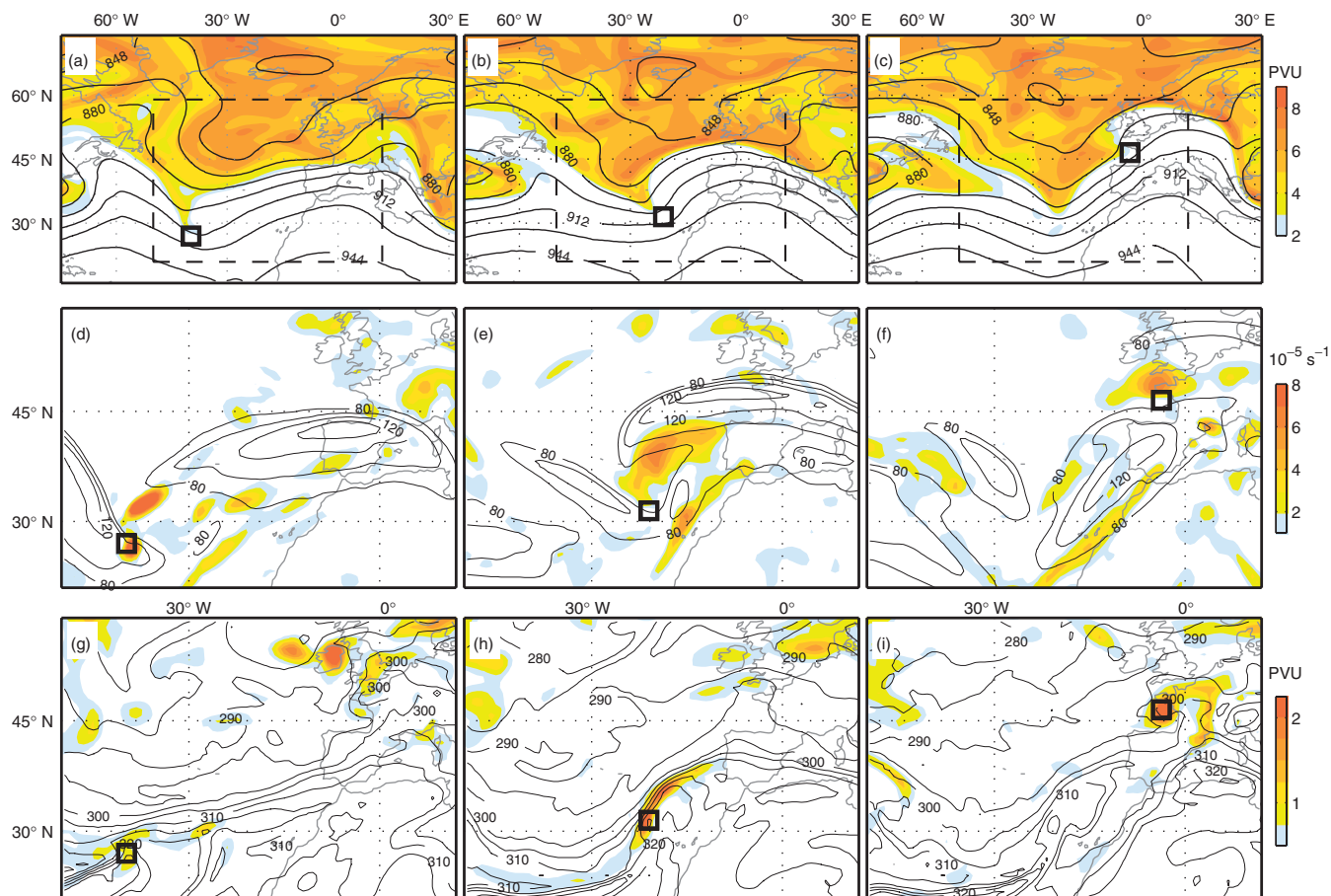


**Figure 4.** Synopsis of different meteorological parameters for three time steps during rapid intensification of Xynthia: left column 26 February 0000 UTC; centre column 27 February 0000 UTC; right column 28 February 0000 UTC. (a)–(c) PV distribution (PVU) (shaded) on the 320 K isentropic level and geopotential height at 300 hPa (black isolines with an interval of 16 gpdm); (d)–(f): jet stream (knots) (isolines) and divergence ( $10^{-5} \text{ s}^{-1}$ ) (shaded) at 300 hPa; (g)–(i) PV distribution (PVU) (shaded) and equivalent potential temperature  $\Theta_e$  (K) (contour lines, every 5 K) at 850 hPa. Please note that (d)–(i) are enlarged to the dashed box as shown in (a)–(c) for better representation of synoptic-scale variables. In all panels the black squares mark the location of the surface cyclone.

Here,  $g$  is gravity,  $\theta$  represents the potential temperature,  $f$  is the Coriolis parameter,  $p$  is the pressure level and  $u$  and  $v$  represent the zonal and meridional components of the wind, respectively. The DHR (also section 5) follows Berrisford (1988) and assumes that condensation occurs where ascending air is (nearly) saturated:

$$\dot{\theta} = \frac{-\frac{L}{c_p} \frac{\kappa \theta \omega}{p} \frac{dq_s}{dT}}{1 + \frac{L}{c_p} \frac{dq_s}{dT}} \left\{ 1 - \exp\left(\frac{h_0 - h}{5}\right) \right\} \quad (2)$$

Thereby it is assumed that the vertical velocity  $\omega < 0$  (ascending motion) and the relative humidity  $h > h_0 = 80\%$ . Variable  $L$  denotes the latent heat of condensation of water,  $c_p$  the specific heat capacity of water vapour at constant pressure,  $\kappa$  the ratio of  $R$  (gas constant) and  $c_p$  and  $q_s$  is the saturation mixing ratio. The latter term accounts for potential saturation on the subgrid scale (cf. Grams *et al.*, 2011).

### 3. Synoptic overview of the storm development

A description of the large-scale atmospheric conditions prior to and during the occurrence of Xynthia is presented in this section. Brief descriptions of Xynthia can also be found in Rivière *et al.* (2012) and Liberato *et al.* (2013). The analysis is based on ERA-Interim re-analysis data. Xynthia was initially identified on 25 February over the subtropical North Atlantic (cf. Figure 1(a)). Its development was associated with a huge snowstorm on the east coast of the United States, which modified the upper-level PV distribution and formed a PV streamer in the vicinity of developing Xynthia (Piaget, 2011). In the following days, Xynthia underwent explosive cyclogenesis and reached its lowest core pressure close to the French Atlantic coast, before it dissipated over the Baltic Sea.

As reported by Osborn (2011), the winter months prior to Xynthia were characterized by a record-breaking negative phase of the NAO. Correspondingly, the polar jet was shifted southward during most of the winter 2009/2010 (Santos *et al.*, 2013), and was located mainly around the southern peak of its trimodal climatological distribution (Woollings *et al.*, 2010). From 4 to 28 February, the polar jet was shifted to a region between 30°N and 40°N (Santos *et al.*, 2013; their Figure 1), thus forming favourable conditions for strong cyclogenesis around this latitudinal band.

A positive SST anomaly existed over most of the subtropical North Atlantic during February 2010 (Figure 2). Figure 2 also shows the presence of long-lived Gulf Stream eddies, which can be inferred from the series of alternating cold and warm anomalies in the Gulf Stream region. The SST anomaly has its maximum (exceeding 2 K) close to the West African coast, a region that is usually characterized by upwelling of cold water, as can be seen in the climatological SST mean (black isolines in Figure 2). It is also mostly above twice the standard deviation of the 30 year climatology as derived from the ERA-Interim (dotted areas in Figure 2). Hence, an increased amount of available moisture can be assumed over the subtropical North Atlantic, which in turn can lead to an enhanced release of latent heat when these air masses are lifted, potentially playing a crucial role in the development of Xynthia. Within these prevailing atmospheric conditions, a catastrophic frontal rainfall event hit the island of Madeira just 1 week before the occurrence of Xynthia (Fragoso *et al.*, 2012). The capital Funchal reported a daily precipitation of 146.9 mm, which has an estimated return period of approximately 290 years. Thus, conditions for the development of extreme hydro-meteorological events were already in place before the development of Xynthia.

To analyse the origins of air masses involved in the cyclone development in more detail, a Lagrangian backward trajectory

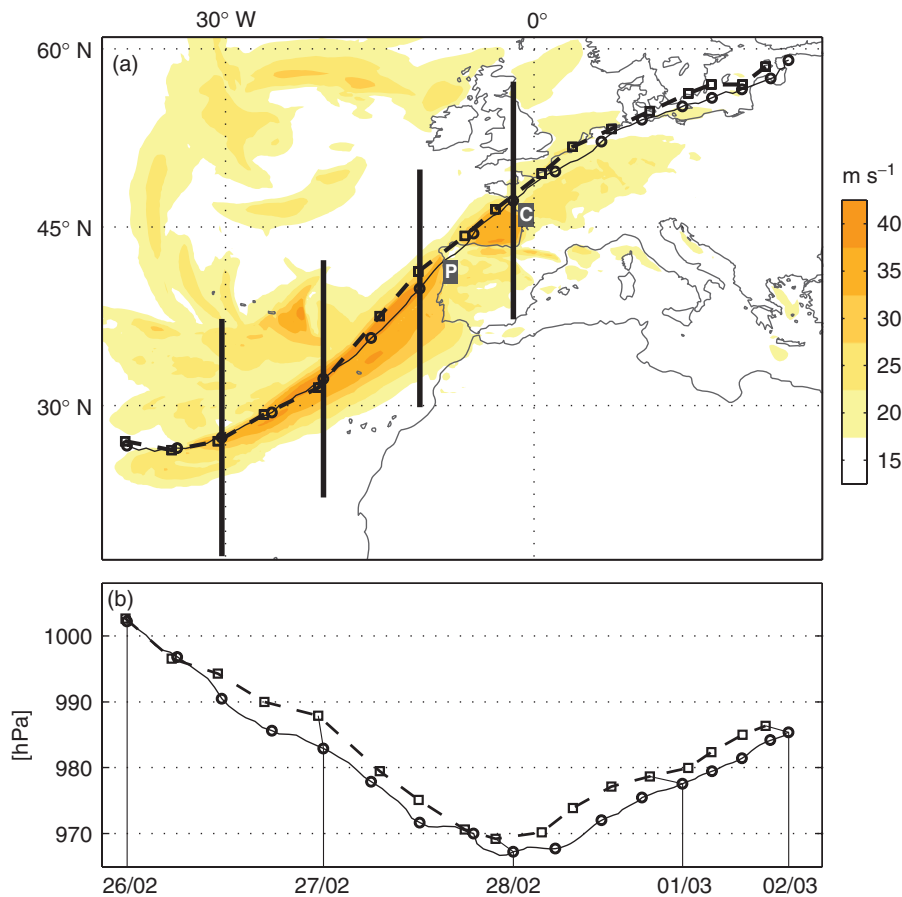


**Figure 5.** (a) Cyclone location and (b) core-pressure evolution of Xynthia as derived from the ERA-Interim (dashed line with squares) and the CNTRL (solid line with circles). First depicted point is at 26 February 0000 UTC. Squares/circles are in six-hourly intervals until 2 March 0000 UTC. (a) Shaded areas show wind signature of the storm (maximum wind gust above  $17.5 \text{ m s}^{-1}$  at each grid point during the considered period). Uppercase letters 'P' and 'C' indicate the locations of the synoptic stations Porto and Chassiron for further comparisons. The four vertical lines along the track assign the positions of north–south cross-sections shown in Figure 11. This figure is available in colour online at [wileyonlinelibrary.com/journal/qj](http://wileyonlinelibrary.com/journal/qj)

analysis (Noone and Simmonds, 1999) is performed. Trajectories starting at 0000 UTC 27 February are calculated 72 h backwards from six different tropospheric pressure levels inside the warm sector of Xynthia, which was located at this time southwest of the Portuguese coast (Figure 3(a)). The warm sector is characterized by an area of warm and moist air, indicated by high values of lower-level equivalent potential temperatures ( $\Theta_e$ ). The air mass inside the warm sector of Xynthia is found to originate from areas with anomalously warm SSTs (Figure 3(a)). Boundary-layer air masses (up to 975 hPa) originate close to the West African coast, whereas mid-tropospheric air masses (400–600 hPa) originate from the central subtropical North Atlantic. The mid-tropospheric air masses originate close to the surface (beneath 900 hPa) and are rapidly lifted over the last 36 h of the analysis (Figure 3(b)). The specific humidity of these air masses decreases significantly during the lifting (Figure 3(c)). Hence, moist air from low levels is transported to higher altitudes within the cyclone while undergoing condensation and releasing latent heat. Due to their rapid ascent, these air masses can be assigned to the warm conveyor belt of the storm, where strong lifting of air masses is typical (e.g. Carlson, 1991). For the boundary-layer air masses, which underwent only a slight descent during the last 24 h of the trajectory analysis (Figure 3(b)), a strong increase of specific humidity can be observed before reaching the cyclone core (Figure 3(c)), thus implying that humidity is gained by these air masses while flowing over warm ocean surfaces. These findings are consistent with results of Liberato *et al.* (2013), who used a more complex evaporation/precipitation Lagrangian method (Stohl *et al.*, 1998) that is able to identify the evaporative sources associated with the development of Xynthia in the subtropical North Atlantic.

Atmospheric conditions at three different times during the phase of Xynthia's rapid intensification are presented in Figure 4.

At 0000 UTC 26 February a long-wave trough at 300 hPa is centred over the North Atlantic (Figure 4(a)). A PV streamer with values of more than 4 PVU is located within the axis of the trough and the tip of the PV streamer is vertically aligned with the identified surface cyclone. The jet stream exhibits a split structure (Figure 4(d)). At the exit region of the western branch of the jet stream, which is vertically aligned with the surface cyclone, strong upper-level divergence can be observed. Hence, upper-air conditions facilitate the early development of the cyclone. At lower levels (850 hPa), the PV distribution exhibits a local maximum in the vicinity of the cyclone, reaching almost 1 PVU (Figure 4(g)). Additionally, a weaker second low-level PV maximum is located further downstream (cf. Rivière, 2012). A backwards vertical tilt between upper- and lower-level vorticity maxima is favourable for baroclinic development of the cyclone (e.g. Holton, 1979). The  $\Theta_e$  field shows a strong horizontal gradient over central and eastern parts of the subtropical North Atlantic. At this stage, the cyclone is located on the southern edge of the frontal zone.

At 0000 UTC 27 February the upper-level trough with its embedded PV streamer and the major jet structure have moved further eastward, with the cyclone still being located in the area of strong upper-level divergence between the two jet streaks (Figure 4(b) and (e)). Thus, perfect conditions for further deepening of the cyclone are provided (cf. Figure 1(b)). Close to the centre of the cyclone, the two lower-tropospheric PV maxima merged to form an elongated coherent maximum, exceeding values of more than 2 PVU (Figure 4(h)). The gradient of  $\Theta_e$  has also sharpened in the vicinity of the cyclone. We hypothesize that this increase in PV can be at least partly attributed to diabatic processes such as latent heat release through the condensation of lifted moist air. In this study the contribution of the anomalously high SSTs in the storm's genesis region to this diabatic PV component is determined.

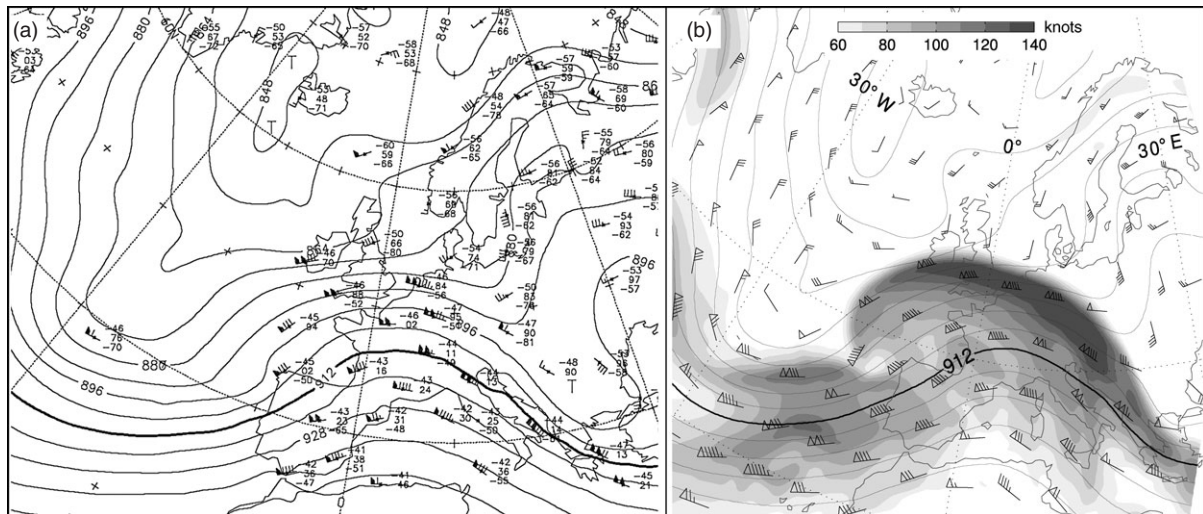


**Figure 6.** (a) Analysis of geopotential height (gpm) (contours every 8 gpm) and wind vectors by the DWD at 300 hPa on 27 February 1200 UTC; (b) as (a) but for the CNTRL. Wind speeds higher than 60 knots are shaded in intervals of 10 knots for clarification of upper level jet-stream conditions in the CNTRL.

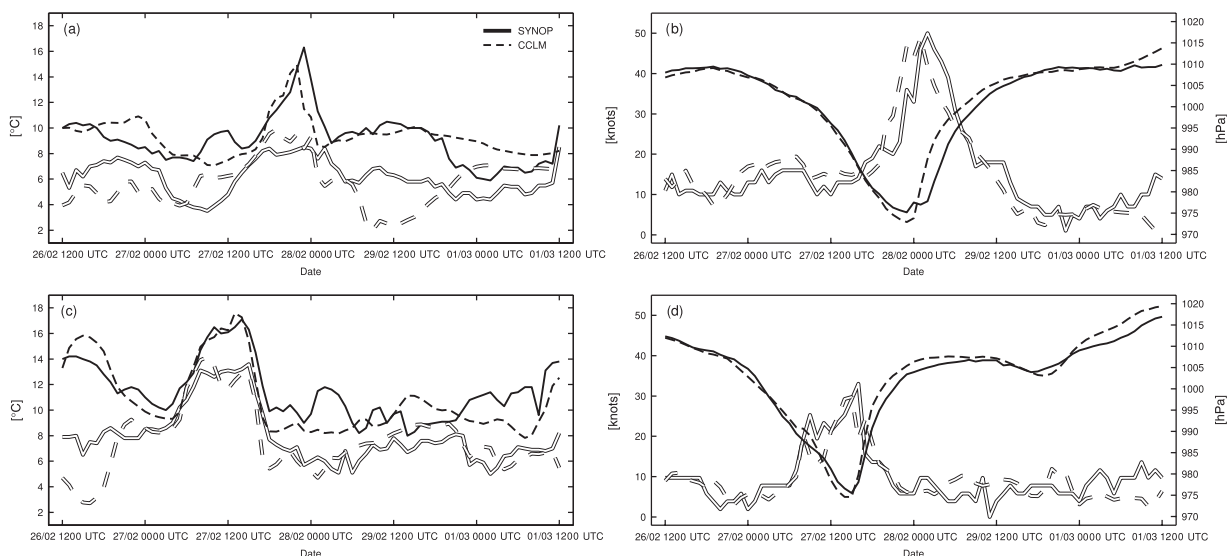


**Figure 7.** Time series for different meteorological parameters at two different locations for the CNTRL (dashed line) and synoptic stations (solid line). (a) The 2 m temperature (black, °C) and dew-point temperature (grey, °C) for CCLM grid point 164, 134 (1.20°W, 46.11°N) and synoptic station 07314 (Chassiron, 1.41°W, 46.05°N). (b) As (a) but for 10 m wind speed (grey, knots) and mean sea-level pressure (black, hPa). (c) As (a) but for CCLM grid point 140, 111 (8.55°W, 41.20°N) and synoptic station 08545 (Porto, 8.68°W, 41.23°N). (d) As (c) but for 10 m wind speed (grey, knots) and mean sea-level pressure (black, hPa). For station locations please refer to Figure 5.

At 0000 UTC 28 February the cyclone has reached its maximum intensity (see Figure 1(b)). The upper-level trough has considerably weakened (Figure 4(c)). The PV streamer has moved further to the northeast and is located over the Bay of Biscay. Upper-level divergence still exhibits locally large values, while the eastern branch of the jet stream has weakened significantly (Figure 4(f)). The cyclone core is now associated with a single contracted PV maximum exhibiting further enhanced values at 850 hPa (Figure 4(i)). Afterwards, the surface cyclone migrates further towards colder air masses and is consequently isolated from the warm and humid air masses, and thus from this energy reservoir.

#### 4. Numerical model studies

##### 4.1. Validation of the CCLM control simulation

To explicitly analyse the role of the anomalous SST and associated latent heat release for the development of Xynthia as represented in the CCLM, validation of the CNTRL experiment is first required. The CNTRL is forced with undisturbed initial conditions (including observed SSTs, see section 2), and is validated against the ERA-Interim re-analysis, the DWD analysis

and observations from the two synoptic stations – Porto and Chassiron (for location see Figure 5(a)). In general, the simulated track of Xynthia and the temporal evolution of the core pressure in the CNTRL are in good agreement with the ERA-interim re-analysis (Figure 5). The core pressure is slightly deeper in the CNTRL simulation than in the re-analysis during the period concerned. The lowest pressure is analysed from the re-analysis at 28 February 0000 UTC (969.2 hPa), located over the Bay of Biscay, while the core pressure in the CNTRL simulation occurs 2 h earlier (966.7 hPa). The simulated cyclone track is slightly shifted southwards compared with the ERA-Interim re-analysis. The simulated wind signature (maximum wind speed per grid point during the whole episode) exhibits highest wind gusts south of the track, with a maximum speed of  $45.8 \text{ m s}^{-1}$  west of the Portuguese coast (Figure 5(a)).

The 300 hPa geopotential height, upper-tropospheric wind speed and direction as simulated by the CNTRL are quite similar to the DWD analysis, which is shown for the 27 February 1200 UTC (Figure 6). As the CCLM is forced by the ERA-Interim, we chose the DWD analysis for comparison in order to have an independent dataset to evaluate the model performance. In both the DWD analysis and the CNTRL, a distinct trough over the central and eastern North Atlantic and a small ridge

over the western Mediterranean can be observed. The strong geopotential height gradient near the western coast of Spain and supergeostrophic conditions over southern France lead to high wind speeds of up to 100 knots (corresponding to  $51.44 \text{ m s}^{-1}$ ) over southwestern Europe and are simulated quite realistically by the CNTRL. The simulated upper-level jet stream (Figure 6(b)) shows a split structure with branches located over central Europe and east of the Iberian coast. This is similar to the upper-level jet stream structures observed in the re-analysis data (cf. Figure 4 and section 3).

Observed meteorological parameters at two synoptic stations, Chassiron and Porto, are compared with the CNTRL at the respective nearest model grid point (Figure 7). Chassiron is located on the island of Oleron just offshore the French Atlantic coast, where some of the most severe damage was reported (Lumbroso and Vinet, 2011). Porto is located on the Portuguese coast just south of the area where Xynthia first hit Iberia. Simulated time series of mean sea-level pressure (MSLP) and wind speed at 10 m are in good agreement with observations for both stations with respect to their temporal evolution as well as their magnitude (Figure 7(b) and (d)). Correlation coefficients between simulated and observed time series for Chassiron are 0.89 for wind speed and 0.98 for the MSLP; for Porto the same coefficients are 0.76 and 0.99, respectively. The rapid decrease of MSLP to a minimum pressure of approximately 975 hPa in the early afternoon of 27 February for Porto and around midnight on 28 February for Chassiron is well reproduced by the CCLM. On the other hand, the strong pressure increase at Chassiron after Xynthia has passed is simulated too early by the CNTRL. As a consequence, simulated wind speeds reach their maximum an hour prior to the observations at Chassiron (Figure 7(b)). Observed and simulated air and dew-point temperatures have similar time series for both synoptic stations (Figure 7(a) and (c)). A sharp increase of air and dew point temperatures can be observed at both stations as the storm passes (before and after noon on 27 February at Porto and Chassiron respectively). This strong increase is due to the passing of the warm sector of the cyclone over the respective stations and is simulated quite realistically by the CNTRL.

We conclude that the CNTRL reproduces the fundamental meteorological parameters of the re-analysis and observational data sets realistically. Therefore, the CCLM seems to be appropriate for the simulation of a windstorm such as Xynthia. The sensitivity experiments are presented in the following subsection.

#### 4.2. Results of the sensitivity experiments

The sensitivity experiments are analysed in order to quantify the role of the SST and associated latent heat release in the development of Xynthia. The main differences between the various sensitivity studies and CNTRL are modified latent heat fluxes between the surface and the atmosphere (see section 2). Figure 8 depicts latent heat fluxes for the CNTRL (Figure 8(a)) and the sensitivity experiments TS1, TS2, TS3, SF5 and SF10 (Figure 8(b)–(f)) averaged over the 48 h period from 0000 UTC 26 February 2010 to 0000 UTC 28 February 2010. As can be seen, the decrease of simulated latent-heat flux is stronger in the sensitivity experiments in which the boundary layer roughness for heat is increased (SF5 and SF10) than in those with reduced SST (TS1, TS2, TS3).

The cyclone tracks and the temporal evolution of the core pressure as simulated by TS1, TS3, SF5 and SF10 compared with results from the CNTRL are shown in Figure 9(a). During the entire period the core pressure of TS1 is above the core pressure of the CNTRL, with a difference of minimum core pressure of 4.3 hPa. This effect is strengthened in TS3, where the minimum core-pressure difference is 8.7 hPa above the CNTRL. Additionally, the absolute minimum core pressure is reached with a retardation of 9 h in TS3 compared with the CNTRL. The results of TS2 are within the range of the results of TS1

and TS3 (not shown). For all sensitivity experiments, cyclone tracks and six-hourly positions are quite similar to CNTRL (Figure 9(b)). These results suggest that decreasing the initial SST has only a small impact on the resulting cyclone track but a recognizable influence on the core pressure development. This assessment is strengthened by the results of the SF5 and SF10 experiments, which also show a clear reduction of storm intensity with minimal variations of the cyclone track compared with the CNTRL. The resulting difference of minimum core pressure is 5.8 hPa (for SF5) and 8.0 hPa (for SF10), respectively. On 27 February 2200 UTC, when the core pressure in the CNTRL reaches its absolute minimum, the deviations for the sensitivity experiment range between 5.9 hPa (TS1) and 10.3 hPa (TS3).

To further clarify the role of latent heat release on the development of Xynthia, the MSLP, low-level  $\Theta_e$  and PV distributions simulated by TS3 and SF10 are compared with the CNTRL (Figure 10). For the CNTRL a band of high  $\Theta_e$  values (vertically averaged between 900 and 950 hPa), reaching from the eastern subtropical North Atlantic along the northwest African shoreline towards the cyclone centre, is obvious at 27 February 1200 UTC (Figure 10(a)). This indicates the availability of warm moist air masses, which on lifting can release latent heat and thus contribute to the further intensification of Xynthia. Compared with the CNTRL, both TS3 (Figure 10(b)) and SF10 (Figure 10(c)) clearly show decreased and westward shifted low-level  $\Theta_e$  over the eastern North Atlantic. As PV is conserved under adiabatic frictionless conditions, positive PV anomalies in the lower troposphere are likely to be (at least partly) attributable to diabatic processes. For the CNTRL, high values of low-level PV (vertically averaged between 750 and 900 hPa) along the Portuguese coast are simulated (Figure 10(d)). In TS3 (Figure 10(e)) and SF10 (Figure 10(f)), simulated low-level PV is weaker (up to 2 PVU) in the vicinity of the cyclone compared with the CNTRL. The association with reduced low-level  $\Theta_e$  implies that the reduction is due to weaker diabatic processes in the sensitivity experiments.

Finally, the effect of the reduced surface latent heat fluxes on cyclone-related precipitation is analysed. Heavy 12-hourly accumulated precipitation of up to  $69.6 \text{ kg m}^{-2}$  along the cyclone track (with both large resolved and parametrized components) is simulated by the CNTRL (Figure 10(g)); the mean precipitation is  $10.47 \text{ kg m}^{-2}$  per grid point for a representative subdomain (see dashed box in Figure 10(g)–(i)). Less accumulated precipitation, peaking at  $64.1 \text{ kg m}^{-2}$  and with an average of  $9.4 \text{ kg m}^{-2}$  per grid point, can be observed for TS3 (Figure 10(h)). The decrease of accumulated precipitation is even stronger for SF10, with accumulated precipitation of less than  $53.1 \text{ kg m}^{-2}$  (average of  $9.1 \text{ kg m}^{-2}$  per grid point) for the entire area (Figure 10(i)). Weaker precipitation can be attributed to: (i) reduced available moisture from the sea due to reduced surface fluxes of latent heat; and/or (ii) weaker lifting during the deepening phase of the cyclone.

We conclude that the artificial reduction of surface latent heat fluxes inhibits the intensification of the cyclone, the development of PV through diabatic processes and cyclone precipitation.

#### 4.3. Vertical perspective on the PV development

Analysing the vertical distribution of PV anomalies and diagnosis of diabatic heating rate (DHR, section 2) provides more profound insights into the role of latent heat release on the intensification phase of Xynthia. Here we consider vertical cross-sections of PV and DHR centred over the surface cyclone and averaged over  $4^\circ$  in the east–west direction and extends  $20^\circ$  in the north–south direction. Figure 11(a)–(d) shows the south–north orientated vertical sections of PV and relative humidity (RH) for the CNTRL for different stages of development. The geographical locations of the cross-sections are shown in Figure 5(a). At 26 February 1200 UTC, high PV values can be observed in the upper troposphere with maximum values at the tropopause level (Figure 11(a)). This is consistent with the identified upper-level

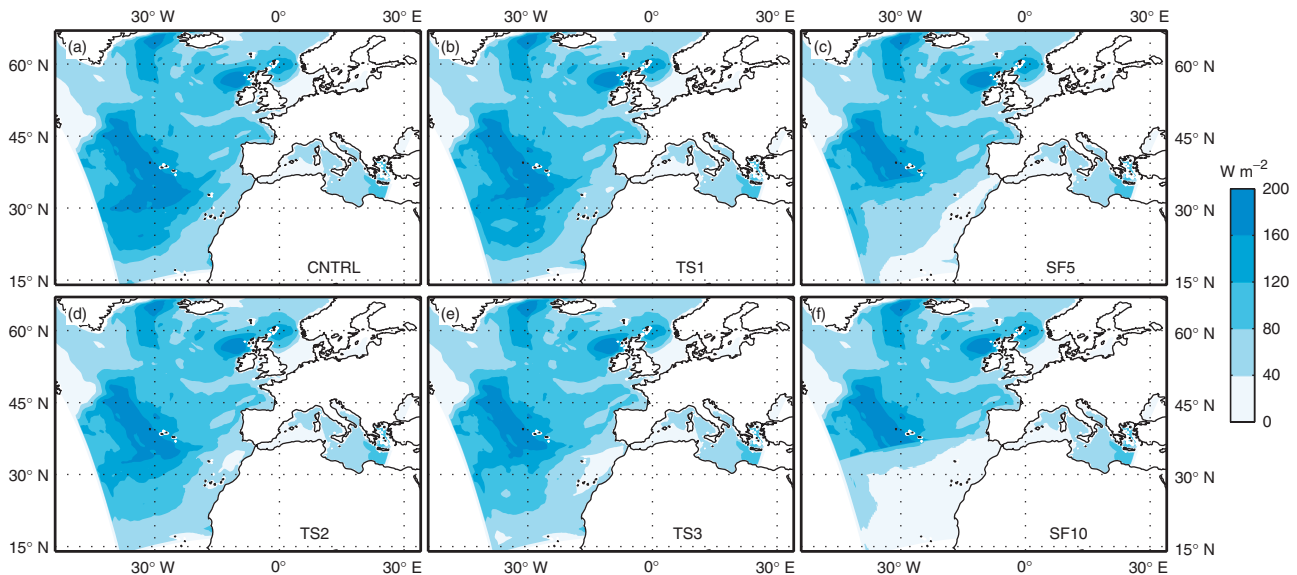


**Figure 8.** Averaged latent-heat fluxes at sea surface (in  $\text{W m}^{-2}$ ) for the period 26 February 2010, 0000 UTC to 28 February 2010, 0000 UTC. (a) Undisturbed control simulation, (b) sensitivity study TS1 with 1 K reduction of SST, (c) sensitivity study SF5 with  $\text{ram\_heat} = 5$ , (d) sensitivity study TS2 with 2 K reduction of SST, (e) sensitivity study TS3 with 3 K reduction of SST and (f) sensitivity study SF10 with  $\text{ram\_heat} = 10$ . For more details see text. This figure is available in colour online at [wileyonlinelibrary.com/journal/qj](http://wileyonlinelibrary.com/journal/qj)

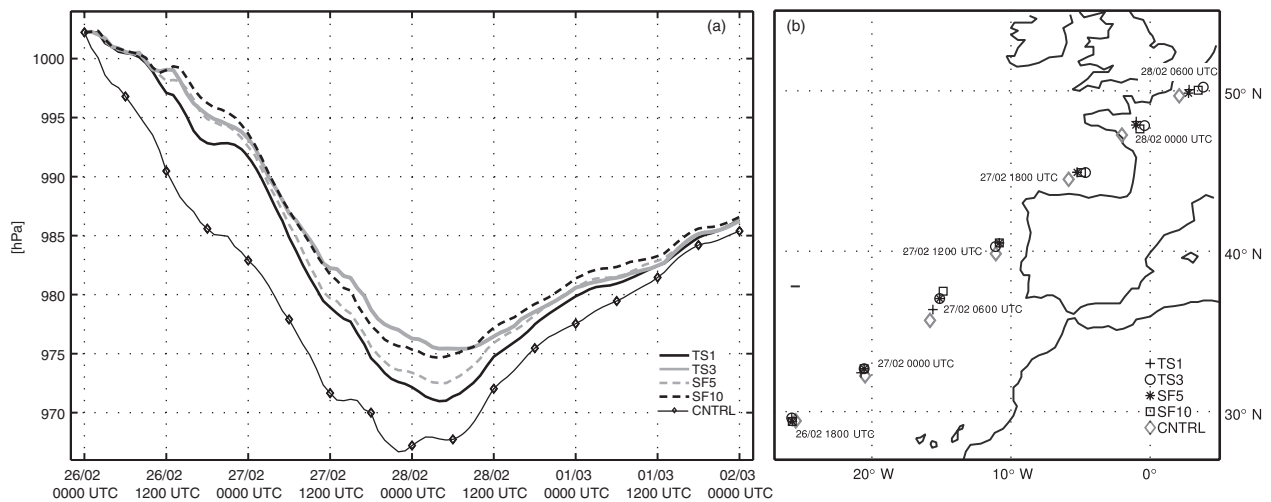


**Figure 9.** (a) Core-pressure evolution and (b) cyclone locations for various sensitivity experiments. For better presentation of the results, only results for TS1 (black/plus symbol), TS3 (grey/circle), SF5 (dashed grey/asterisk) and SF10 (dashed black/square) are included. For reference the core-pressure evolution and location for the CNTRL (diamond symbols) are included.

PV streamer as shown in Figure 4(a)–(c). A secondary simulated PV maximum can be seen at mid-tropospheric levels that may be attributed to diabatic heating processes within the warm conveyor belt. Hence, crucial atmospheric conditions for a rapid cyclone development are present. Further, north of the surface cyclone centre moist air masses with RH of more than 80% reach up above 500 hPa, reflecting the upward transport of warm and moist air within the warm conveyor belt of the cyclone. Twelve hours later a distinct PV tower with two regions of maximum PV extends from the surface to the upper troposphere right above surface cyclone (Figure 11(b)). The PV tower is the result of the merging of diabatically produced PV and upper-level PV. Additionally, the region of moist air north of the cyclone has further enlarged, which is an indicator of the ongoing uplifting of humid air masses on 27 February 0000 UTC. Above this region, lower values of PV occur as the result of reduced PV above the area of strongest latent heat release. South of the cyclone a region of dry mid-tropospheric air develops, associated with the dry intrusion (Browning, 1997). On 27 February 1200 UTC, the low and mid-troposphere above the surface cyclone is still characterized by an amplified PV tower (Figure 11(c)). While moist air is still advected to upper levels within the warm conveyor belt of the cyclone, the dry intrusion south of the surface cyclone extends downwards to 700 hPa.

At peak intensity of the storm, 28 February 0000 UTC, the PV tower extends throughout the whole troposphere. Values of up to 3 PVU are visible at lower levels, consistent with diabatic processes taking place there. To the north, moist air is still reaching to higher levels, while the dry intrusion to the south manifests itself at mid-tropospheric levels.

The impact of diabatic processes on the PV structure of the storm is demonstrated by horizontally averaging PV over a  $4^\circ \times 4^\circ$  box centred on the surface cyclone in the CNTRL and the sensitivity experiments TS3 and SF10 (Figure 11(e)–(h)). The diagnoses of the DHR confirm the influence of diabatic processes on the development of the storm. A strong DHR occurs within the corresponding air column at lower and mid-tropospheric levels during the deepening phase of the storm. Although on 26 February 1200 UTC the vertical distribution of PV is very similar in the three simulations (Figure 11(e)), PV is reduced in both sensitivity experiments in the lower troposphere at later times (Figure 11(f)–(h)). A decrease of PV of up to 0.9 PVU can be seen for 27 February 1200 UTC (Figure 11(g)). This coincides with a reduction in the DHR of  $0.5 \text{ K h}^{-1}$  for TS3 and SF10, respectively. At the same time, upper-level PV values (300–500 hPa) in the sensitivity experiments are enhanced in relation to the CNTRL. The enhanced PV at 500 hPa in TS3, and

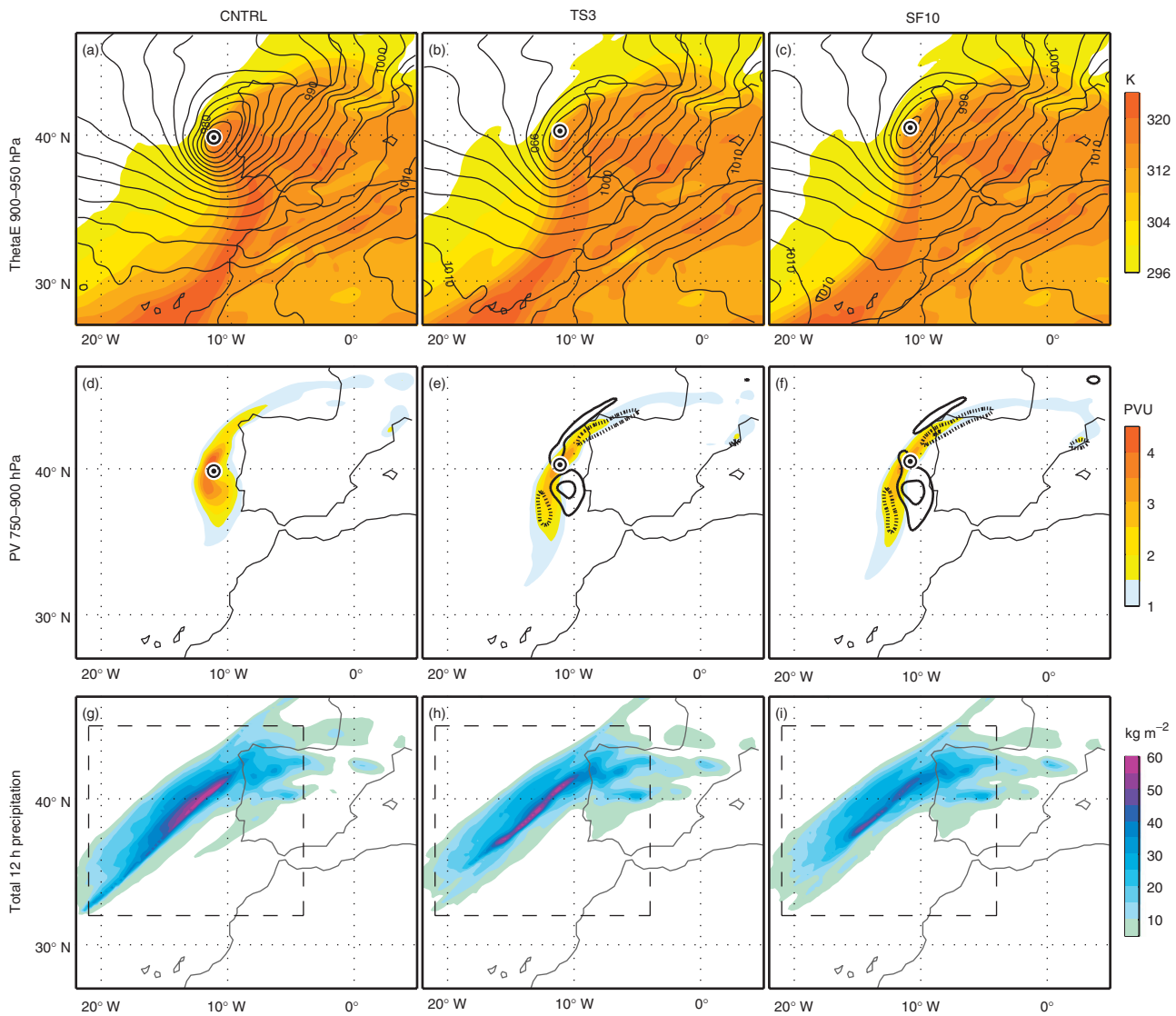


**Figure 10.** (Top row) Mean sea-level pressure (contour each 2.5 hPa) and vertically averaged  $\Theta_e$  between 900 and 950 hPa on 27 February 1200 UTC for (a) CNTRL, (b) TS3 and (c) SF10. (Centre row) as (a) to (c), but for lower-tropospheric PV vertically averaged between 750 and 900 hPa. ((e) and (f) Negative (positive) PV differences of TS3 - CNTRL and SF10 - CNTRL contoured as thick (dashed) black lines (contour interval 1 PVU). For (a)–(f), black/white circles indicate corresponding cyclone position. (Bottom row) As (a) to (c) but for 12 h precipitation accumulation on 27 February between 0000 UTC and 1200 UTC. Comparative values for precipitation are calculated in the box marked by the dashed line (see text for details).

more clearly in SF10, is related to the reduced DHR just below 500 hPa. The overall weakened negative vertical gradient in PV in the sensitivity experiments can be attributed to the weaker DHR at mid-tropospheric levels. On 28 February 0000 UTC (Figure 11(h)) it is noticeable that the DHR at lower levels has generally reduced by approximately  $2 \text{ K h}^{-1}$  since 27 February 1200 UTC, while at upper levels only the sensitivity experiments show a marked reduction of the DHR. In particular the reduction of the DHR at lower levels implies that the peak storm intensity has been reached (cf. Figure 9). To summarize, these results again clearly indicate the important role of moisture processes in the cyclogenesis of Xynthia and their contribution to the weaker intensification of the storm in the TS and SF experiments (cf. Figure 9(a)).

## 5. Summary and conclusion

The role of the anomalously high SST and associated latent heat release in the development of the exceptional windstorm Xynthia in early 2010 has been analysed. The record breaking negative phase of the NAO during the winter 2009/2010 was associated with a southward shift of the polar jet stream. These conditions favoured the development of Xynthia around  $30^\circ\text{N}$  near an area with anomalously warm SSTs, even for the subtropical North Atlantic. The occurrence of an upper-level PV streamer, a

split jet stream associated with strong divergence and enhanced baroclinicity further contributed to the intensification of Xynthia. Results of two different sets of sensitivity experiments with the CCLM demonstrate the importance of the enhanced SST and surface latent heat fluxes to the development of Xynthia.

Our findings regarding the main atmospheric driving factors during the intensification of Xynthia are in agreement with a variety of studies on extratropical cyclones. In more detail, these driving factors are the existence of a strong jet stream with accompanied horizontal divergence, enhanced baroclinicity and availability of latent heat energy. Further, the importance of a split jet structure analysed during the stage of rapid intensification has already been ascertained for recent windstorms such as Lothar, Kyrill and Klaus (Wernli *et al.*, 2002; Liberato *et al.*, 2011; Fink *et al.*, 2012). In general, a prevailing negative NAO reduces the total number of extreme cyclones over the North Atlantic, but increases the number of systems travelling towards southwestern Europe (e.g. Raible, 2007; Pinto *et al.*, 2009). Thus, Xynthia may be seen as exemplary case study for extreme cyclogenesis over the subtropical eastern North Atlantic.

The quantification of dry baroclinic *versus* moist diabatic processes (e.g. Fink *et al.*, 2012) reveals the importance of diabatic processes during the intensification of windstorms such as Xynthia. Here, this is estimated by considering regional model simulations with perturbed physics. Langland *et al.* (1996)

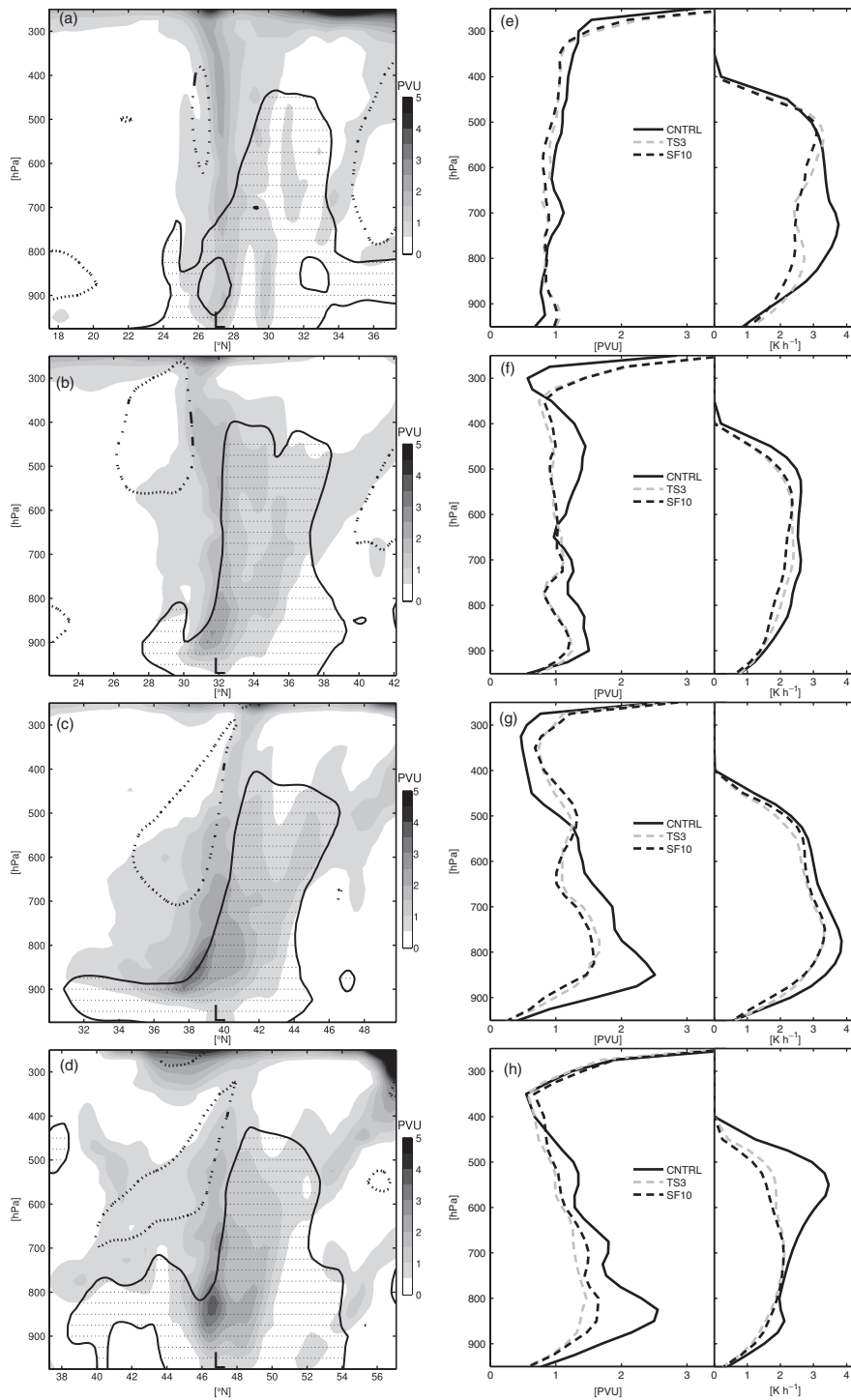


**Figure 11.** (a)–(d) South–north orientated vertical sections of the PV distribution (PVU) at different time steps (for positions of cross-sections see Figure 5). The PV and relative humidity (dashed isoline: 20% RH; dotted area: RH > 80%) for the CNTRL at (a) 26 February 1200 UTC, (b) 27 February 0000 UTC, (c) 27 February 1200 UTC and (d) 28 February 0000 UTC. The location of the surface low is indicated by ‘L’. (e)–(h) Vertical distribution of horizontally averaged PV (left, PVU) and diabatic heating rate ( $\dot{\theta}$ , right,  $\text{K h}^{-1}$ ) over a  $4^\circ \times 4^\circ$  box centred on the surface cyclone at different time steps for the CNTRL (solid black line), TS3 (dashed grey line) and SF10 (dashed black line). Time steps in (e)–(h) according to (a)–(d).

showed that the intensification of an idealized extratropical cyclone was sensitive to increasing the transfer coefficient of the surface latent heat flux. In our sensitivity experiments, the surface heat fluxes were artificially reduced by increasing the laminar boundary roughness length for heat (*rlam\_heat*; cf. Bellprat *et al.*, 2012) or reducing the SST. The results of our sensitivity studies with the CCLM confirm the importance of diabatic processes for Xynthia, as these experiments show a weaker and retarded intensification of the storm. The contribution of enhanced SSTs to the intensification of extratropical storms has been discussed by several modelling studies, e.g. for storm Lothar (Wernli *et al.*, 2002). Our results are also in accordance with other studies addressing the influence of SST anomalies on the development of storms. For instance, Booth *et al.* (2012) analysed the sensitivity

of mid-latitude storm intensification to perturbations in the SST near the Gulf Stream, revealing that enhanced SSTs lead to stronger storms. The same relationship had also been found by Giordani and Caniaux (2001).

The formation of a PV tower is a typical characteristic of strong extratropical cyclones (e.g. Wernli *et al.*, 2002; Campa and Wernli, 2012). As Xynthia intensifies, a strong PV tower develops above the surface cyclone within our control simulation. Likewise, we are able to show the existence of an upper-level stratospheric intrusion (PV streamer) that merges with a diabatically produced PV anomaly at low and mid-levels. This interaction is typical for east Atlantic cyclones, where upper-level forcing and mid-level latent heating are of equal importance (cf. Dacre and Gray, 2013). The results of the DHR diagnosis and the decrease of the PV

tower in our sensitivity experiments demonstrate the importance of available low-level moisture for the diabatic processes during the intensification of the storm. The large values of low-level PV can be attributed to high potential temperatures at the surface (Campa and Wernli, 2012). Sensitivity studies with reduced SST or with increased laminar boundary roughness for heat showed a reduction of surface latent heat fluxes, inducing both a weaker and generally retarded development of the cyclone, and a weakening of the PV tower, particularly at lower levels (cf. Figure 11(f) and (g)). This fact along with the overall reduced DHR in the sensitivity experiments corroborates our hypothesis that anomalously high values of SST over the subtropical North Atlantic and the associated latent heat release were instrumental for the development of Xynthia.

A pertinent scientific question is the potential impact of increasing greenhouse gas forcing on storms undergoing explosive development on the southern edge of the North Atlantic storm track (around 35°N to 45°N), such as Klaus (Liberato *et al.*, 2011) and Xynthia. For example, Pinto *et al.* (2009) argued that the conditions for such intense developments close to Europe may be more favourable under future climate conditions, and suggested that the importance of diabatic processes during the intensification of extreme cyclones may significantly increase. Further, Bengtsson *et al.* (2009) estimated that the most prominent change in storm characteristics under future climate conditions is a significant increase in total precipitation. Based on these and other studies, we suggest that storms such as Xynthia may occur more frequently under future climate conditions, increasing the windstorm risk for southwestern Europe.

### Acknowledgements

We thank the European Centre for Medium-range Weather Forecasts (ECMWF, UK) for providing the ERA-Interim re-analysis data. We thank the German Climate Computer Centre (DKRZ, Hamburg) for computer and storage resources within the context of DKRZ project ANDIVA (Number 105). We thank Andreas H. Fink (University of Cologne) for discussions.

### References

- Ahmadi-Givi F, Graig GC, Plant RS. 2004. The dynamics of a midlatitude cyclone with very strong latent-heat release. *Q. J. R. Meteorol. Soc.* **130**: 295–323, doi: 10.1256/qj.02.226.
- Baehr C, Pouponneau B, Ayrault F, Joly A. 1999. Dynamical characterization of the FASTEX cyclogenesis cases. *Q. J. R. Meteorol. Soc.* **125**: 3469–3494.
- Barras V, Simmonds I. 2009. Observation and modeling of stable water isotopes as diagnostics of rainfall dynamics over southeastern Australia. *J. Geophys. Res.* **114**: D23308, doi: 10.1029/2009JD012132.
- Bedacht E, Hofherr T. 2011. Wintersturm Xynthia in Südwesteuropa und Deutschland. *Munich Re Topics Geo*, 2010, 18–21 (in German).
- Bellprat O, Kotlarski S, Lüthi D, Schär C. 2012. Exploring perturbed physics ensembles in a regional climate model. *J. Climate* **25**: 4582–4599.
- Bengtsson L, Hodges KI, Keenlyside N. 2009. Will extratropical storms intensify in a warmer climate? *J. Clim.* **22**: 2276–2301.
- Berrisford P. 1988. Potential vorticity in extratropical cyclones, PhD thesis, University of Reading: Reading, UK.
- Booth JF, Thompson L, Patoux J, Kelly KA. 2012. Sensitivity of midlatitude storm intensification to perturbations in the sea surface temperature near the Gulf stream. *Mon. Weather Rev.* **140**: 1241–1256.
- Born K, Ludwig P, Pinto JG. 2012. Wind gust estimation for mid-European winter storms: Towards a probabilistic view. *Tellus A* **64**: 17471.
- Browning KA. 1997. The dry intrusion perspective of extra-tropical cyclone development. *Meteorol. Appl.* **4**: 317–324.
- Campa J, Wernli H. 2012. A PV perspective on the vertical structure of mature midlatitude cyclones in the Northern Hemisphere. *J. Atmos. Sci.* **69**: 725–740.
- Carlson TN. 1991. *Mid-latitude Weather Systems*. Harper Collins: London.
- Chagnon JM, Gray SL, Methven J. 2013. Diabatic processes modifying potential vorticity in a North Atlantic cyclone. *Q. J. R. Meteorol. Soc.* **139**: 1270–1282.
- Chang CB, Perkey DJ, Kreitzberg CW. 1982. A numerical case study of the effects of latent heating on a developing wave cyclone. *J. Atmos. Sci.* **39**: 1555–1570.
- Dacre HF, Gray SL. 2009. The spatial distribution and evolution characteristics of North Atlantic cyclones. *Mon. Weather Rev.* **137**: 99–115.
- Dacre HF, Gray SL. 2013. Quantifying the climatological relationship between extratropical cyclone intensity and atmospheric precursors. *Geophys. Res. Lett.* **40**: 2322–2327, doi: 10.1002/grl.50105.
- Danard MB. 1964. On the influence of released latent heat on cyclone development. *J. Appl. Meteorol.* **3**: 27–37.
- Davis CA, Emanuel KA. 1991. Potential vorticity diagnostics of cyclogenesis. *Mon. Weather Rev.* **119**: 1929–1953.
- Dee DP, Uppala SM, Simmons AJ, Berrisford P, Poli P, Kobayashi S, Andrae U, Balmaseda MA, Balsamo G, Bauer P, Bechtold P, Beljaars ACM, van de Berg L, Bidlot J, Bormann N, Delsol C, Dragani R, Fuentes M, Geer AJ, Haimberger L, Healy SB, Hersbach H, Holm EV, Isaksen I, Kallberg P, Köhler M, Matricardi M, McNally AP, Monge-Sanz BM, Morcrette J-J, Park B-K, Peubey C, de Rosnay P, Tavolato C, Thépaut J-N, Vitart F. 2011. The ERA-Interim re-analysis: Configuration and performance of the data assimilation system. *Q. J. R. Meteorol. Soc.* **137**: 553–597, doi: 10.1002/qj.828.
- Deveson ACL, Browning KA, Hewson TD. 2002. A classification of FASTEX cyclones using a height-attributable quasi-geostrophic vertical-motion diagnostic. *Q. J. R. Meteorol. Soc.* **128**: 93–117.
- Dickinson MJ, Bosart LF, Bracken WE, Hakim GJ, Schultz DM, Bedrick MA, Tyle KR. 1997. The March 1993 superstorm cyclogenesis: Incipient phase synoptic- and convective-scale flow interaction and model performance. *Mon. Weather Rev.* **125**: 3041–3072.
- Etienne C, Goyette S, Kuszli C-A. 2013. Numerical investigations of extreme winds over Switzerland during 1990–2010 winter storms with the Canadian Regional Climate Model. *Theor. Appl. Climatol.* **113**: 529–547.
- Fink AH, Pohle S, Pinto JG, Knippertz P. 2012. Diagnosing the influence of diabatic processes on the explosive deepening of extratropical cyclones. *Geophys. Res. Lett.* **39**: L07803, doi: 10.1029/2012GL051025.
- Fragoso M, Trigo RM, Pinto JG, Lopes S, Lopes A, Ulbrich S, Magro C. 2012. The 20 February 2010 Madeira flash-floods: Atmospheric controls and extreme rainfall assessment. *Nat. Hazards Earth Syst. Sci.* **12**: 715–730.
- Giordani H, Caniaux G. 2001. Sensitivity of cyclogenesis to sea surface temperature in the northwestern Atlantic. *Mon. Weather Rev.* **129**: 1273–1295.
- Grams CM, Wernli H, Böttcher M, Campa J, Corsmeier U, Jones SC, Keller JH, Lenz C-J, Wiegand L. 2011. The key role of diabatic processes in modifying the upper-tropospheric wave guide: A North Atlantic case study. *Q. J. R. Meteorol. Soc.* **137**: 2174–2193.
- Gray SL, Dacre HF. 2006. Classifying dynamical forcing mechanisms using a climatology of extratropical cyclones. *Q. J. R. Meteorol. Soc.* **132**: 1119–1137.
- Holton JR. 1979. *An Introduction to Dynamic Meteorology* (2nd edn). Academic Press: New York, NY.
- Hoskins BJ. 1990. Theory of extratropical cyclones. In *Extratropical Cyclones. The Erik Palmén Memorial Volume*, Newton C, Holopainen EO (eds.): 63–80 American Meteorological Society: Boston, MA.
- Hoskins BJ, Hodges KI. 2002. New perspectives on the Northern Hemisphere winter storm tracks. *J. Atmos. Sci.* **59**: 1041–1061.
- Hoskins BJ, Valdes PJ. 1990. On the existence of storm-tracks. *J. Atmos. Sci.* **47**: 1854–1864.
- Hoskins B, McIntyre ME, Robertson AW. 1985. On the use and significance of isentropic potential vorticity maps. *Q. J. R. Meteorol. Soc.* **111**: 877–946.
- Joos H, Wernli H. 2012. Influence of microphysical processes on the potential vorticity development in a warm conveyor belt: A case study with the limited area model COSMO. *Q. J. R. Meteorol. Soc.* **138**: 407–418.
- Lamb HH. 1991. *Historic Storms of the North Sea, British Isles, and Northwest Europe*. Cambridge University Press: Cambridge, UK.
- Langland RH, Elsberry RL, Errico RM. 1996. Adjoint sensitivity of an idealized extratropical cyclone with moist physical processes. *Q. J. R. Meteorol. Soc.* **122**: 1891–1920.
- Liberato MLR, Pinto JG, Trigo IF, Trigo RM. 2011. Klaus – an exceptional winter storm over northern Iberia and southern France. *Weather* **66**: 330–334.
- Liberato MLR, Pinto JG, Trigo RM, Ludwig P, Ordóñez P, Yuen D, Trigo IF. 2013. Explosive development of winter storm Xynthia over the southeastern North Atlantic. *Nat. Hazards Earth Syst. Sci.* **13**: 2239–2251, doi: 10.5194/nhess-13-2239-2013.
- Lumbroso DM, Vinet F. 2011. A comparison of the causes, effects and aftermaths of the coastal flooding of England in 1953 and France in 2010. *Nat. Hazards Earth Syst. Sci.* **11**: 2321–2333.
- Massacand AC, Wernli H, Davies HC. 1998. Heavy precipitation on the Alpine southside: An upper-level precursor. *Geophys. Res. Lett.* **25**: 1435–1438, doi: 10.1029/98GL50869.
- Massacand AC, Wernli H, Davies HC. 2001. Influence of upstream diabatic heating upon an Alpine event of heavy precipitation. *Mon. Weather Rev.* **129**: 2822–2828.
- Noone D, Simmonds I. 1999. A three-dimensional spherical trajectory algorithm. In *Research Activities in Atmospheric and Oceanic Modelling*, Report No. 28, WMO/TD-No. 942. Ritchie H. (ed.): 3.26–3.27. World Meteorological Organization: Chicago, IL.
- Osborn TJ. 2011. Winter 2009/10 temperatures and a record-breaking North Atlantic Oscillation index. *Weather* **66**: 19–21.
- Piaget N. 2011. 'Genesis of winter storm Xynthia', Master thesis. IACETH: Zürich, Switzerland.
- Pinto JG, Zacharias S, Fink AH, Leckebusch GC, Ulbrich U. 2009. Factors contributing to the development of extreme North Atlantic cyclones and their relationship with the NAO. *Clim. Dyn.* **32**: 711–737.
- Plant RS, Craig GC, Gray SL. 2003. On a threefold classification of extratropical cyclo-genesis. *Q. J. R. Meteorol. Soc.* **129**: 2989–3012.
- Pomroy HR, Thorpe AJ. 2000. The evolution and dynamical role of reduced upper-tropospheric potential vorticity in intensive observing period one of FASTEX. *Mon. Weather Rev.* **128**: 1817–1834.

- Raible CC. 2007. On the relation between extremes of midlatitude cyclones and the atmospheric circulation using ERA40. *Geophys. Res. Lett.* **34**: L07703, doi: 10.1029/2006GL029084.
- Reed RJ, Stoelinga MT, Kuo Y-H. 1992. A model-aided study of the origin and evolution of the anomalously high potential vorticity in the inner region of a rapidly deepening marine cyclone. *Mon. Weather Rev.* **120**: 893–913.
- Rivière G, Arbogast P, Lapeyre G, Maynard K. 2012. A potential vorticity perspective on the motion of a mid-latitude winter storm. *Geophys. Res. Lett.* **39**: L12808, doi: 10.1029/2012GL052440.
- Robertson FR, Smith PJ. 1983. The impact of model moist processes on the energetics of extratropical cyclones. *Mon. Weather Rev.* **111**: 723–744.
- Rockel B, Will A, Hense A. (eds.) 2008. Special issue: Regional climate modelling with COSMO-CLM (CCLM). *Meteorol. Z.* **17**: 347–348.
- Santos JA, Woollings T, Pinto JG. 2013. Are the winters 2010 and 2012 archetypes exhibiting extreme opposite behavior of the North Atlantic jet stream? *Mon. Weather Rev.* **141**: 3626–3640, doi:10.1175/MWR-D-13-00024.1.
- Snyder C, Lindzen RS. 1991. Quasi-geostrophic Wave-CISK in an unbounded baroclinic shear. *J. Atmos. Sci.* **48**: 76–86.
- Stohl A, Hittenberger M, Wotawa G. 1998. Validation of the Lagrangian particle dispersion model FLEXPART against large scale tracer experiment data. *Atmos. Environ.* **32**: 4245–4264.
- von Storch H, Langenberg H, Feser F. 2000. A spectral nudging technique for dynamical downscaling purposes. *Mon. Weather Rev.* **128**: 3664–3673.
- Swiss Re 2008. *Natural Catastrophes and Man-made Disasters in 2007: High Losses in Europe*, Sigma, Nr. 1/2008. Swiss Re Publishing: Zürich, Switzerland. <http://www.swissre.com/sigma/>.
- Trigo IF. 2006. Climatology and interannual variability of storm-tracks in the Euro-Atlantic sector: A comparison between ERA-40 and NCEP/NCAR reanalyses. *Clim. Dyn.* **26**: 127–143.
- Uccellini LW. 1990. Process contributing to the rapid development of extratropical cyclones. In *Extratropical Cyclones, The Erik Palmén Memorial Volume*, Newton C, Holopainen EO (eds.): 81–105. American Meteorological Society: Boston, MA.
- Uccellini LW, Johnson DR. 1979. The coupling of upper and lower tropospheric jet streaks and implications for the development of severe convective storms. *Mon. Weather Rev.* **107**: 682–703.
- Wanner H, Bronnimann S, Casty C, Gyalistras D, Luterbacher J, Schmutz C, Stephenson DB, Xoplaki E. 2001. North Atlantic oscillation. Concepts and studies. *Surv. Geophys.* **22**: 321–382.
- Wernli H, Davies HC. 1997. A Lagrangian-based analysis of extratropical cyclones. I: The method and some applications. *Q. J. R. Meteorol. Soc.* **123**: 467–489.
- Wernli H, Dirren S, Liniger MA, Zillig M. 2002. Dynamical aspects of the life cycle of the winter storm 'Lothar' (24–26 December 1999). *Q. J. R. Meteorol. Soc.* **128**: 405–429.
- Willison J, Robinson W, Lackmann G. 2013. The importance of resolving mesoscale latent heating in the North Atlantic stormtrack. *J. Atmos. Sci.* **70**: 2234–2250.
- Woollings T, Hannachi A, Hoskins B. 2010. Variability of the North Atlantic eddy-driven jet stream. *Q. J. R. Meteorol. Soc.* **136**: 856–868.



## 6. Summary of the results and outlook

In this thesis recent severe extratropical cyclones affecting Europe are investigated by means of partly high-resolution COSMO-CLM simulations. The focuses are (i) on the realistic simulation of winter storm events and their associated wind gust distributions and (ii) on the understanding of dynamic aspects and mesoscale processes that are relevant during the genesis and development of individual winter storm events like Kyrill (January 2007) and Xynthia (February 2010). The estimation of area-wide wind gusts is considered by applying a new physical based wind gust estimation to the COSMO-CLM and validated on basis of an ensemble of 158 simulated historical winter storm events against observations at 37 sites in Germany. After the model was evaluated to simulate winter storm events realistically, the consideration of individual exceptional storm events with COSMO-CLM provides new insights on the dynamical and mesoscale aspects during their genesis and further development. The outcomes provide the basis for further research on these special kinds of winter storm events. To conclude, this thesis contributes to research focuses particularly on the mesoscale modelling of extratropical cyclones and can be summarised as follows:

- The COSMO-CLM is able to reproduce severe winter storm events realistically.
- The introduction of a new physically based wind gust estimation method provides comparable results to existing wind gust estimation methods and furthermore permits the estimation of uncertainties by introducing a probabilistic approach.
- The development and impacts of Kyrill are substantially influenced by secondary cyclogenesis at the occluded front over the eastern North Atlantic. So far, this rare case is not considered in review articles on this topic. Negative stretching deformation as well as diabatic processes were found to play a major role during the secondary cyclogenesis. The occurrence of strong surface wind gusts along the cold front of Kyrill is associated with downward mixing of high momentum air above the boundary layer.
- Sensitivity studies with regard to changes in SST reveal the importance of diabatic processes, which are of significant influence for the development of far southern originating winter storm Xynthia.

In the following, the contents and outcomes of the individual papers are summarised in more detail. Afterwards, the results are briefly discussed and possible areas of future application are presented.

### **6.1 Paper I**

Paper I introduces a new physical based wind gust estimation method that has been implemented to the COSMO-CLM with the intention of providing realistic area-wide patterns of the distribution of surface wind gusts. The method was developed to take into account turbulent kinetic energy (TKE, therefore being referred to as TKE-method), a quantity that is available as a prognostic or diagnostic variable supplied by COSMO-CLM. A total of 158 historical winter storms between 1972 and 2008 are simulated to have a sufficient large database to validate the model performance. The simulations of the winter storms are evaluated by comparing the resulting track and pressure progressions with corresponding ERA-Interim reanalysis data. Additionally, the wind gust estimation approach is extended by a probabilistic approach that permits the estimation of uncertainties of expected wind gusts. Wind and gust observations of 37 weather stations are taken into account for validation of the new TKE-method.

An important result is the assertion that the COSMO-CLM is able to provide realistic and applicable simulations of severe winter storm events affecting Europe. For the ten strongest cyclones in terms of potential damage over Germany, the absolute minimum of core pressure values and the corresponding location are in good agreement, except for winter Storm Daria (January 1990). Further comparisons of simulated and observed 10m wind speed and maximum wind gusts are in good agreement. Obviously, the proper simulation of 10 m wind speed is of importance. If 10 m wind speed is not predicted correctly, the wind gust estimation methods depending on 10 m wind speed fail as well. The results of the TKE-method are comparable with the wind gust estimation method by Schulz and Heise (2003), which is the standard version for the estimation of wind gusts in COSMO-CLM. Outcomes of the TKE-method are additionally compared to the method after Brasseur (2001). The maximum wind gust as simulated by the Brasseur-method is overestimated in most cases (except for observations at mountain stations). Also, the method after Brasseur hardly shows any reduction of gust speed over land compared to marine areas. As a result, the TKE-method is superior concerning the method after Brasseur. Another crucial point is the precise spatial and temporal representation of wind (gust) patterns by COSMO-CLM, for example during the passage of a cold front. Small temporal discrepancies between simulations and observations

can lead to large differences when comparing time series of wind gusts. Therefore, the considering of footprints that represent the maximum wind gust at each grid point during the storm period is suggested to eliminate temporal dependencies. The introduction of the probabilistic approach, which is currently limited to the 37 observational sites, reveals some promising results. The determination of quantiles permits the estimation of uncertainties by indicating ranges in which the gusts are expected to occur. The estimation of uncertainties may be of added value when issuing appropriate weather warnings or for applications for wind gust related damage estimation.

### **6.2 Paper II**

Paper II presents the results of the case study about winter storm Kyrill (January 2007). The storm swept about large parts of Western, Central and Eastern Europe and caused widespread havoc, high economic losses and loss of life. Kyrill was embedded in a strong zonal background pressure gradient related to strong positive values of the NAO index. It was the strongest storm during a storm series in January 2007. The storm emerged in a strong baroclinic environment and underwent explosive cyclogenesis as it crossed the upper-level jet stream from south to north over the central North Atlantic Ocean and reached its maximum intensity west of the Irish coast. Usually, the development of such systems slowed down after crossing the jet stream. In the case of Kyrill, a secondary cyclone developed and, in combination with favourable upper-level conditions like a split jet structure with associated strong divergence, moves with maintained deep pressure further towards Europe. Most severe damage was reported when the associated convectively interspersed cold front crossed Germany and neighbouring countries. ERA-Interim driven, horizontal highly resolved, ( $0.22^\circ$  to  $0.025^\circ$ ) COSMO-CLM simulations were performed to clarify the dynamical aspects that led to the formation of the secondary cyclone and are accountable for the strong wind gust along the cold front.

The results of the simulations indicate that the formation of the secondary cyclone occurs along the occluded front. This kind of secondary cyclogenesis is not mentioned in current review articles that cover the topic so far and thus can be considered as a rare event. Negative stretching deformation along the occluded front and diabatic processes in the mid and lower troposphere is found to be among the mechanisms that account for the secondary development. Furthermore, the split jet structure and associated upper level divergence, which is asserted to be responsible for the maintenance of the deep core pressure is well reproduced

by the COSMO-CLM when compared to reanalysis data. Analyses of the severe wind gusts associated with the strong cold front show a clear relation between high momentum in the lower troposphere (wind speed exceeding  $45 \text{ m s}^{-1}$  at 850 hPa) together with conditional instability and a turbulent flow (assessed by low gradient Richardson number) in the boundary layer. These conditions could explain the high wind gusts generated by downward mixing of high momentum to the surface. According to the realistic physical interpretation of the nature of wind gusts by COSMO-CLM, an area-wide assertion of surface wind gusts is permitted. Consequently, the results of two different wind gust estimation methods implemented in the COSMO-CLM indicate the occurrence of widespread severe wind gusts during the cold front passage.

### **6.3 Paper III**

Paper III presents the results of the case study about winter storm Xynthia (February 2010). This extraordinary winter storm was characterised by a far southern origin close to the subtropics ( $30^\circ\text{N}$ ) over the central North Atlantic. During its life cycle, the storm first affected the Portuguese coast, re-intensifies as it crossed the Bay of Biscay and makes landfall at the French Atlantic coast. Afterwards, Xynthia steadily weakened and continued to move in northeastern direction until it dissipated over the Baltic Sea. Xynthia occurred during a record breaking negative NAO phase and was associated with an upper level PV-streamer and a southern displaced jet stream that exhibits a split structure aloft the surface cyclone. ERA-Interim reanalysis data is utilised to capture the large-scale environment in which the storm was embedded. Additionally, ERA-Interim driven COSMO-CLM simulations with horizontal grid spacing of  $0.22^\circ$  are realised and used to investigate the influence of diabatic processes on the development and strength of the storm.

The analysis of SSTs in the North Atlantic basin shows strong positive anomalies (up to  $3\text{K}$  close to the West African coast) compared to climatological mean SSTs in the southeastern parts of the North Atlantic. This is in line with the track of winter storm Xynthia, which moved along the anomalous warm ocean waters. Trajectory analyses reveal the incorporation of warm and moist air masses originating over the anomalously warm Ocean surface into the cyclone. To emphasize the role of the enhanced SSTs on the cyclone development, COSMO-CLM sensitivity studies with lowered initial SSTs and reduced surface latent heat fluxes are conducted, respectively. The results clearly indicate a strong link between the SST / surface fluxes and the maximum intensity of the storm. By lowering the

SST in the southeastern Atlantic by 3K, an increase of minimum core pressure of more than 10 hPa is observed, which implies a less intense cyclone development. Additionally, the development of Xynthia is slightly retarded in case of lower SST / surface fluxes. Finally, the vertical structure of Xynthia is also modified under the influence of altered surface conditions. The vertical extended PV-tower that is a result of strong diabatic heating in the lower and mid troposphere, is considerably weakened within the sensitivity studies. The reduced diabatic heating in the sensitivity studies is attributed to less warm and humid air masses over the ocean that is involved in the cyclogenesis process.

### **6.4 Discussion and outlook**

The comprehensive analysis of recent winter storms over the North Atlantic - European sector with high-resolution COSMO-CLM simulations extends the current knowledge and provides a substantial basis for further research activities on that topic. Therefore, the essential requirement of realistic simulations of individual winter storm events by the COSMO-CLM is ascertained. In this subsequent section, the main outcomes of this thesis are discussed and further research possibilities are suggested.

The realistic simulation of 158 winter storm events by COSMO-CLM allows the introduction and evaluation of the TKE-method. Since the comparison of the presented probabilistic wind gust estimation approach to measurements is limited to 37 observational sites in Germany, the spatial extension of the approach would be a challenging issue. Therefore, the obtained statistical characteristics of observed gustiness at stations have to be spatially interpolated to the corresponding grid of simulated quantities. As discussed in Paper I, a simple multi linear regression approach using fixed topographic characters as predictors is not satisfying. The consideration of further dynamical parameters like prevailing wind direction and TKE itself seem to be important factors that have to be taken into account when generating gridded statistical characteristics of gustiness based on observations. A successful interpolation of the observed gustiness characteristics and further application of the probabilistic approach would offer a powerful tool for the estimation of uncertainties (by indicating a possible range of maximum wind gusts) of the occurrence of wind gust on area-wide basis that could be of relevance for both society and applications in the insurance industry as well. An alternative way to apply the probabilistic approach on a wider base could be achieved by deriving synthetic wind gusts from wind observations at synoptic station sites when wind gusts measurements are missing or not reported. Seregina *et al.* (2014) recently

developed a wind gust model whereby the observational basis could be extended by wind gust data for 123 weather stations across Germany. Finally, the consideration of gusts as a result of mean wind speed and a turbulent part (TKE) provides a physically consistent approach to obtain wind gusts by the COSMO-CLM. It is suggested that such physical methods (likewise the method after Brasseur) should be preferred for realistic wind gust estimation in comparison to purely statistical relationships of mean wind speed and wind gusts. Nevertheless, the possibility of further fine-tuning of the proposed wind gust estimation approach should not be excluded. Additionally, the results of the 158 simulated winter storm events, as used for model evaluation in this thesis, have been embedded in a study by the GDV (Gesamtverband der Deutschen Versicherer, German Insurance Association) to estimate the costs of climate change for the insurance industry in Germany (Held *et al.*, 2013). The application of the dynamical downscaling of winter storm events is also used in a combined statistical and dynamical approach to obtain high-resolution footprints of winter storm events from large-scale datasets (Haas and Pinto, 2012).

The analysis of winter storm Kyrill in January 2007 (Paper II) reveals new insights on the dynamics that lead to the secondary cyclogenesis along the occluded front of the parent cyclone. Additionally the nature of the strong wind gusts along the cold front over Central Europe is considered. The detailed analysis of this particular kind of secondary cyclogenesis, which is even not considered in recent review literature on secondary cyclone development, may be applicable as a leading case study on this topic. Although dry baroclinic processes played the major role during the development of Kyrill (Fink *et al.*, 2012), diabatic processes seems to be an important factor during the formation of the secondary cyclone. Here, the incorporation of relatively warm and humid air masses in the warm sector of the storm may be connected with the diabatic processes. To support this statement, further investigations considering the sensitivity of diabatic processes (by means of additional modelling studies) on the intensity of the secondary cyclogenesis are possible research focuses in the future. This leads to the question of possible effects on the general characteristics of secondary frontal developments in the North Atlantic basin in the context of expected climate change. Since the preferred location of these secondary events is shifted downstream and south to the climatological storm track (Ayrault *et al.*, 1995), the potential of more intense storm events that are influenced by diabatic processes is given in case of generally expected warming of the atmosphere and adjacent ocean surface layers. As the availability of moisture will increase in a warmer atmosphere, this may imply an enhanced role diabatic processes due to stronger latent heat release in case those moist air masses are lifted when they are incorporated into the

cyclone. Also the analysis of the atmospheric conditions that are accountable for the widespread strong surface wind gusts in association with the severe cold front over Central Europe provides further research possibilities. Further, the application of the derecho definition to European winter storms, where Kyrill belongs to (Gatzen *et al.*, 2011), opens new perspectives on this topic of research.

In Paper III, the influence of warm and moist air masses on the development of winter storm Xynthia (2010) is analysed in more detail. Although the general correlation of enhanced SSTs and the intensity of extratropical cyclones have been described in earlier studies (e.g. Booth *et al.*, 2012; Giordani and Caniaux, 2001), a detailed study of winter storm Xynthia is considerable for various reasons. A variety of factors contribute to the uncommonly far southern origin and further development of Xynthia, each one noticeable and exceptional taken by itself. Among these factors are the record breaking negative NAO phase and associated warm SST anomalies over the southeastern North Atlantic, the existence of an upper level PV-streamer and a split jet structure with associated strong upper-level divergence. Especially the incorporation of warm and humid air masses that originate over the anomalously warm waters of the southeastern North Atlantic Ocean and associated diabatic processes appear to be of importance for the intensity of Xynthia. This case study confirms conclusions made by Fink *et al.* (2012), who stated that moist diabatic processes might have played a major role on the pressure drop of winter storm Xynthia. In a more recent study by Doyle *et al.* (2014), the sensitivity and predictability of winter storm Xynthia to perturbations of the moisture and temperature field is ascertained as well. Furthermore, results from a study by Liberato *et al.* (2013) confirm that the main supply of moisture is located over a region over the North Atlantic Ocean with anomalously high SSTs by identifying moisture sources, sinks and moisture transport with a lagrangian model. The variety of studies concerning winter storm Xynthia reveal the wide interest on this exceptionally storm. Additionally, all these studies point out the relevance of such kind of storms in the framework of climate change perspective. In the context of future warming (particularly of the ocean surface) due to increasing greenhouse gas forcing, the frequency, and thus associated hazards, of diabatically driven winter storms may increase in the future (Pinto *et al.*, 2009). The analysis of the sensitivity of winter storm Xynthia to increased available moisture contributes to the understanding of possible cyclone developments and expectable impacts of this kind of winter storms under future scenarios.

To conclude, the outcomes of this thesis extend the current knowledge and provide a substantial basis for the understanding of dynamical aspects and mesoscale mechanisms being

relevant during the genesis, development and the passage of individual winter storms like Kyrill (January 2007) and Xynthia (February 2010) over Europe. A comprehensive understanding of physical mechanisms and the effects of atmospheric conditions associated with individual winter storms are essential to improve the accuracy of the prediction of future storm events

### References\*

- ADAMSON, D. S., S. E. BELCHER, B. J. HOSKINS, AND R. S. PLANT, 2006: Boundary-layer friction in midlatitude cyclones. *Q. J. R. Meteorol. Soc.*, **132**, 101–124.
- AHMADI-GIVI, F., G. C. CRAIG, AND R. S. PLANT, 2003: The dynamics of a midlatitude cyclone with very strong latent heat release. *Q. J. R. Meteorol. Soc.*, **130**, 295–323.
- AYRAULT, F., F. LALAURETTE, A. JOLY, AND C. LOO, 1995: North Atlantic ultra high frequency variability. *Tellus A*, **47**, 671–696.
- BAEHR C., B. POUPONNEAU, F. AYRAULT, AND A. JOLY, 1999: Dynamical characterization of the FASTEX cyclogenesis cases. *Q. J. R. Meteorol. Soc.*, **125**, 3469–3494.
- BAKER, L. 2009: Sting jets in severe northern European wind storms. *Weather*, **64**, 143–148.
- BJERKNES, J., AND H. SOLBERG, 1922: Life cycles of cyclones and the polar front theory of atmospheric circulation. *Geophys. Publ.*, **3**, 1–18.
- BJERKNES, J. AND J. HOLMBOE, 1944: On the theory of cyclones. *J. Meteor.*, **1**, 1–22.
- BOOTH J. F., L. THOMPSON, J. PATOUX, AND K.A. KELLY, 2012: Sensitivity of midlatitude storm intensification to perturbations in the sea surface temperature near the Gulf stream. *Mon. Wea. Rev.*, **140**, 1241–1256.
- BRASSEUR, O., 2001: Development and Application of a Physical Approach to Estimating Wind Gusts. *Mon. Wea. Rev.*, **129**, 5–25.
- BROWNING, K. A., AND C. W. PARDOE, 1973: Structure of low-level jet streams ahead of mid-latitude cold fronts. *Q. J. R. Meteorol. Soc.*, **99**, 619–638.
- BROWNING, K.A., 1986: Conceptual models of precipitation systems. *Wea. Forecasting*, **1**, 23– 41.
- BROWNING, K. A. 1994: Life cycle of a frontal cyclone. *Met. Apps*, **1**, 233–235.
- BROWNING, K. A., AND R. REYNOLDS, 1994: Diagnostic study of a narrow cold-frontal rainband and severe winds associated with a stratospheric intrusion. *Q. J. R. Meteorol. Soc.*, **120**, 235–257.
- BROWNING, K. A., 1997: The dry intrusion perspective of extra-tropical cyclone development. *Met. Apps.*, **4**, 317–324
- BROWNING, K. A., 2004: The sting at the end of the tail: Damaging winds associated with extratropical cyclones. *Q. J. R. Meteorol. Soc.*, **130**, 375–399.
- CAMPA, J, AND H. WERNLI, 2012: A PV perspective on the vertical structure of mature midlatitude cyclones in the northern hemisphere. *J. Atmos. Sci.*, **69**, 725–740.

---

\* for chapters 1,2, and 6

## References

---

- CARLSON, T. N., 1980: Airflow through midlatitude cyclones and the comma cloud pattern. *Mon. Wea. Rev.*, **108**, 1498–1509.
- CARLSON T. N., 1991: *Mid-latitude Weather Systems*. Harper Collins: London. pp. 507.
- CHARNEY, J. G., 1947: The dynamics of long waves in a baroclinic westerly current. *J. Meteor.*, **4**, 135-162.
- CLARK P. A., K. A. BROWNING, AND C. WANG, 2005: The sting at the end of the tail: Model diagnostics of fine-scale three-dimensional structure of the cloud head. *Q. J. R. Meteorol. Soc.*, **131**, 2263–2292.
- DANARD M. B., 1964: On the influence of released latent heat on cyclone development. *J. Appl. Meteorol.*, **3**, 27–37.
- DACRE H. F., AND S. L. GRAY, 2006: Life-cycle simulations of low-level frontal waves and the impact of deformation strain, *Q. J. R. Meteorol. Soc.*, **132**, 2171-2190.
- DE ROOY, W. C., AND K. KOK, 2004: A combined physical statistical approach for the downscaling of model wind speed. *Wea. Forec.* **19**, 485–495.
- DELLA-MARTA, P. M., M. A. LINIGER, C. APPENZELLER, D. N. BRESCH, P. KÖLLNER-HECK, AND V. MUCCIONE, 2010: Improved estimates of the European winter wind storm climate and the risk of reinsurance loss using climate model data. *J. Appl. Meteor. Clim.* **49**, 2092–2120.
- DOYLE, J. D., C. AMERAULT, C. A. REYNOLDS, AND P. A. REINECKE, 2014: Initial condition sensitivity and predictability of a severe extratropical cyclone using a moist adjoint. *Mon. Wea. Rev.*, **142**, 320–342.
- DURST, C. D., 1960. Wind speeds over short periods of time. *Meteorol. Mag.*, **89**, 181–186.
- EADY, E.T., 1949: Long waves and cyclone waves. *Tellus*, **1**, 33–52.
- ERTEL, H., 1942: Ein neuer hydrodynamischer wirbelsatz. *Meteor. Z.*, **59**, 277–281.
- ETIENNE, C., S. GOYETTE, AND C.-A. KUSZLI, 2013: Numerical investigations of extreme winds over Switzerland during 1990-2010 winter storms with the Canadian Regional Climate Model. *Theor. Appl. Climatol.*, **113**, 529-547.
- FINK A. H., T. BRÜCHER, V. ERMERT, A. KRÜGER, AND J. G. PINTO, 2009: The European storm Kyrill in January 2007: Synoptic evolution and considerations with respect to climate change. *Nat. Hazards Earth Syst. Sci.*, **9**, 405-423.
- FINK A. H., S. POHLE, J. G. PINTO, AND P. KNIPPERTZ, 2012: Diagnosing the influence of diabatic processes on the explosive deepening of extratropical cyclones. *Geophys. Res. Lett.*, **39**, L07803
- GATZEN, C., T. PÚČIK, AND D. RYVA, 2011: Two cold-season derechoes in Europe. *Atmos. Res.*, **100**, 740-748.
- GIORDANI H., AND G. CANIAUX, 2001: Sensitivity of cyclogenesis to sea surface temperature in the northwestern Atlantic. *Mon. Wea. Rev.*, **129**, 1273–1295.

## References

---

- GRAMS, C. M., H. WERNLI, M. BÖTTCHER, J. CAMPA, U. CORSMEIER, S. C. JONES, J. H. KELLER, C.-J. LENZ, AND L. WIEGAND, 2011: The key role of diabatic processes in modifying the upper-tropospheric wave guide: a North Atlantic case-study. *Q. J. R. Meteorol. Soc.*, **137**, 2174–2193.
- GRAMS, C. M., BINDER, H., PFAHL, S., PIAGET, N., AND H. WERNLI, 2014: Atmospheric processes triggering the Central European floods in June 2013, *Nat. Hazards Earth Syst. Sci. Discuss.*, **2**, 427–458, doi:10.5194/nhessd-2-427-2014
- GRAY, S. L. AND H. F. DACRE, 2006: Classifying dynamical forcing mechanisms using a climatology of extratropical cyclones. *Q. J. R. Meteorol. Soc.*, **132**, 1119–1137.
- GRØNÅS S., 1995: The seclusion intensification of the New Year's Day storm 1992. *Tellus A*, **47**, 733–746.
- HAAS R, AND J. G. PINTO, 2012: A combined statistical and dynamical approach for downscaling large-scale footprints of European windstorms. *Geophys. Res. Lett.*, **39**:L23804
- HARROLD, T. W., 1973: Mechanisms influencing the distribution of precipitation within baroclinic disturbances. *Q. J. R. Meteorol. Soc.*, **99**, 232–251.
- HELD H., F. W. GERSTENGARBE, T. PARDOWITZ, J. G. PINTO, U. ULBRICH, U. BÖHM, K. BORN, M. BÜCHNER, M. G. DONAT, M. K. KARREMAN, G. C. LECKEBUSCH, P. LUDWIG, K. M. NISSEN, T. NOCKE, H. OSTERLE, B. F. PRAHL, P. C. WERNER, B. J. BEFORT, AND O. BURGHOFF, 2013: Projections of global warming-induced impacts on winter storm losses in the German private household sector. *Clim Change*, **121**, 195–207.
- HOSKINS B. J., M. E. MCINTYRE, AND A. W. ROBERTSON, 1985: On the use and significance of isentropic potential vorticity maps. *Q. J. R. Meteorol. Soc.*, **111**, 877–946.
- HOSKINS, B. J. AND P. BERRISFORD, 1988: A potential vorticity perspective of the storm of 15–16 October 1987. *Weather*, **43**, 122–129.
- HOSKINS, B. J., 1990: Theory of extratropical cyclones. In *Extratropical Cyclones—The Erik Palmén memorial volume*, Newton C., Holopainen E. O. (eds.), Amer. Meteorol. Soc: Boston, 63–80.
- HOSKINS, B. J., AND P. J. VALDES, 1990: On the Existence of Storm-Tracks. *J. Atmos. Sci.*, **47**, 1854–1864.
- HOSKINS, B., 1997: A potential vorticity view of synoptic development. *Met. Apps.*, **4**, 325–334
- HOSKINS B. J., AND K. I. HODGES, 2002: New perspectives on the Northern Hemisphere winter storm tracks. *J. Atmos. Sci.*, **59**, 1041–1061.
- HOUBE, R. A. JR., AND P. V. HOBBS, 1982: Organization and structure of precipitating cloud systems. *Adv. Geophys.*, **24**, 225–31.
- HURRELL J. W., AND C. DESER, 2009: North Atlantic climate variability: the role of the North Atlantic Oscillation. *J. Mar. Syst.*, **78**, 28–41.
- HURRELL, J., 1995: Decadal trends in the North Atlantic Oscillation: Regional temperatures and precipitation. *Science*, **269**, 676–679.
- JOLY, A., AND A. J. THORPE, 1991: The stability of time-dependent flows: An application to fronts in developing baroclinic waves. *J. Atmos. Sci.*, **48**, 163–182.

## References

---

- KALNAY E., M. KANAMITSU, R. KISTLER, W. COLLINS, D. DEAVEN, L. GANDIN, M. IREDELL, S. SAHA, G. WHITE, J. WOOLLEN, Y. ZHU, A. LEETMAA, B. REYNOLDS, M. CHELLIAH, W. EBISUZAKI, W. HIGGINS, J. JANOWIAK, K. C. MO, C. ROPELEWSKI, J. WANG, R. JENNE, AND D. JOSEPH, 1996: The NCEP-NCAR 40-year reanalysis project. *Bull. Am. Meteorol. Soc.*, **77**, 437–472.
- KLAWA, M., AND U. ULBRICH, 2003: A model for the estimation of storm losses and the identification of severe winter storms in Germany, *Nat. Hazards Earth Syst. Sci.*, **3**, 725–732.
- KNOX, J. A., J. D. FRYE, J. D. DURKEE, AND C. M. FUHRMANN, 2011: Non-Convective high winds associated with extratropical cyclones. *Geography Compass*, **5**, 63–89.
- LIBERATO, M. R. L., J. G. PINTO, I. F. TRIGO, AND R. M. TRIGO, 2011: Klaus - An exceptional winter storm over northern Iberia and southern France, *Weather*, **66**, 330–334.
- LIBERATO, M. L. R., J. G. PINTO, R. M. TRIGO, P. LUDWIG, P. ORDÓÑEZ, D. YUEN, AND I. F. TRIGO, 2013: Explosive development of winter storm Xynthia over the subtropical North Atlantic Ocean, *Nat. Hazards Earth Syst. Sci.*, **13**, 2239–2251.
- MAILIER, J. P., D. B. STEPHENSON, C. A. T. FERRO, AND K. I. HODGES, 2006: The serial clustering of extratropical cyclones. *Mon. Wea. Rev.*, **134**, 2224–2240.
- MASSACAND A. C., H. WERNLI, AND H. C. DAVIES, 2001. Influence of upstream diabatic heating upon an alpine event of heavy precipitation. *Mon. Wea. Rev.*, **129**, 2822–2828.
- PALMEN, E., 1948: On the distribution of temperature and wind in the upper westerlies. *J. Meteor.*, **5**, 20–27.
- PARKER, D. J., 1998: Secondary frontal waves in the North Atlantic region: A dynamical perspective of current ideas. *Q. J. R. Meteorol. Soc.*, **124**, 829–856.
- PARTON G. A., G. VAUGHAN, E. G. NORTON, K. A. BROWNING, AND P. A. CLARK, 2009: Wind profiler observations of a sting jet. *Q. J. R. Meteorol. Soc.*, **135**, 663–680.
- PIAGET, N., 2011: Genesis of winter storm “Xynthia”. Master thesis, IACETH, Zürich
- PINTO, J. G., S. ZACHARIAS, A. H. FINK, G. C. LECKEBUSCH, AND U. ULBRICH, 2009: Factors contributing to the development of extreme North Atlantic cyclones and their relationship with the NAO. *Clim. Dyn.*, **32**, 711–737.
- PINTO, J. G., C. P. NEUHAUS, G. C. LECKEBUSCH, M. REYERS, AND M. KERSCHGENS, 2010: Estimation of wind storm impacts over West Germany under future climate conditions using a statistical-dynamical downscaling approach. *Tellus A*, **62**, 188–201.
- REED, R. J., 1990: Advances in knowledge and understanding of extratropical cyclones during the past quarter century: An overview. In *Extratropical Cyclones—The Erik Palmén memorial volume, Newton C., Holopainen E. O. (eds.)*. Amer. Meteorol. Soc: Boston, 27–47.
- REED, R. J., M. T. STOELINGA, AND Y.-H. KUO, 1992: A model-aided study of the origin and evolution of the anomalously high potential vorticity in the inner region of a rapidly deepening marine cyclone. *Mon. Wea. Rev.*, **120**, 893–913.

## References

---

- RENFREW, I. A., A. J. THORPE, AND C. H. BISHOP, 1997: The role of the environmental flow in the development of secondary frontal cyclones. *Q. J. R. Meteorol. Soc.*, **123**, 1653–1675.
- ROCKEL, B., A. WILL, AND A. HENSE, (EDS.), 2008: Special issue: regional climate modelling with COSMO-CLM (CCLM). *Meteor. Z.*, **17**, 347–348.
- ROSSA, A. M., H. WERNLI, AND H. C. DAVIES, 2000: Growth and decay of an extra-tropical cyclone's PV-tower. *Meteor. Atmos. Phys.*, **73**, 139–156.
- ROSSBY, C.G. AND COLLABORATORS, 1939: Relation between variations in the intensity of the zonal circulation of the atmosphere and the displacements of the semi-permanent centers of action. *J. Marine. Res.*, **2**, 38–55.
- ROSSBY, C. G., 1940: Planetary flow patterns in the atmosphere. *Q. J. R. Meteorol. Soc.*, **66**, 68–87.
- SANDERS, F., AND J. R. GYAKUM, 1980: Synoptic-Dynamic Climatology of the “Bomb”. *Mon. Wea. Rev.*, **108**, 1589–1606.
- SCHULTZ D. M., AND C. F. MASS, 1993: The occlusion process in a midlatitude cyclone over land. *Mon. Wea. Rev.*, **121**, 918–940.
- SCHULTZ D. M., AND P. N. SCHUMACHER, 1999: The use and misuse of conditional symmetric instability. *Mon. Weather Rev.*, **127**, 2709–2732.
- SCHULTZ D. M., AND G. VAUGHAN, 2011: Occluded fronts and the occlusion process: A fresh look at conventional wisdom. *Bull. Amer. Meteor. Soc.*, **92**, 443–466.
- SCHULZ, J.-P., AND E. HEISE, 2003: A new scheme for diagnosing near-surface convective gusts. *COSMO Newsl.*, **3**, 221–225. Online at: [www.cosmo-model.org](http://www.cosmo-model.org)
- SCHWIERZ, C., P. KÖLLNER-HECK, E. ZENKLUSEN MUTTER, D. N. BRESCH, P.-L. VIDALE, M. WILD, AND C. SCHÄR, 2010: Modelling European winter wind storm losses in current and future climate. *Clim. Change*, **101**, 485–514.
- SEMPLE, A. T., 2003: A review and unification of conceptual models of cyclogenesis. *Met. Apps.*, **10**, 39–59.
- SEREGINA L. S., R. HAAS, K. BORN, AND J. G. PINTO, 2014: Development of a wind gust model to estimate gust speeds and their return periods. *Tellus A* (accepted)
- SHAPIRO, M. A., AND D. KEYSER, 1990: Fronts, jet streams and the tropopause. *In Extratropical Cyclones—The Erik Palmén memorial volume, Newton C, Holopainen E. O. (eds.)* Amer. Meteorol. Soc: Boston, 167–191.
- TRACTON M. S., 1973. The role of cumulus convection in the development of extratropical cyclones. *Mon. Wea. Rev.* **101**, 573–593.
- OORT, A. H., 1971: The observed annual cycle in the meridional transport of atmospheric energy. *J. Atmos. Sci.*, **28**, 325–339.
- UCCELLINI L. W., AND D. R. JOHNSON, 1979: The coupling of upper and lower tropospheric jet streaks and implications for the development of severe convective storms. *Mon. Wea. Rev.*, **107**, 682–703.

## References

---

- UCCELLINI L. W., 1990. Processes contributing to the rapid development of extratropical cyclones. *In Extratropical Cyclones—The Erik Palmén memorial volume*, Newton C., Holopainen E. O. (eds.) Amer. Meteorol. Soc: Boston, 81–105.
- ULBRICH, U., A. H. FINK, M. KLAWA, AND J. G. PINTO, 2001: Three extreme storms over Europe in December 1999. *Weather*, **56**, 70–80.
- ULBRICH U., T. BRÜCHER, A. H. FINK, A. KRÜGER, G. C. LECKEBUSCH, AND J. G. PINTO, 2003: The Central European Floods in August 2002: Part 2 - Synoptic causes and considerations with respect to climate change. *Weather*, **58**, 434–442.
- VERKAIK, J. W., 2000. Evaluation of two gustiness models for exposure correction values. *J. Appl. Meteor.*, **39**, 1613–1626.
- WANNER H., S. BRONNIMANN, C. CASTY, D. GYALISTRAS, J. LUTERBACHER, C. SCHMUTZ, D. B. STEPHENSON, AND E. XOPLAKI, 2001: North Atlantic oscillation. Concepts and studies. *Surv. Geophys.*, **22**, 321–382.
- WERNLI H., AND H. C. DAVIES, 1997: A Lagrangian-based analysis of extratropical cyclones. I: The method and some applications. *Q. J. R. Meteorol. Soc.*, **123**, 467–489.
- WERNLI, H., S. DIRREN, M. A. LINIGER, AND M. ZILLIG, 2002: Dynamical aspects of the life cycle of the winter storm ‘Lothar’ (24–26 December 1999). *Q. J. R. Meteorol. Soc.*, **128**, 405–429.
- WHITAKER, J. S., L. W. UCCELLINI, AND K. F. BRILL, 1988: A modelbased diagnostic study of the rapid development phase of the Presidents’ Day cyclone. *Mon. Wea. Rev.*, **116**, 2337–2365.
- WIERINGA, J., 1973. Gust factors over open water and built up country. *Bound. Layer Meteor.* **3**, 424–441.
- WOOLLINGS T., A. HANNACHI, B. J. HOSKINS, 2010. Variability of the North Atlantic eddy-driven jet stream. *Q. J. R. Meteorol. Soc.*, **136**, 856–868.

## Acknowledgements

I would like to thank the GDV (Gesamtverband der Deutschen Versicherer, contribution to project “Auswirkungen des Klimawandels auf die Schadensituation in der deutschen Versicherungswirtschaft”) and Aon-Benfield, Impact Forecasting (contribution to project “Development of a Pan-European Storm Risk Model“) for their financial support during the preparation of this thesis.

I thank Prof. Dr. Michael Kerschgens for mentoring me and giving me the opportunity to do my doctorate on this interesting topic.

I thank Prof. Dr. A. Fink for both being the second reviewer of my thesis and also for inspiring and fruitful discussions and Prof. Dr. Martin Melles for chairing the examining board.

I would particularly like to thank PD Dr. Joaquim Pinto for numberless and invaluable suggestions that contribute to the improvement of this thesis and also for co-authorship of the relevant publications for this study. I also sincerely thank Dr. Suzanne Gray for a lot of valuable advices and bringing forward new ideas that improves the publications in this thesis as well.

I thank my colleagues within the research group for the pleasant and inspiring working atmosphere within the different projects during the last couple of years: Dr. Mark Reyers, Rabea Haas, Melanie Karremann and Sven Ulbrich.

I am grateful to all colleagues at RTL for having a nice time working at the weather desk and giving me the opportunity to enhance my skills in weather forecasting if time permitted.

Furthermore I would like to thank my parents, Karin and Peter, for supporting me during the whole university studying and throughout my entire life.

Last but not least, my heartfelt thanks to my wife Sarah and my little boy Tom. No further explanation is necessary.

The COSMO-CLM simulations used in this study have been performed at the blizzard supercomputer at German Climate Computer Centre (DKRZ in Hamburg, Germany) within the context of DKRZ project ANDIVA (project ID 105).



## **Eigene Beteiligung an den Veröffentlichungen**

An der Entstehung der drei vorliegenden Artikel war ich maßgeblich beteiligt, was auch durch die Erstautorenschaft bei zwei der drei Artikel (Paper II und Paper III) belegt wird. Die grundlegende Implementierung der probabilistischen Methode zur Abschätzung von Böen in das COSMO-CLM durch Dr. K. Born begründet seine Erstautorenschaft bezüglich des dritten vorliegenden Artikels (Paper I). Meine Beteiligung an allen aufgeführten Publikationen umfasst deren Konzeption, die Durchführung der COSMO-CLM Simulationen der Winterstürme, das Aufbereiten der gemessenen Wind- und Böendaten, die Analyse und Auswertung der Modellergebnisse sowie die finale Ausarbeitung des jeweiligen Artikels in Zusammenarbeit mit den jeweiligen Co-Autoren.



## Erklärung

Ich versichere, dass ich die von mir vorgelegte Dissertation selbständig angefertigt, die benutzten Quellen und Hilfsmittel vollständig angegeben und die Stellen der Arbeit – einschließlich Tabellen, Karten und Abbildungen –, die anderen Werken im Wortlaut oder dem Sinn nach entnommen sind, in jedem Einzelfall als Entlehnung kenntlich gemacht habe; dass diese Dissertation noch keiner anderen Fakultät oder Universität zur Prüfung vorgelegen hat; dass sie – abgesehen von unten angegebenen Teilpublikationen – noch nicht veröffentlicht worden ist sowie, dass ich eine solche Veröffentlichung vor Abschluss des Promotionsverfahrens nicht vornehmen werde. Die Bestimmungen der Promotionsordnung sind mir bekannt. Die von mir vorgelegte Dissertation ist von Prof. Dr. Michael Kerschgens betreut worden.

Köln, im März 2014

(Patrick Ludwig)

Folgende Teilpublikationen liegen vor:

BORN, K., P. LUDWIG, AND J. G. PINTO, 2012: Wind Gust Estimation for Mid-European Winter Storms: Towards a Probabilistic View. *Tellus A* **64**:17471 doi: 10.3402/tellusa.v64i0.17471

LUDWIG, P., J. G. PINTO, S. A. HOEPP, A. H. FINK, AND S. L. GRAY, 2014; Secondary cyclogenesis along an occluded front leading to damaging wind gusts: windstorm Kyrill, January 2007. *Mon. Wea. Rev.* doi: <http://dx.doi.org/10.1175/MWR-D-14-00304.1>

LUDWIG, P., J. G. PINTO, M. REYERS, AND S. L. GRAY, 2014; The role of anomalous SST and surface fluxes over the southeastern North Atlantic in the explosive development of windstorm Xynthia. *Q. J. R. Meteorol. Soc.* **140**, 1729–1741. doi: 10.1002/qj.2253